

Ultrashort filaments of light in weakly-ionized, optically-transparent media

L. Bergé,* S. Skupin, and R. Nuter

Département de Physique Théorique et Appliquée, CEA-DAM/Île de France, B.P. 12, 91680 Bruyères-le-Châtel, France

J. Kasparian

Laboratoire de Spectroscopie Ionique et Moléculaire, Université Claude Bernard Lyon 1, 43 bd du 11 Novembre, 69622 Villeurbanne Cedex, France

J.-P. Wolf

GAP-Biophotonics, Université de Genève, 20 Rue de l'École de Médecine, 1211 Genève 4, Switzerland

(Dated: February 9, 2008)

Modern laser sources nowadays deliver ultrashort light pulses reaching few cycles in duration, high energies beyond the Joule level and peak powers exceeding several terawatt (TW). When such pulses propagate through optically-transparent media, they first self-focus in space and grow in intensity, until they generate a tenuous plasma by photo-ionization. For free electron densities and beam intensities below their breakdown limits, these pulses evolve as self-guided objects, resulting from successive equilibria between the Kerr focusing process, the chromatic dispersion of the medium, and the defocusing action of the electron plasma. Discovered one decade ago, this self-channeling mechanism reveals a new physics, widely extending the frontiers of nonlinear optics. Implications include long-distance propagation of TW beams in the atmosphere, supercontinuum emission, pulse shortening as well as high-order harmonic generation. This review presents the landmarks of the 10-odd-year progress in this field. Particular emphasis is laid to the theoretical modeling of the propagation equations, whose physical ingredients are discussed from numerical simulations. The dynamics of single filaments created over laboratory scales in various materials such as noble gases, liquids and dielectrics reveal new perspectives in pulse shortening techniques. Differences between femtosecond pulses propagating in gaseous or condensed materials are underlined. Attention is also paid to the multifilamentation instability of broad, powerful beams, breaking up the energy distribution into small-scale cells along the optical path. The robustness of the resulting filaments in adverse weathers, their large conical emission exploited for multipollutant remote sensing, nonlinear spectroscopy, and the possibility to guide electric discharges in air are finally addressed on the basis of experimental results.

PACS numbers: 42.65.Tg, 42.65.-k, 52.38.Hb, 42.68.Ay

Contents

I. Introduction	2	E. Self-phase modulation and supercontinuum generation	16
II. Propagation equations	3	F. Modulational instabilities: The route to multiple filamentation	17
A. Helmholtz equation	3	IV. Universal features of femtosecond filamentation	19
1. From vectorial to scalar description	4	A. Radial self-focusing and temporal splittings	19
2. Weak backscattering	4	B. Robustness and multifilamentation	21
3. Unidirectional pulse propagation	4	C. White light generation and Conical emission	23
4. Envelope description	5	D. Role of the laser wavelength	24
B. Nonlinear optical responses	6	V. Ultrashort filaments in gases	26
C. Plasma generation for singly-charged ionization	7	A. Novel perspectives for pulse shortening	26
III. Optical Ultrashort filaments: A few tools for their analytical description	10	B. High-order harmonic generation	28
A. Kerr focusing and wave collapse	10	VI. Ultrashort filaments in dense media	29
1. Principles of wave self-focusing	11	A. Pulse propagation in dielectrics and damages	29
2. Variational approaches	12	B. Pulse propagation in liquids and applications	30
B. Saturation by temporal dispersion	13	VII. Filaments in the atmosphere: Conveying intense structures over kilometers	32
C. Saturation by plasma defocusing	14	A. Long-distance propagation and white-light supercontinuum	32
D. Saturation by optical nonlinearities	15	1. Temporal chirping and spatial lensing	32
		2. Plasma and optical field measurements	33
		3. Multifilamentation	34
		4. White-light generation	36

*Electronic address: luc.berge@cea.fr

B. Remote sensing (LIDAR) applications	37
1. Principle of LIDAR: Towards "Femtolidars"	37
2. Remote filament-induced breakdown spectroscopy	38
C. Towards a laser lightning rod	39
VIII. Outlook	40
Acknowledgments	40
A. Ionization rates for atoms and molecules	41
1. Ionization in gases	41
a. The Keldysh theory	41
b. The PPT theory	42
c. The ADK molecular theory	42
2. Ionization in dense media	43
B. Atomic dipole for High-Harmonic Generation	43
C. The Teramobile laser	44
References	45

I. INTRODUCTION

Over the past two decades, ultrafast laser sources producing ultrashort pulses have come of age. Technological advances in this field have permitted the generation of light wave packets comprising only a few oscillation cycles of the electric field. In space, the extent of the pulses becomes focusable to a spot size comparable to the laser wavelength. In time, mode-locking and chirped-pulse amplification (CPA) technologies allow to access smaller and smaller durations and optical intensities locally exceeding hundreds of terawatt (TW) per cm^2 at moderate (sub-mJ) energies. Power levels nowadays approach the petawatt range with femtosecond pulse durations (1 fs = 10^{-15} sec.). Ultrashort light pulses enable researchers to probe ultrafast relaxation processes on never-before-accessed time scales and study light-matter interactions at unprecedented intensity levels. Due to extreme temporal and spatial confinements, the pulse strength exceeds that of the Coulomb field which binds electrons at their nucleus. It becomes strong enough to overcome the Coulomb barrier and triggers optical-field ionization. Pushed to ultrahigh intensities $> 10^{18}$ cm^2 , the availability of CPA lasers has extended the horizon of laser physics from atomic and optics studies to relativistic plasmas, nuclear and high-energy physics (Mourou *et al.*, 2006).

Before reaching such extreme intensities, progress in ultrashort laser systems has led to the ability to observe tunnel or multiphoton ionization in several spectral ranges, before the ionization process reaches saturation. In this regime, an intriguing phenomenon was discovered by Braun *et al.* (Braun *et al.*, 1995) in the middle of the nineties. By launching infrared pulses with femtosecond durations and gigawatt (GW) powers in the atmosphere, the beam became confined to a long-living, self-confined tube of light capable of covering several tens of meters, i.e., many linear diffraction lengths, along the propagation axis. The mechanism supporting this "light bullet"



FIG. 1 Principle of producing femtosecond filaments in air at the laser wavelength of 800 nm. Photograph at the right-hand side shows a transverse cut of the filament profile.

results from the balance between Kerr focusing, which increases the local optical index with the wave intensity, and self-induced ionization. When an ultrashort pulse self-focuses and couples with a self-induced plasma channel, its spatial profile exhibits a narrow extent along the optical path. Spectra broaden due to self-phase modulation (SPM), which is sustained by the mechanism of high-intensity clamping. This picture classically refers to what is commonly called a "femtosecond filament". In the diffraction plane, this filament is characterized by a white-light spot, surrounded by concentric "rainbows" with colors ranging from red to green. The high nonlinearities competing through the filamentation process produce an impressive supercontinuum leading to white-light emission. They also affect the beam divergence through an apparent conical emission, as illustrated in Fig. 1

Femtosecond filaments have, for the last decade, opened the route to a fascinating physics. Their highly nonlinear dynamics sparked broad interest, first because of the capability of femtosecond pulses to convey high intensities over spectacular distances, second because of the white light emitted by the filaments transforming infrared lasers into "white-light lasers" (Chin *et al.*, 1999b; Kasparian *et al.*, 2003). For appropriate beam configurations, long fs filaments can be created not only in the atmosphere, but also in noble gases, liquids and dielectric solids, as long as the pulse intensity does not reach the limit of optical breakdown, which implies the electron plasma density to remain at subdense levels. These optical structures are subject to strong modifications of their temporal profile, triggered by SPM together with the ionization front and the chromatic dispersion of the medium. The dynamical balance between nonlinear focusing and ionization can result in a drastic shortening of the pulse duration, down to the optical cycle limit. This property opens quite promising ways to generically deliver light with durations of a few fs only, which should further impact the fields of high-order harmonic generation and sub-fs pulse production. Besides, femtosecond pulses with broad spatial extents create several filaments, whose mutual interactions support the self-guiding of the beam envelope and can preserve a confined state upon several kilometers. This recently led to develop ultrashort Light Detection And Ranging (Lidar) facilities, that exploit the white light emitted by these filaments, in order to detect and identify several pollutants within a single laser shot.

Many applications have been inspired by this ultrafast "light bullet", which justifies the present review. Before commenting on these, an accurate understand-

ing of the filamentation phenomenon requires a rigorous derivation of the propagation equations together with basic tools for capturing the underlying physics. For this purpose, Section II addresses the model describing the long range propagation of ultrashort laser pulses in any optically-transparent medium. Section III reviews the basic phenomenon of wave self-focusing and its limitation by potential players such as plasma generation, chromatic dispersion and optical nonlinearities. Emphasis is given to semi-analytic (e.g., variational) methods providing qualitative information about these effects. Section IV lists the major phenomena driving femtosecond filaments, whatever the propagation medium may be. Section V is devoted to pulse shortening that can be achieved by letting femtosecond pulses ionize atom gases at appropriate pressures and to high-order harmonic generation. Section VI addresses different propagation regimes in condensed materials (water, silica glasses), from the laser-induced breakdown limit to X -shaped nonlinear waves self-guided with no plasma generation. Section VII concentrates on the atmospheric applications of the white-light supercontinuum emitted by ultrashort filaments. Current techniques for changing their onset distance and self-channeling length are discussed, together with the diagnostics used for plasma and optical-field measurements. Attention is paid to novel ultrashort LIDAR-based setups and their use in remotely analyzing aerosols, biological agents, dense targets through remote filament-induced breakdown spectroscopy. Their ability to trigger and guide electric discharges over several meters is also discussed. Section VIII finally summarizes the principal aspects of this review and presents future prospects.

II. PROPAGATION EQUATIONS

To start with, we derive the model describing the propagation of ultrashort optical pulses in transparent media. Using conventional description of nonlinear optics, straightforward combination of the Maxwell's equations yields (Agrawal, 2001; He and Liu, 1999; Shen, 1984)

$$\nabla^2 \vec{E} - \vec{\nabla}(\vec{\nabla} \cdot \vec{E}) - c^{-2} \partial_t^2 \vec{E} = \mu_0 (\partial_t^2 \vec{P} + \partial_t \vec{J}), \quad (1a)$$

$$\vec{\nabla} \cdot \vec{E} = (\rho - \vec{\nabla} \cdot \vec{P}) / \epsilon_0, \quad (1b)$$

where ϵ_0 , μ_0 and c denote the electric permittivity, magnetic permeability and the speed of light in vacuum, respectively. The optical electric field \vec{E} , the polarization vector \vec{P} , the carrier density ρ and the current density \vec{J} are real valued. For further convenience, we introduce standard Fourier transforms applied to the fields $(\vec{E}, \vec{P}, \vec{J})^\dagger$ as

$$(\widehat{\vec{E}}, \widehat{\vec{P}}, \widehat{\vec{J}})^\dagger(\vec{r}, \omega) \equiv \frac{1}{2\pi} \int (\vec{E}, \vec{P}, \vec{J})^\dagger(\vec{r}, t) e^{i\omega t} dt. \quad (2)$$

The current density \vec{J} describes the motions of the free electrons created by ionization of the ambient atoms,

for which ion dynamics is discarded. The polarization vector \vec{P} describes the bounded electron response driven by the laser radiation. It is usually decomposed into a linear part $\vec{P}_L \equiv \vec{P}^{(1)}$ related to the first-order susceptibility tensor $\overleftrightarrow{\chi}^{(1)}$ and a nonlinear one \vec{P}_{NL} satisfying $|\vec{P}^{(1)}| \gg |\vec{P}_{NL}|$. For isotropic, homogeneous, non magnetizable media and spectral ranges far from any material resonance, \vec{P} can be expressed as a power series in \vec{E} :

$$\widehat{\vec{P}} = \widehat{\vec{P}}^{(1)}(\vec{r}, \omega) + \widehat{\vec{P}}^{(3)}(\vec{r}, \omega) + \widehat{\vec{P}}^{(5)}(\vec{r}, \omega) + \dots \quad (3)$$

with scalar components

$$\begin{aligned} \widehat{P}_\mu^{(j)} = \epsilon_0 \sum_{\alpha_1 \dots \alpha_j} \int \dots \int \chi_{\mu\alpha_1 \dots \alpha_j}^{(j)}(-\omega_\sigma; \omega_1, \dots, \omega_j) \\ \times \widehat{E}_{\alpha_1}(\vec{r}, \omega_1) \dots \widehat{E}_{\alpha_j}(\vec{r}, \omega_j) \delta(\omega - \omega_\sigma) d\omega_1 \dots d\omega_j, \end{aligned} \quad (4)$$

where $\omega_\sigma = \omega_1 + \dots + \omega_j$. All susceptibility tensors $\overleftrightarrow{\chi}^{(j)}$ with even index j vanish due to inversion symmetry. The subscript μ indicates the field vector component in Cartesian coordinates and the indices α_j have to be summed up over x , y , and z . The tensor $\overleftrightarrow{\chi}^{(1)}$ is diagonal with $\chi_{\mu\alpha}^{(1)} = \chi^{(1)} \delta_{\mu\alpha}$, so that

$$\widehat{\vec{P}}^{(1)}(\vec{r}, \omega) = \epsilon_0 \chi^{(1)}(\omega) \widehat{\vec{E}}(\vec{r}, \omega), \quad (5)$$

and the scalar dielectric function, defined by

$$\epsilon(\omega) = 1 + \chi^{(1)}(\omega), \quad (6)$$

enters the wave number of the electromagnetic field $k(\omega) = \sqrt{\epsilon(\omega)}\omega/c$. Since $\chi^{(1)}$ is complex-valued, the dielectric function $\epsilon(\omega)$ contains every information not only about the material dispersion, but also about the linear losses given by the imaginary part of $\chi^{(1)}(\omega)$. When losses are negligible, $\epsilon(\omega)$ is real and reduces to $\epsilon(\omega) = n^2(\omega)$, where $n(\omega)$ here denotes the linear refractive index of the medium, which can be described in certain frequency ranges (far from resonances) by, e.g., a Sellmeier formula. By convention, $n_0 \equiv n(\omega_0)$ for the central frequency $\omega_0 = 2\pi c/\lambda_0$ of a laser operating at the wavelength λ_0 and $k_0 \equiv k(\omega_0)$. Without any specification, $\omega = 2\pi c/\lambda$, $w_\perp = 2\pi/k_\perp$ is the waist of the optical wave packet in the plane (x, y) and k_\perp is the corresponding extent in the transverse Fourier space.

A. Helmholtz equation

By taking its Fourier transform, Eqs. (1a) expresses as the Helmholtz equation

$$[\partial_z^2 + k^2(\omega) + \nabla_\perp^2] \widehat{\vec{E}} = -\mu_0 \omega^2 \widehat{\vec{F}}_{NL} + \vec{\nabla}(\vec{\nabla} \cdot \widehat{\vec{E}}), \quad (7a)$$

$$\vec{\nabla} \cdot \widehat{\vec{E}} = (\epsilon_0 \epsilon)^{-1} (\widehat{\rho} - \vec{\nabla} \cdot \widehat{\vec{P}}_{NL}), \quad (7b)$$

where $\nabla_{\perp}^2 \equiv \partial_x^2 + \partial_y^2$ stands for transverse diffraction and

$$\widehat{\mathcal{F}}_{\text{NL}} \equiv \widehat{P}_{\text{NL}} + i\widehat{J}/\omega \equiv \widehat{F} \otimes \widehat{E}, \quad (8)$$

gathers all nonlinear contributions through the function F that depends on \widehat{E} and can be viewed as the effective nonlinear refractive index change of the medium (\otimes is the convolution operator). Because Eqs. (7) are usually difficult to integrate in the full space-time domain, assumptions are requested to simplify them into more tractable form. The most fundamental of those consists in supposing that the wavefield keeps a transverse extension always fulfilling

$$k_{\perp}^2/k^2(\omega) \ll 1, \quad (9)$$

i.e., for $k(\omega)$ located around ω_0 , the transverse waist of the beam has dimensions larger than the central wavelength. The second one assumes small nonlinearities, i.e.,

$$\frac{\widehat{F}}{\epsilon_0\epsilon(\omega)} \ll 1. \quad (10)$$

1. From vectorial to scalar description

The previous conditions make vectorial effects negligible for, e.g, a transversally-polarized light field $E_{\perp} = (E_x, E_y)$. Indeed, Eqs. (7) can be combined, with the help of the continuity equation $\partial_t \rho + \vec{\nabla} \cdot \vec{J} = 0$ expressed in Fourier variable, into the form

$$[\partial_z^2 + k^2(\omega) + \nabla_{\perp}^2] \widehat{E} = -\mu_0\omega^2 \left[\widehat{\mathcal{F}}_{\text{NL}} + \frac{\vec{\nabla}(\vec{\nabla} \cdot \widehat{\mathcal{F}}_{\text{NL}})}{k^2(\omega)} \right], \quad (11)$$

whose last term scrambles nonlinear vectorial components. When we project the vectors $\widehat{E} = (\widehat{E}_{\perp}, E_z)^{\dagger}$, $\widehat{P}_{\text{NL}} = (\widehat{P}_{\text{NL}}^{\perp}, P_{\text{NL}}^z)^{\dagger}$, $\widehat{J} = (\widehat{J}_{\perp}, J_z)^{\dagger}$, $\vec{\nabla} = (\vec{\nabla}_{\perp}, \partial_z)^{\dagger}$ onto the transverse and longitudinal axis with unit vectors \vec{e}_{\perp} and \vec{e}_z , respectively, \widehat{E}_z is found to scale as $O(k_{\perp}/k)$. This follows from a direct Fourier transform of Eq. (7b) for weak nonlinearities [Eq. (10)]. Expressed in Fourier space, the nonlinear coupling of transverse/longitudinal components described by the scrambling term behave as $O(k_{\perp}^2/k^2)$ (Fibich and Ilan, 2001a,b; Milsted Jr. and Cantrell, 1996). So, these effects become important in the limit $k_{\perp} \rightarrow k(\omega)$ only. Reversely, if we postpone to further demonstrations that nonlinear compression processes are stopped *before* k_{\perp} becomes comparable with k (by, e.g., chromatic dispersion or plasma generation), the last term in the right-hand side (RHS) of (11) is close to zero, implying thereby $E_z \simeq 0$. The field remains transversally polarized along the propagation axis, making the influence of $\vec{\nabla}(\vec{\nabla} \cdot \widehat{\mathcal{F}}_{\text{NL}})/k^2$ negligible. Hence, as long as the nonlinear polarization and current density preserve the conditions (9) and (10), vectorial effects can be ignored for purely

optical or weakly-ionized materials as well. This property justifies the use of a scalar description for linearly-polarized beams having, e.g., $E_y = 0$.

2. Weak backscattering

The question of evaluating backscattering waves may be crucial in several areas, such as remote sensing experiments (Kasparian *et al.*, 2003; Yu *et al.*, 2001), which spectrally analyze the photons returning towards the laser source. The amount of backscattered photons, however, constitutes a weak percentage of those traveling in the forward direction through a transparent medium. The reason can be seen from the scalar version of Eq. (11) expressed as

$$D_+(\omega)D_-(\omega)\widehat{E} = -\nabla_{\perp}^2\widehat{E} - \mu_0\omega^2\widehat{F} \otimes \widehat{E}, \quad (12)$$

where $D_{\pm}(\omega) \equiv \partial_z \mp ik(\omega)$. By substituting the solution $\widehat{E} = \widehat{U}_+e^{ik(\omega)z} + \widehat{U}_-e^{-ik(\omega)z}$, Eq. (12) expands as

$$e^{2ik(\omega)z}[\partial_z^2 + 2ik(\omega)\partial_z + \nabla_{\perp}^2 + \mu_0\omega^2\widehat{F}]\widehat{U}_+ + [\partial_z^2 - 2ik(\omega)\partial_z + \nabla_{\perp}^2 + \mu_0\omega^2\widehat{F}]\widehat{U}_- = 0. \quad (13)$$

Here, \widehat{U}_+ and \widehat{U}_- represent the Fourier components of the forward and backward running fields, for which we a priori assume $|\partial_z U_{\pm}| \ll |k(\omega)U_{\pm}|$ and $U_+ \gg U_-$. For technical convenience, we assume $\widehat{F} = \tilde{F}\delta(\omega)$. Following Fibich *et al.* (Fibich *et al.*, 2002), we can integrate Eq. (13) over the interval $z - \pi/2k \leq z \leq z + \pi/2k$ (one fast oscillation) and Taylorize $\widehat{U}_{\pm}(z)$ to evaluate

$$2ik(\omega)\partial_z\widehat{U}_- \sim -\frac{e^{2ik(\omega)z}}{2ik(\omega)}\partial_z[\nabla_{\perp}^2 + \mu_0\omega^2\tilde{F}]\widehat{U}_+. \quad (14)$$

Since $\nabla_{\perp}^2 \sim -k_{\perp}^2$ in Fourier space, the backscattered component has a weak influence on the beam dynamics if $k_{\perp}^2 \ll k^2(\omega)$ and as long as the longitudinal variations of the nonlinearities remain small.

3. Unidirectional pulse propagation

The limit (9) moreover implies that the wave components forming the angle $\theta = \arcsin(k_{\perp}/k)$ between the transverse and longitudinal directions mostly propagate forwards since $\theta \ll \pi/2$ (Feit and Fleck, 1988). Because the propagation physics is mainly brought by the forward component, one has $\widehat{U}_- \rightarrow 0$ and $\widehat{E} \simeq \widehat{U}_+e^{ik(\omega)z}$. With the above approximations, the operator $D_-(\omega)$ for backscattering mainly applies to the most rapid variations of the field, expected to be driven by the complex exponential, i.e., $D_-(\omega)\widehat{E} \approx 2ik(\omega)\widehat{E}$. The so-called Unidirectional Pulse Propagation Equation (UPPE)

$$\partial_z\widehat{E} = \frac{i}{2k(\omega)}\nabla_{\perp}^2\widehat{E} + ik(\omega)\widehat{E} + \frac{i\mu_0\omega^2}{2k(\omega)}\widehat{\mathcal{F}}_{\text{NL}} \quad (15)$$

then naturally emerges from Eq. (12). Validity of this model explicitly requires that the second-order derivative in z of the envelope function \widehat{U}_+ must be small compared with $|k(\omega)\partial_z\widehat{U}_+|$, since $D_+(\omega)D_-(\omega)\widehat{\mathcal{E}} = e^{ik(\omega)z}[\partial_z^2 + 2ik(\omega)\partial_z]\widehat{U}_+$ (Geissler *et al.*, 1999; Husakou and Herrmann, 2001). This approximation, usually expressed as $|\partial_z\widehat{U}_+| \ll |k(\omega)\widehat{U}_+|$, refers to the "paraxiality" assumption. It holds if the field envelope U_+ does not significantly change over propagation distances of the order of λ , for all wavelengths under consideration. Paraxiality is again linked to the weakness of both the ratio k_\perp/k and the nonlinearities. Let us indeed assume the nonlinear function F clamped at a maximal constant level, F_{\max} . The forward component of Eq. (13) then goes like

$$\widehat{U}_+ \sim e^{ik(\omega)z} \sqrt{1 - \frac{k_\perp^2}{k^2(\omega)} + \frac{\mu_0\omega^2}{k^2(\omega)} F_{\max} - 1}. \quad (16)$$

It is seen right away that this solution fits that of the paraxial model discarding second derivatives in z , i.e., $\widehat{U}_+ \sim e^{-i(k_\perp^2 - \mu_0\omega^2 F_{\max})z/2k(\omega)}$, as long as the two constraints (9) and (10) apply.

Recently, Kolesik *et al.* (Kolesik and Moloney, 2004a; Kolesik *et al.*, 2002) proposed an UPPE model based on the exact linear modes of the Helmholtz equation. The key idea is to preserve the linear solutions, $\widehat{E}_{\text{lin}} = e^{\pm i\sqrt{k^2(\omega) + \nabla_\perp^2}z}$, as long as possible along the manipulation of Eq. (7a). Rewriting Eq. (12) as

$$D_+^\perp(\omega)D_-^\perp(\omega)\widehat{E} = -\mu_0\omega^2\widehat{\mathcal{F}}_{\text{NL}}, \quad (17)$$

with $D_\pm^\perp(\omega) \equiv (\partial_z \mp i\sqrt{k^2(\omega) + \nabla_\perp^2})$, we may retain the forward running component $\widehat{E} = \widehat{U}_+ e^{i\sqrt{k^2(\omega) + \nabla_\perp^2}z}$ constrained to the "paraxial" limit $D_-^\perp(\omega)\widehat{E} \approx 2i\sqrt{k^2(\omega) + \nabla_\perp^2}\widehat{E}$. Repeating the previous procedure immediately yields

$$\partial_z\widehat{E} = i\sqrt{k^2(\omega) + \nabla_\perp^2}\widehat{E} + \frac{i\mu_0\omega^2\widehat{\mathcal{F}}_{\text{NL}}}{2\sqrt{k^2(\omega) + \nabla_\perp^2}}. \quad (18)$$

Eq. (18) allows to formally describe DC-field components ($\omega = 0$), whereas Eq. (15) is limited to non-zero frequencies strictly. Despite these minor differences, UPPE models (15) and (18) become quite analogous when the condition $k_\perp^2/k^2 \ll 1$ applies. The major advantage of the UPPE models is to elude the formal use of a central optical frequency and correctly describe the complete spectrum of pulses in nonlinear regimes, even when they develop very large bandwidths.

For practical use, it is convenient to introduce the complex version of the electric field

$$E = \sqrt{c_1}(\mathcal{E} + \mathcal{E}^*), \quad \mathcal{E} = \frac{1}{\sqrt{c_1}} \int \Theta(\omega)\widehat{E}e^{-i\omega t}d\omega, \quad (19)$$

where $c_1 \equiv \omega_0\mu_0/2k_0$ and $\Theta(x)$ denotes the Heaviside function. Because \mathcal{E} satisfies $\widehat{\mathcal{E}}^*(\omega) = \widehat{\mathcal{E}}(-\omega)^*$ (* means

complex conjugate), it is then sufficient to treat the UPPE model (15) in the frequency domain $\omega > 0$ only. The field intensity can be defined by E^2 averaged over an optical period at least, for a given central frequency ω_0 . This quantity usually follows from the modulus of the time averaged Poynting vector. It is expressed in W/cm^2 and with the above normalization factor c_1 it is simply given by the classical relation $I = |\mathcal{E}|^2$.

4. Envelope description

When a central frequency ω_0 is imposed, Eq. (15) restitutes the Nonlinear Envelope Equation (NEE), earlier derived by Brabec and Krausz (Brabec and Krausz, 1997). We can make use of the Taylor expansion

$$k(\omega) = k_0 + k'\bar{\omega} + \widehat{\mathcal{D}}, \quad \widehat{\mathcal{D}} \equiv \sum_{n \geq 2}^{+\infty} \frac{k^{(n)}}{n!}\bar{\omega}^n, \quad (20)$$

where $\bar{\omega} = \omega - \omega_0$, $k' = \partial k/\partial\omega|_{\omega=\omega_0}$ and $k^{(n)} = \partial^n k/\partial\omega^n|_{\omega=\omega_0}$ and develop Eq. (15) as

$$\begin{aligned} \partial_z E = & \int \left[\frac{i\nabla_\perp^2}{2k(\omega)} + i(k_0 + k'\bar{\omega} + \widehat{\mathcal{D}}) \right] \\ & \times \widehat{E}(\omega)e^{-i\omega t}d\omega + i\frac{\mu_0}{2} \int \frac{\omega^2}{k(\omega)}\widehat{\mathcal{F}}_{\text{NL}}(\omega)e^{-i\omega t}d\omega. \end{aligned} \quad (21)$$

We apply the property following which $\widehat{E}(\omega)$ is the Fourier transform of $E(t)e^{i\omega_0 t}$ in $\bar{\omega}$, so that $\bar{\omega}$ corresponds to $i\partial_t$ by inverse Fourier transform. Terms with $k(\omega)$ in their denominator are expanded up to first order in $\bar{\omega}$ only. Furthermore, we introduce the complex-field representation

$$\mathcal{E} = Ue^{ik_0 z - i\omega_0 t}, \quad (22)$$

involving the novel envelope function U . Next, the new time variable $t \rightarrow t - z/v_g$ can be utilized to replace the pulse into the frame moving with the group velocity $v_g = k'^{-1}$. Eq. (21) then restores the NEE model

$$(i\partial_z + \mathcal{D})U \simeq -\frac{T^{-1}}{2k_0}(\nabla_\perp^2 U) - \frac{\mu_0\omega_0^2}{2k_0\sqrt{c_1}}T\mathcal{F}_{\text{NL}}^{\text{env}}(U), \quad (23)$$

where

$$\mathcal{D} \equiv \sum_{n \geq 2}^{+\infty} (k^{(n)}/n!)(i\partial_t)^n, \quad T = (1 + \frac{i}{\omega_0}\partial_t), \quad (24)$$

whenever $|k_0 - \omega_0 k'|/k_0 \ll 1$. This condition is met if the difference between group and phase velocity relative to the latter is small, which is fulfilled in a wide range of propagation phenomena. The operator T^{-1} introduces *space-time focusing* in front of the diffraction term $[T^{-1}(\nabla_\perp^2 U)]$. On the other hand, nonlinearities with the

envelope function $\mathcal{F}_{\text{NL}}^{\text{env}}(U)$ are also affected by the operator T , which refers to *self-steepening*. For dispersion relations truncated at some finite orders $n < +\infty$, the NEE model applies to optical fields with sufficiently narrow spectral bandwidths. With full chromatic dispersion, it holds for describing light pulses down to the single cycle.

B. Nonlinear optical responses

We henceforth assume a linearly polarized field (along, e.g., \vec{e}_x) and treat nonlinear effects within a scalar description. For centro-symmetric materials, only one relevant component of the tensor remains in the cubic contribution $P^{(3)}$, e.g., $\chi^{(3)} = \chi_{xxxx}^{(3)}$ (Agrawal, 2001). For simplicity, we may first consider $\chi^{(3)}$ as keeping a constant value for a spectral domain centered around ω_0 . Eq. (4) then simplifies with a single component, noted $\chi_{\omega_0}^{(3)}$, and in time domain one finds $P^{(3)}(\vec{r}, t) = \epsilon_0 \chi_{\omega_0}^{(3)} E^3$. This expression holds whenever we suppose an instantaneous response of the medium, which ignores the contribution of molecular vibrations and rotations to $\chi^{(3)}$. Strictly speaking, however, the phenomenon of Raman scattering comes into play when the laser field interacts with anisotropic molecules. This interaction can be schematized by a three-level system built from the rotational states of a molecule. The molecular scatterer has two rotational eigenstates, the ground state (level 1) with energy $\hbar\Omega_1$ and an excited one (level 2) with energy $\hbar\Omega_2$ where $\hbar = 1.06 \times 10^{-34}$ Js and Ω_m denotes the frequency of the state $m = 1, 2, 3$. Far above lies an electronic (or translational) state with energy $\hbar\Omega_3 \gg \hbar\Omega_2 - \hbar\Omega_1$. This molecule interacts with the laser field whose photon frequency ω_0 fulfills $\Omega_{13}, \Omega_{23} \gg \omega_0 \gg \Omega_{21}$, [$\Omega_{nm} \equiv \Omega_n - \Omega_m$], such that state $|3\rangle$ cannot be populated. Because of the definite parity of these molecular states, the dipole matrix element μ_{12} associated with the transition $|1\rangle \rightarrow |2\rangle$ via a single photon is null, so that the rotational state $|2\rangle$ can only be excited via transition through a virtual state $|3\rangle$ [$\mu_{13} \simeq \mu_{23} \equiv \mu \neq 0$]. Following this path, a Stokes photon with energy $\hbar\omega_s = \hbar\omega_0 - \hbar\Omega_{21}$ is emitted and the corresponding polarization vector involves the density matrix element associated with the states $|1\rangle$ and $|2\rangle$ as $P_{\text{Raman}} = \chi^{(1)}[\rho_{12}e^{i\omega_R t} + c.c.]E$. Here, $\omega_R = \Omega_{21}$ is the fundamental rotational frequency and ρ_{12} is found to satisfy (Peñano *et al.*, 2003)

$$\partial_t \rho_{12} \simeq -\frac{\rho_{12}}{\tau_2} - i\frac{\mu^2 E^2}{\hbar^2 \Omega_{31}} e^{-it/\tau_1}, \quad (25)$$

where $\tau_1 = 1/\omega_R$ and τ_2 is the dipole dephasing time. Eq. (25) provides the Raman response

$$P_{\text{Raman}} = \frac{2\chi^{(1)}\mu^2}{\Omega_{31}\hbar^2} E \int_{-\infty}^t e^{-\frac{t-t'}{\tau_2}} \sin\left(\frac{t-t'}{\tau_1}\right) E^2(t') dt', \quad (26)$$

which originates from nonresonant, nonlinear couplings.

Expressed in terms of the rescaled complex field \mathcal{E} [Eq. (19)] and with appropriate normalizations (Sprangle *et al.*, 2002), it completes the cubic polarization as

$$P^{(3)} = 2n_0 n_2 \epsilon_0 \sqrt{c_1} \int_{-\infty}^{+\infty} \bar{R}(t-t') |\mathcal{E}(t')|^2 dt' \mathcal{E} \quad (27a)$$

$$+ 2n_0 n_2 \epsilon_0 \sqrt{c_1} (1 - x_K) \mathcal{E}^3 / 3 + c.c.,$$

$$\bar{R}(t) = (1 - x_K) \delta(t) + x_K \Theta(t) h(t), \quad (27b)$$

$$h(t) = \frac{2}{3} \frac{\tau_1^2 + \tau_2^2}{\tau_1 \tau_2^2} e^{-t/\tau_2} \sin(t/\tau_1), \quad (27c)$$

with the definition of the nonlinear refractive index $n_2 = 3\chi_{\omega_0}^{(3)}/(4n_0^2 c \epsilon_0)$. Here, contributions in $O(\mathcal{E}^3)$ are retained to further describe third-harmonic generation. Expression (27a) possesses both retarded and instantaneous components in the ratio x_K . The instantaneous part $\sim \delta(t)$ describes the response from the bound electrons upon a few femtoseconds or less. The retarded part $\sim h(t)$ accounts for nuclear responses, namely, the Raman contribution, in which fast oscillations in E^2 give negligible contributions, as τ_1 and τ_2 currently far exceed the optical period $\sim \omega_0^{-1}$.

The fraction of delayed Kerr depends on the molecular species under consideration. For air at 800 nm, Sprangle (Sprangle *et al.*, 2002) suggests $\tau_1 \simeq 62$ fs, $\tau_2 \simeq 77$ fs and $x_K = 1/2$. This choice is consistent with that proposed in experimental papers (Nibbering *et al.*, 1997; Ripoche *et al.*, 1997). When $\tau_1 \sim \tau_2$, the function $h(t) \simeq (1/\tau_1)e^{-t/\tau_1}$ can also be used in the ratio $x_K = 1/2$ (Chiron *et al.*, 1999). For condensed materials, the parameter ranges $\tau_2/\tau_1 = 2 - 4$, $\tau_2 = 30 - 50$ fs with $x_K = 0.15 - 0.18$ have been suggested (Agrawal, 2001; Zozulya *et al.*, 1999). Values of the nonlinear Kerr index n_2 can be found in the literature (Gong *et al.*, 1998; Hellwarth *et al.*, 1990; Lehmeier *et al.*, 1985; Luo *et al.*, 1995; Nibbering *et al.*, 1997). Comprised between 10^{-19} cm²/W for gases and 10^{-16} cm²/W in dense media, they may, however, vary by a factor of the order of unity, depending on the procedure used for their evaluation (polarization spectroscopy, self- or cross-phase modulated spectra, time-resolved interferometry), together with the laser wavelength and pulse durations at which measurements are performed.

Besides, the susceptibility tensor has nonlinear components $\chi^{(j>3)}$ that satisfy the ordering (Boyd, 1992; Shen, 1984)

$$\frac{P^{(k+2)}}{P^{(k)}} = \frac{\chi^{(k+2)}}{\chi^{(k)}} \cdot \frac{E^{k+2}}{E^k} \approx \frac{|E|^2}{|E_{\text{at}}|^2}, \quad (28)$$

where $E_{\text{at}} \simeq 3 \times 10^{10}$ V/m is the characteristic atomic electric field strength with intensity $I_{\text{at}} > 10^{14}$ W/cm². Typically, the evaluation $\chi^{(5)}/\chi^{(3)} \sim 10^{-12}$ holds for nonresonant interactions in, e.g., gases. Despite the lack of knowledge on the sign of $\chi^{(5)}$ (Pan *et al.*, 1990), the quintic susceptibility is often expected to saturate Kerr focusing and has, therefore, a negative sign

(Nurhuda *et al.*, 2002b). Since the ordering (28) suggests that $\chi^{(j)}$ is rapidly decreasing with the order j , the Taylor series with respect to the electric field is truncated at the 5th order. Quintic polarization can be derived following the same procedure as above, with $\chi^{(5)}$ assumed constant in the frequency domain. By developing E^5 in terms of $(\mathcal{E}, \mathcal{E}^*)$ [Eq. (19)], the quintic contribution of the polarization vector then expands as

$$P^{(5)} = -2n_0n_4\epsilon_0\sqrt{c_1} \left(|\mathcal{E}|^4 + \frac{1}{2} |\mathcal{E}|^2 \mathcal{E}^2 + \frac{1}{10} \mathcal{E}^4 \right) \mathcal{E} + c.c. \quad (29)$$

where $n_4 = 5|\chi_{\omega_0}^{(5)}|/(4n_0^3c^2\epsilon_0^2)$. On the whole, the total nonlinear polarization vector reads as

$$P_{\text{NL}} = P^{(3)} + P^{(5)}. \quad (30)$$

C. Plasma generation for singly-charged ionization

When free electrons are created, they induce a current density $\vec{J} = q_e\rho\vec{v}_e$. This quantity depends on the electron charge $q_e = -1.6 \times 10^{-19}$ C, the electron density ρ and the electron velocity \vec{v}_e . \vec{J} is computed from the fluid equations (Esarey *et al.*, 1997; Sprangle *et al.*, 1996)

$$\partial_t\rho + \vec{\nabla} \cdot (\rho\vec{v}_e) = \mathcal{S}, \quad (31a)$$

$$\partial_t\vec{v}_e + (\vec{v}_e \cdot \vec{\nabla})\vec{v}_e = \frac{q_e}{m_e} \left(\vec{E} + \frac{\vec{v}_e \times \vec{B}}{c} \right) - \nu_e\vec{v}_e - \mathcal{S}\vec{v}_e/\rho. \quad (31b)$$

Here, \mathcal{S} represents external plasma sources and ν_e is the effective electron collision frequency. These equations can be combined to yield

$$\partial_t\vec{J} + \nu_e\vec{J} = \frac{q_e^2\rho}{m_e}\vec{E} + \vec{\Pi}, \quad (32)$$

where

$$\vec{\Pi} = \frac{q_e}{m_e c} \vec{J} \times \vec{B} - \frac{\vec{J}}{\rho q_e} (\vec{\nabla} \cdot \vec{J}) - (\vec{J} \cdot \vec{\nabla}) \vec{v}_e \quad (33)$$

represents ponderomotive forces acting on slowly-varying time scales. For linearly-polarized electromagnetic fields (\vec{E}, \vec{B}) oscillating at the high frequency ω_0 , the driving term $\vec{\Pi}$ admits envelope components containing gradients of the field intensity, radiation pressure due to electron collisions and changes in the electron density. Ponderomotive forces induce low plasma currents, which can in turn generate electromagnetic pulses (EMP) (Cheng *et al.*, 2001, 2002) and provide sources of coherent sub-THz radiation (Tzortzakis *et al.*, 2002). Numerical simulations (Peñano *et al.*, 2004; Sprangle *et al.*, 2004) have shown, however, that for 100-fs pulses reaching intensities of 10^{14} W/cm² and free electron densities $\rho \sim 10^{16}$ cm⁻³ in the atmosphere, the efficiency conversion to EMP is of the order of 10^{-9} with local intensities

attaining only 10 kW/cm². In dielectrics, the plasma generates EMP intensities remaining about \sim MW/cm² for peak laser intensities of $\sim 10^{13}$ W/cm². These ponderomotive terms can thus be ignored, as long as peak intensities are below 10^{15} W/cm². In this range, plasma density perturbations due to Langmuir wave oscillations and relativistic increase of the electron mass have also a negligible influence. Therefore, the equation for the current density reduces to Eq. (32) in which $\Pi = 0$. At the lowest order in v_e , the growth of the electron density is only governed by the source term \mathcal{S} , i.e.,

$$\partial_t\rho = \mathcal{S} = W(I)(\rho_{\text{nt}} - \rho) + \frac{\sigma}{U_i}\rho I - f(\rho), \quad (34)$$

that involves photo-ionization processes with rate $W(I)$, collisional ionization with cross-section σ , and a function describing electron recombination or attachment with neighboring ions denoted by $f(\rho)$. Here, ρ_{nt} and U_i are the density of neutral species and the ionization potential, respectively, while $\rho \ll \rho_{\text{nt}}$. Typically, the recombination function in gases has a quadratic dependency on ρ , so that $f(\rho) = \beta_{\text{recomb}}\rho^2$ with $\beta_{\text{recomb}}[\text{cm}^3/\text{s}] \sim 2 \times 10^{-8}$ at electron temperatures $T_e = 1$ eV (Mlejnek *et al.*, 1998a; Sprangle *et al.*, 2002; Tzortzakis *et al.*, 2000b). Recombination times belong to the nanosecond scale. In dielectrics, much shorter recombination times are involved ($\tau_{\text{recomb}} = 50 - 150$ fs) and the density linearly decreases like $f(\rho) = \rho/\tau_{\text{recomb}}$ (Audebert *et al.*, 1994; Peñano *et al.*, 2005; Tzortzakis *et al.*, 2001d).

Besides, the electron collisional rate depends on the electron energy distribution function and temperature versus the ionization potential U_i . Assuming a Maxwellian distribution function for the electron velocity, this rate linearly varies like $\sigma |\mathcal{E}|^2 / U_i$, as long as the electron thermal energy is small compared with U_i . Here, σ is the inverse bremsstrahlung cross-section (Lotz, 1967a,b). If we omit Ohmic heating, solving for the current density (32) leads by Fourier transformation to

$$\widehat{\vec{J}} = \frac{q_e^2}{m_e(\nu_e^2 + \omega^2)} (\nu_e + i\omega) \widehat{(\rho\vec{E})}. \quad (35)$$

The current density term in Eq. (1a) transforms as

$$\mu_0\partial_t\vec{J} \rightarrow \left[-i\frac{\omega n_0\sigma(\omega)}{c} + \frac{\omega_0^2}{c^2\rho_c(1 + \nu_e^2/\omega^2)} \right] \widehat{(\rho\vec{E})}, \quad (36)$$

after introducing the critical plasma density

$$\rho_c \equiv \frac{\omega_0^2 m_e \epsilon_0}{q_e^2} \simeq \frac{1.11 \times 10^{21}}{\lambda_0^2 [\mu\text{m}]} \text{cm}^{-3}, \quad (37)$$

at which the laser wave number vanishes. The cross-section

$$\sigma(\omega) = \frac{q_e^2}{m_e \epsilon_0 n_0 c \nu_e (1 + \omega^2/\nu_e^2)} \quad (38)$$

then provides the frequency-dependent collisional rate. This expression was earlier derived in the

limit of zero elastic collisions with ions by Kennedy (Kennedy, 1995), Yablonovitch and Bloembergen (Yablonovitch and Bloembergen, 1972) and by Feit and Fleck (Feit and Fleck, 1974). Often linked to what is called the "Drude" model, it determines energy losses through plasma (cascade) ionization.

In Eq. (34), $W(I)$ denotes the rate for photo-ionization. It is evaluated from perturbative theories valid as long as the electric field E is weaker than the atom field strength E_{at} . This rate has been re-derived in Appendix A, following Keldysh's and Perelomov, Popov and Terent'ev (PPT)'s theories applying to atoms or dielectrics (crystals) (Keldysh, 1965; Perelomov and Popov, 1967; Perelomov *et al.*, 1966, 1967). To describe the ionization of complex atoms, PPT formula usually includes the so-called ADK coefficients [for Ammosov, Delone and Krainov (Ammosov *et al.*, 1986)], originally established in the limit of high intensities. Optical field ionization theories stress two major limits bounded by the "adiabaticity" Keldysh parameter,

$$\gamma = \omega_0 \frac{\sqrt{2m_e U_i}}{|q_e| E_p}, \quad (39)$$

namely, the limit for multiphoton ionization (MPI, $\gamma \gg 1$) concerned with rather low intensities and the tunnel limit ($\gamma \ll 1$) concerned with high intensities, from which the Coulomb barrier becomes low enough to let the electron tunnel out. Here, E_p denotes the peak optical amplitude ($E_p = \sqrt{2c_1 I}$). For simplicity, we ignore the phenomenon of above-threshold ionization (Agostini *et al.*, 1979; Corkum *et al.*, 1989), through which the electron embarks more kinetic energy than $K\hbar\omega_0 - U_i$. For laser intensities $I = |\mathcal{E}|^2 < 10^{13}$ W/cm², MPI characterized by the limit

$$\gamma \gg 1 \implies W(I) \rightarrow W_{\text{MPI}} = \sigma_K I^K \quad (40)$$

dominates, where $K = \text{mod}(U_i/\hbar\omega_0) + 1$ is the number of photons necessary to liberate one electron. For higher intensities, tunnel ionization starts to contribute, i.e., electrons tunnel out within one optical cycle. Despite the complexity of ionization formulas, all of them exhibit common dependencies on the laser field strength (Perry *et al.*, 1988b; Reiss, 1980). By producing charged ions of noble gases as a function of the laser intensity, quantitative measurements confirmed the validity of Keldysh theory for singly-charged ions only (Perry *et al.*, 1988a). This theory basically applies to hydrogen atoms and discards the Coulomb field of the residual ion on the outgoing electron. The PPT/ADK or Krainov's models (Krainov, 1997), instead, better reproduce experimental ionization rates of atoms in, e.g., the tunnel regime and may even suit for higher-charged states (Augst *et al.*, 1991; Cornaggia and Hering, 2000). On this basis, ionization of diatomic molecules can be predicted through semi-empirical theories using the PPT rate in which the electron tunnels through a barrier with effective potential Z_{eff}/r . Here, Z_{eff} is determined by fitting the theo-

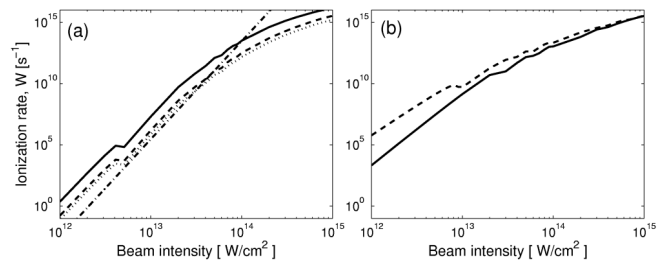


FIG. 2 (a) Ionization rate of O_2 molecules vs. laser intensity obtained from the PPT theory (solid curve), ADK molecular model (dashed curve), the fitting curve from PPT with $Z_{\text{eff}} = 0.53$ (dotted curve) (Talebpour *et al.*, 1999) and the MPI-like formulation (dash-dotted curve) used in (Couairon *et al.*, 2002) at 800 nm. (b) Keldysh ionization rates for crystals applied to fused silica (solid curve, $U_i = 7.8$ eV) and water (dashed curve, $U_i = 7$ eV) at the same laser wavelength.

retical slope of the PPT formula onto measured ion signals. For ion signals collected from the interaction of O_2 and N_2 molecules with a 800 nm laser pulse, Z_{eff} is inferred from PPT applied to a corresponding atom (Xe atom) with ionization potential close to that of dioxygen molecules ($U_i^{\text{O}_2} \simeq 12.1$ eV, $Z_{\text{eff}} = 0.53$) and to Ar atoms with U_i close to the energy gap of N_2 molecules ($U_i^{\text{N}_2} \simeq 15.6$ eV, $Z_{\text{eff}} = 0.9$) (Talebpour *et al.*, 1999). The PPT/ADK formula can alternatively be extended to O_2 molecules by selecting the molecular coefficients of Tong *et al.* (Tong *et al.*, 2002) within the so-called "ADK Molecular" ionization model (Nuter and Bergé, 2006).

Figure 2 illustrates ionization rates for some of the previous theories applied to O_2 molecules [Fig. 2(a)] or to fused silica [Fig. 2(b)]. PPT and ADK molecular ionization rates plotted in solid and dashed curves differ by only one decade. The dotted curve indicates the experimental fit from O_2^+ signals with the PPT rate using $Z_{\text{eff}} = 0.53$. A good agreement is achieved between this fit and the ADK molecular ionization curve. Note that as long as the beam saturates below 10^{13} W/cm², the MPI limit alone can be retained. Beyond this intensity, the photo-ionization rate departs from the law $\sigma_K I^K$ and must include tunnel contributions. To get qualitative behaviors only, the MPI rate may, however, be used at higher intensities, while keeping the interaction physics valid.

Because free carriers are first generated by photo-ionization, we must take the corresponding losses into account. Via energy conservation law, self-consistent expressions for these losses can be established. The temporal evolution of the energy density w is determined by a local version of the Poynting theorem, i.e.,

$$\frac{d}{dt}w(\vec{r}, t) = \vec{J}(\vec{r}, t) \cdot \vec{E}(\vec{r}, t), \quad (41)$$

from which we can compute the energy lost by the pulse when it extracts electrons through single ionization process (Kandidov *et al.*, 2003; Rae and Burnett, 1992). The amount of energy per time and volume units is then

given by $\vec{J} \cdot \vec{E} = U_i \partial_t \rho_{\text{PI}}$ where $\partial_t \rho_{\text{PI}} \equiv W(I)(\rho_{\text{nt}} - \rho)$. Using complex-valued fields, the current associated with photo-ionization losses is merely found to be

$$\vec{J}_{\text{loss}} = \sqrt{\frac{k_0}{2\omega_0\mu_0}} U_i \frac{W(I)}{I} (\rho_{\text{nt}} - \rho) (\vec{\mathcal{E}} + \vec{\mathcal{E}}^*), \quad (42)$$

where fast oscillations are canceled in the denominator. Geissler *et al.* (Geissler *et al.*, 1999) derived similar losses by introducing the overall polarization vector for free electrons $\vec{\mathcal{P}} = q_e \rho_{\text{PI}} \vec{x}$, so that $\partial_t \vec{\mathcal{P}} = q_e \dot{\rho}_{\text{PI}} \vec{x} + \vec{J}$. Free electrons arise with zero velocity at the position $\vec{x}(t) \simeq U_i \vec{E}/(2|q_e|I)$, yielding the same loss current.

As a final result, the propagation equation within the UPPE description (15) reads in Fourier space as

$$\frac{\partial}{\partial z} \hat{\mathcal{E}} = \left[\frac{i}{2k(\omega)} \nabla_{\perp}^2 + ik(\omega) \right] \hat{\mathcal{E}} + \frac{i\mu_0\omega^2}{2k(\omega)\sqrt{c_1}} \Theta(\omega) \hat{P}_{\text{NL}} - \frac{ik_0^2\Theta(\omega)}{2\epsilon(\omega_0)k(\omega)(1 + \frac{\nu_e^2}{\omega^2})} \left(\frac{\rho\hat{\mathcal{E}}}{\rho_c} \right) - \frac{\Theta(\omega)}{2} \sqrt{\frac{\epsilon(\omega_0)}{\epsilon(\omega)}} \mathcal{L}(\omega), \quad (43)$$

$$\frac{\partial}{\partial z} U = \frac{i}{2k_0} T^{-1} \nabla_{\perp}^2 U + i\mathcal{D}U + i\frac{\omega_0}{c} n_2 T \left[(1 - x_K) |U|^2 + x_K \int_{-\infty}^t h(t-t') |U(t')|^2 dt' \right] U - i\frac{\omega_0}{c} n_4 T |U|^4 U - i\frac{k_0}{2n_0^2\rho_c} T^{-1} \rho U - \frac{\sigma}{2} \rho U - \frac{\beta_{\text{MPA}}(|U|)}{2} U, \quad (45a)$$

$$\frac{\partial}{\partial t} \rho = W(I)(\rho_{\text{nt}} - \rho) + \frac{\sigma(\omega_0)}{U_i} \rho |U|^2 - f(\rho) \quad (45b)$$

where t stands for the retarded time variable $t - z/v_g$. The function $\beta_{\text{MPA}}(|U|) = (\rho_{\text{nt}} - \rho) U_i W(I) / |U|^2$ accounts for losses caused by photo-ionization. In the MPI limit (40), this dissipative function takes the form $\beta_{\text{MPA}}(|U|) \rightarrow \beta^{(K)} |U|^{2K-2}$ where $\beta^{(K)} \equiv K \hbar \omega_0 \sigma_K \rho_{\text{nt}}$ is the coefficient for multiphoton absorption (MPA). The first term of the operator \mathcal{D} corresponds to group-velocity dispersion (GVD) with coefficient $k'' = \partial^2 k / \partial \omega^2|_{\omega=\omega_0}$. Equations (45) describe wave diffraction, Kerr focusing response, plasma generation, chromatic dispersion with a self-consistent action of deviations from the classical slowly-varying envelope approximation through space-time focusing and self-steepening operators $[(T^{-1} \nabla_{\perp}^2 \mathcal{E})$ and $(T|\mathcal{E}|^2 \mathcal{E})$, respectively]. They are usually integrated numerically by using, e.g., initially singly-humped pulses taken with a super-Gaussian beam shape

$$U(x, y, z = 0, t) = U_0 e^{-\frac{r^{2N}}{w_0^{2N}} - ik_0 \frac{t^2}{2f} - \frac{t^2}{t_p^2} - iC \frac{t^2}{t_p^2}}, \quad (46)$$

which may be focused through a lens of focal length f and be temporally chirped if $C \neq 0$. Here, $r = \sqrt{x^2 + y^2}$. For Gaussian beams ($N = 1$), $U_0 = \sqrt{2P_{\text{in}}/\pi w_0^2}$ involves the input power P_{in} , w_0 is the beam waist and t_p the $1/e^2$ pulse half-width, such that its full-width-at-

where

$$\mathcal{L}(\omega) = \frac{U_i}{2\pi} \int \mathcal{E} \left[\frac{W(I)}{I} (\rho_{\text{nt}} - \rho) + \frac{\sigma(\omega)}{U_i} \rho \right] e^{i\omega t} dt. \quad (44)$$

$P_{\text{NL}}(\vec{r}, t)$ [Eq. (30)] and the expression containing the electron density $\rho(\vec{r}, t)$ [Eq. (34)] must be transformed to Fourier space. Treating the complex field \mathcal{E} only for positive frequencies is sufficient because of the symmetry $\widehat{\mathcal{E}}^*(\omega) = \widehat{\mathcal{E}}(-\omega)^*$, which imposes to select the parts of the nonlinear terms belonging to the frequency range $\omega > 0$.

For practical use, the collision cross-section σ is stated for a central frequency ω_0 . We furthermore assume $\nu_e^2/\omega_0^2 \ll 1$ and $\sqrt{\epsilon(\omega_0)}/\epsilon(\omega) \approx 1$. The link to the NEE model is then straightforward, whenever the dispersion relation supports a Taylor expansion around ω_0 . By retaining only waveforms beating at ω_0 , the nonlinear envelope equation for the forward component U is directly inferred from (23) as

half-maximum (FWHM) is $\Delta t = \sqrt{2 \ln 2} t_p$. The initial level ($t = -\infty$) of plasma density is zero. In linear propagation, such Gaussian pulses diffract over the distance

$$z_f = (f^2/z_0)/(1 + f^2/z_0^2), \quad (47)$$

where $z_0 = \pi n_0 w_0^2 / \lambda_0$ is the diffraction range of the collimated beam ($f = +\infty$). In nonlinear propagation, the interplay between all competitors in Eqs. (45) severely alters beam diffraction and can maintain the pulse in self-guided state over longer distances. As an example, Fig. 3 shows the dynamics of the maximum fluence ($\bar{F} = \int_{-\infty}^{+\infty} |\mathcal{E}|^2 dt$) for an unchirped, collimated Gaussian pulse with 0.9 and 0.45 μJ energies, input waist $w_0 = 71 \mu\text{m}$, half-width duration $t_p = 42.5$ fs propagating in a 3-cm long silica sample. This beam is numerically simulated from the UPPE model [Fig. 3(a)] and the NEE including higher-order dispersion up to $n = 5$ [Fig. 3(b)]. The ionization rate is delivered by the Keldysh's formula for crystals [Fig. 2(b)]. Silica promotes strong chromatic dispersion, which is approximated by the NEE model, but not by UPPE that describes the full linear dispersion relation. Despite this difference, we can observe that the beam fluence remains identical according to both descriptions (43) and (45). This property is true in several

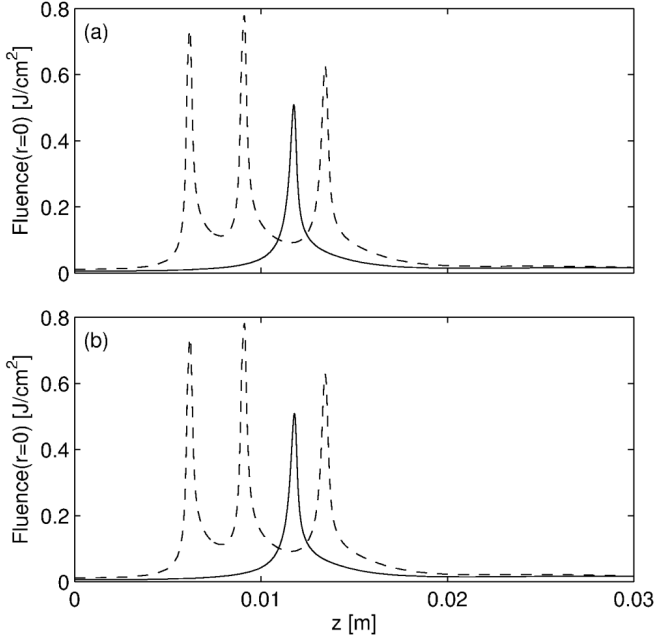


FIG. 3 Maximum fluence for pulses propagating in silica glass with $0.45 \mu\text{J}$ (solid curve) and $0.9 \mu\text{J}$ (dashed line) energies simulated from (a) the UPPE model, (b) the NEE model with dispersion limited to fifth order.

media (dielectrics, liquids and air as well), whenever Eq. (45a) includes dispersive contributions $k^{(n)}$ with $n > 3$ (Kolesik *et al.*, 2003b, 2002).

Earlier studies on femtosecond pulse propagation in the atmosphere started with simpler models than Eqs. (43) or (45) by, e.g., ignoring time dispersion (Kandidov *et al.*, 1994). Their derivation was improved later (Feng *et al.*, 1995; Mlejnek *et al.*, 1998a,b; Sprangle *et al.*, 1996), before being finalized into NEE and UPPE formulations.

III. OPTICAL ULTRASHORT FILAMENTS: A FEW TOOLS FOR THEIR ANALYTICAL DESCRIPTION

A. Kerr focusing and wave collapse

For beams with no temporal dispersion, Eq. (45a) with no other nonlinear response than the instantaneous cubic Kerr term ($x_K = 0$), i.e.,

$$\frac{\partial}{\partial z} U = \frac{i}{2k_0} \nabla_{\perp}^2 U + i \frac{\omega_0}{c} n_2 |U|^2 U = 0, \quad (48)$$

describes the self-focusing of optical wave-packets with $n_2 > 0$ (Askar'yan, 1962; Marburger, 1975). Self-focusing is a nonlinear phenomenon common to several branches of physics. In optics, it intervenes through the refractive optical index $N_{\text{opt}} = n_0 + n_2 I$ that increases with the field intensity and forces light rays to refract onto the axis. This causes a compression of the beam in the diffraction

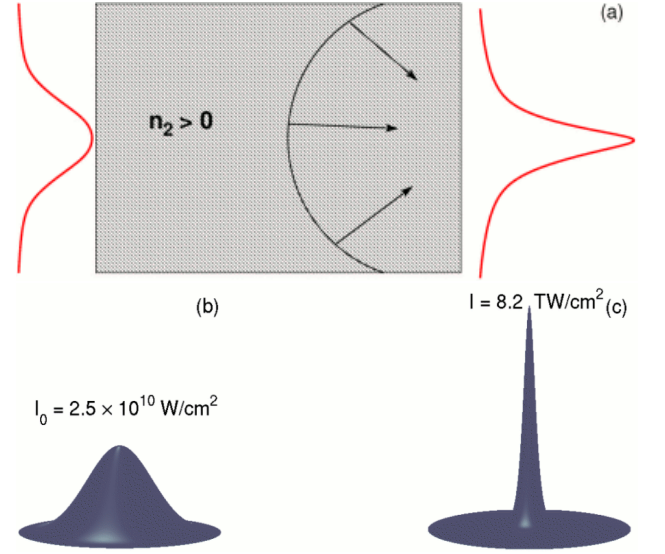


FIG. 4 (a) Principle of wave self-focusing. Insets (b) and (c) detail some intensity profiles of the solution to Eq. (48), applied to silica ($n_2 = 3.2 \times 10^{-16} \text{ cm}^2/\text{W}$). The initial condition is the Gaussian pulse (46) where $f = +\infty$, $w_0 = 130 \mu\text{m}$, $P_{\text{in}}/P_{\text{cr}} = 3$, $t_p = 85 \text{ fs}$ and $C = 0$.

plane, which leads to "wave collapse" when the Kerr non-linearity is not saturated. A necessary condition for the collapse is that the input power $P_{\text{in}} = \int |\mathcal{E}|^2 d\vec{r}$ exceeds some critical value,

$$P_{\text{cr}} \simeq \frac{3.72 \lambda_0^2}{8\pi n_0 n_2}, \quad (49)$$

computed on the Townes mode (see below). The beam waist decreases more and more, as the field amplitude $|U|$ diverges. Figure 4 illustrates the self-focusing principle taking place in purely Kerr media. The two insets detail the collapsing evolution of a Gaussian wave-packet with initial condition (46) at $z = 0$ and near the collapse distance z_c . This distance, also termed as "nonlinear focus", locates the point at which the beam amplitude diverges along the optical path. It is given by the well-known semi-empirical Marburger formula (Marburger, 1975)

$$z_c = \frac{0.367 z_0}{\sqrt{\left(\sqrt{\frac{P_{\text{in}}}{P_{\text{cr}}}} - 0.852\right)^2 - 0.0219 + \frac{z_0}{f}}}. \quad (50)$$

Below we briefly review properties of wave collapse and how self-focusing is affected by temporal dispersion and plasma generation. In order to argue on the relevant mechanisms participating in this process, we discard non-resonant terms causing harmonic generation and consider an instantaneous cubic response ($x_K = 0$). We apply the approximation $T^{-1} \simeq 1 - (i/\omega_0) \partial_t$ supposing $\omega_0 t_p \gg 1$, neglect recombination and treat the plasma coupling term driven by MPI only and subject to the limit $T^{-1} \rightarrow 1$. Equations (45) are then rescaled in dimensionless form by using the substitutions $r \rightarrow \omega_0 r$,

$t \rightarrow t_p t$, $z \rightarrow 4z_0 z$, $U \rightarrow \sqrt{c_2} \psi$ and $\rho \rightarrow (n_0^2 \rho_c / 2z_0 k_0) \rho$, where $c_2 \equiv \lambda_0^2 / 8\pi^2 n_0 n_2 \omega_0^2$. They result into the extended nonlinear Schrödinger (NLS) equation

$$i\partial_z \psi + \nabla_{\perp}^2 \psi + |\psi|^2 \psi + \mathcal{F}(\psi) = 0, \quad (51a)$$

$$\begin{aligned} \mathcal{F} = & -\delta \partial_t^2 \psi - \rho \psi - \epsilon |\psi|^4 \psi + i\nu |\psi|^{2K-2} \psi \\ & + \frac{i(|\psi|^2 \psi - \nabla_{\perp}^2 \psi)_t}{t_p \omega_0}, \quad \partial_t \rho = \Gamma |\psi|^{2K}, \end{aligned} \quad (51b)$$

where $\mathcal{F}(\psi)$ includes "perturbations" of a critical collapse, such as GVD, MPI, nonlinear saturation, MPA and pulse steepening. GVD and MPA have the normalized coefficients $\delta \equiv 2z_0 k'' / t_p^2$ and $\nu = 2z_0 \beta^{(K)} c_2^{K-1}$, respectively. Quintic saturation is taken into account through $\epsilon = n_4 c_2 / n_2$. The rescaled MPI coefficient reads as $\Gamma = (2z_0 k_0 / n_0^2 \rho_c) \sigma_K \rho_{nt} t_p c_2^K$. For Gaussian beams, the incident amplitude (46) reduces to

$$|\psi(z=0)| = \sqrt{\frac{16\pi n_0 n_2 P_{in}}{\lambda_0^2}} e^{-r^2 - t^2}. \quad (52)$$

1. Principles of wave self-focusing

With a purely cubic nonlinearity, solutions to the Cauchy problem (51a) can blow-up (or collapse) at finite distance (Kelley, 1965; Sulem and Sulem, 1999). To describe this singular process, let us consider the NLS equation (51a) with $\mathcal{F} = \partial_t^2 \psi$ ($\delta = -1$), so that the Laplacian $\vec{\nabla}_{\perp}^2 \rightarrow \vec{\nabla}^2 = \partial_x^2 + \partial_y^2 + \partial_z^2 + \dots$ formally accounts for the dispersion of a wave-packet along D orthogonal spatial axes [$\vec{r} = (x, y, t, \dots)$]. The wavefunction ψ evolves from the spatially-localized initial datum $\psi(\vec{r}, 0) \equiv \psi_0(\vec{r})$, assumed to belong to the Hilbert space H^1 with finite norm $\|\psi\|_{H^1} = (\|\psi\|_2^2 + \|\vec{\nabla} \psi\|_2^2)^{1/2}$, where $\|f\|_p \equiv (\int |f|^p d\vec{r})^{1/p}$. Two invariants are associated with ψ , namely, the L^2 norm (power) P and Hamiltonian H :

$$P = \|\psi\|_2^2, \quad H = \|\vec{\nabla} \psi\|_2^2 - \frac{1}{2} \|\psi\|_4^4. \quad (53)$$

The following "virial" equality can be established (Glasse, 1977; Vlasov *et al.*, 1974)

$$P d_z^2 \langle r^2 \rangle = 4\{2H + (1 - D/2)\|\psi\|_4^4\}, \quad (54)$$

where $\langle r^2 \rangle = \int r^2 |\psi|^2 d\vec{r} / P$ denotes the mean-squared radius of the solution ψ . By a double integration in z , Eq. (54) shows that, whenever $D \geq 2$, there exist initial conditions for which $\langle r^2 \rangle$ vanishes at finite distance, which is the sufficient signature of a wave collapse. For finite norms P , the inequality $P \leq (4/D)^2 \langle r^2 \rangle \times \|\vec{\nabla} \psi\|_2^2$ thus implies that the gradient norm diverges in collapse regimes. As H is finite, the collapse dynamics makes the L^4 norm $\|\psi\|_4^4$ blow up in turn and $\max_r |\psi|$ diverges accordingly, by virtue of the mean-value theorem $\int |\psi|^4 d\vec{r} \leq \max_r |\psi|^2 \times P$ (Kuznetsov, 1996). This leads to a finite-distance blow-up, at which the solution

ψ stops to exist in H^1 (Rasmussen and Rypdal, 1986). This mathematical singularity reflects the ultimate issue of the nonlinear self-focusing in the absence of saturation of the Kerr response and under the paraxiality assumption.

While $H < 0$ arises from Eq. (54) as a sufficient condition for collapse, sharper requirements can be derived by means of the Sobolev inequality

$$\|\psi\|_4^4 \leq C \|\vec{\nabla} \psi\|_2^D \times \|\psi\|_2^{4-D}. \quad (55)$$

In the critical case $D = 2$, this inequality can be used to bound H from below, so that the gradient norm blows up only if P fulfills the constraint $P > P_c$. The best constant in Eq. (55) is exactly $C_{\text{best}} = 2/P_c$ and it involves the quantity $P_c = \int R^2 d\vec{r} = 11.68$, where R is the radially-symmetric soliton solution, called the "Townes mode", of $-R + r^{-1} \partial_r r \partial_r R + R^3 = 0$ (Chiao *et al.*, 1964; Weinstein, 1983). P_c justifies the existence of a critical power for the 2D self-focusing of optical beams in nonlinear Kerr media. In the supercritical case $D = 3$, a criterion for collapse, sharper than $H < 0$, can be established from a combination of Eqs. (54) and (55) as $H < P_c^2 / P$ for gradient norms initially above $3P_c^2 / P$ (Kuznetsov *et al.*, 1995). Here, P_c again corresponds to the mass of the 3D soliton satisfying $-R + r^{-2} \partial_r r^2 \partial_r R + R^3 = 0$.

Once collapse is triggered, the solution focuses self-similarly near the singularity point z_c as (Rypdal *et al.*, 1985)

$$\psi(\vec{r}, z) = L^{-1}(z) \phi(\vec{\xi}, \zeta) e^{i\lambda \zeta + iLL_z \xi^2 / 4}, \quad (56)$$

where $\vec{\xi} = \vec{r} / L(z)$, $\zeta(z) \equiv \int_0^z du / L^2(u)$ and the parameter λ is positive for making the new wavefunction ϕ localized. The function $L(z)$ represents the scale length that vanishes as collapse develops, and ϕ converges to an exactly self-similar form $\phi(\vec{\xi})$ fulfilling $\partial_{\zeta} \phi \rightarrow 0$. For radial solutions Eq. (51a) transforms into

$$i\partial_{\zeta} \phi + \xi^{1-D} \partial_{\xi} \xi^{D-1} \partial_{\xi} \phi + |\phi|^2 \phi + \beta [\xi^2 - \xi_T^2] \phi = 0, \quad (57)$$

where $\xi_T^2 \equiv \beta^{-1} [\lambda - iLL_z (\frac{D}{2} - 1)]$ is viewed as a complex turning point, with $\beta \equiv -\frac{1}{4} L^3 L_{zz}$. As $L(z) \rightarrow 0$, ϕ can be treated by means of quasi-self-similar techniques (Bergé, 1998). The solution ϕ is split into a nonlinear core, ϕ_c , extending in the range $\xi \ll \xi_T$, and a linear tail, $\phi_T \sim e^{-\lambda \pi / \beta} / \xi^{1+i\lambda/\beta}$, defined in the complementary spatial domain $\xi \gg \xi_T$ where the nonlinearity vanishes. The length $L(z)$ is then identified from the continuity equation describing the mass exchanges between the core and tail parts of ψ . The dynamics of self-similar collapses vary with the space dimension number as follows.

- For $D = 2$, $L(z)$ has a twice-logarithmic correction: $L(z) \simeq L_0 \sqrt{z_c - z} / \sqrt{\ln \ln [1/(z_c - z)]}$ (Fraïman, 1985; Landman *et al.*, 1988; Malkin, 1990). As $z \rightarrow z_c$, the exponential contribution of the tail decreases to zero, while the core converges to the Townes mode R . The power P relaxes to the

critical value P_c and stays mostly located around the center. Self-similar relaxation of self-focusing beams to the Townes mode has been reported experimentally (Moll *et al.*, 2003).

- For $D = 3$, β attains a fixed point $\beta_0 \neq 0$, leading to the scaling law $L(z) \simeq L_0 \sqrt{z_c - z}$. The power is no longer preserved self-similarly in space, since $P = L(z) \int |\phi|^2 d\vec{\xi}$. This integral behaves as $P \simeq P_{\text{core}}(z) + P_{\text{tail}}(z)$, where $P_{\text{core}}(z) \sim L(z)$ vanishes, while $P_{\text{tail}}(z)$ contains almost all the initial mass as $L(z) \rightarrow 0$. A 3D collapse is thus accompanied by an expulsion of mass towards the large distances where it keeps a stationary density $r^2 |\psi|^2 \rightarrow \text{const}$ (Kosmatov *et al.*, 1991; leMesurier, 2000; Vlasov *et al.*, 1989; Zakharov and Kuznetsov, 1986).

2. Variational approaches

Because the cubic NLS equation is not integrable at high dimension numbers $D \geq 2$, approximation methods describing the fate of singular solutions may be employed. Among those, "variational approaches" consist in building a set of dynamical equations governing the size, amplitude and phase of the beam. These beam parameters are evaluated from functional integrals (Action or Lagrangian integrals) computed from a given trial function, which the pulse is supposed to keep along the optical path. Such methods give global, qualitative behaviors within a pedestrian way. Their principal drawback is that, as they need to fulfill the main conservation laws (e.g., preservation of the L^2 norm), they capture the entire initial mass of the solution and do not let the latter evacuate radiation to the boundaries or relax to an exact ground state. This discrepancy may partly be cured by accounting for corrective damping of the nonlinear core (Arévalo and Becker, 2005; Kath and Smyth, 1995), but improvements become rapidly tricky and limited. Variational principles applied to NLS solutions were extensively studied (Anderson, 1983; Anderson and Bonnedal, 1979; Anderson *et al.*, 1979; Bondeson *et al.*, 1979; Desaix *et al.*, 1991) and further exploited in different contexts (Cerullo *et al.*, 1996; Karlsson *et al.*, 1992; Manassah, 1992; Manassah *et al.*, 1988; Pietsch *et al.*, 1991; Silberberg, 1990; Vidal and Johnston, 1997). They were also widely worked out by several authors in the present scope (Couairon, 2003b; Esarey *et al.*, 1997; Lehner and Auby, 2000; Sprangle *et al.*, 1996).

For example, considering the shape (46) with $N = 1$, a Gaussian trial function in the form

$$\psi = \frac{\sqrt{\mathcal{J}(z)}}{L(z)\sqrt{T(z)}} \phi(\xi_{\perp}, \eta) e^{i\frac{L_z L}{4}\xi_{\perp}^2 - i\frac{T_z T}{4\delta}\eta^2} \quad (58)$$

with $\phi = e^{-\xi_{\perp}^2/2 - \eta^2/2 + i\theta(z)}$, $\xi_{\perp} = r/L(z)$, $\eta = t/T(z)$ can be employed in the virial identities governing the transverse and temporal mean squared extents

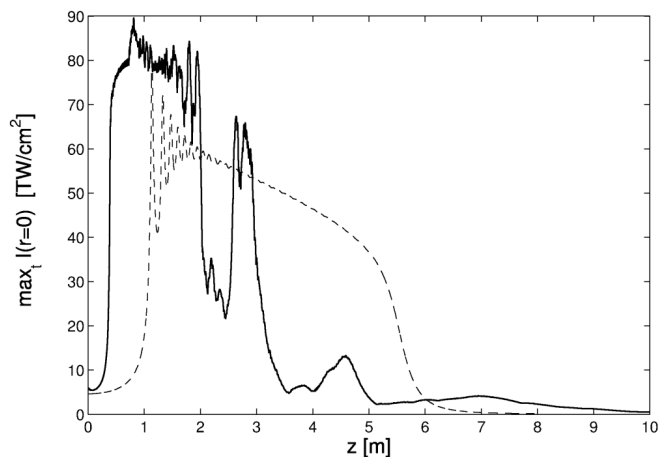


FIG. 5 Peak intensities for a 1 mm-waisted, 100-fs collimated Gaussian pulse with 22 critical powers. Dashed line: Results from Eqs. (59) in the limits $T, T^{-1} \rightarrow 1$; Solid line: (3 + 1)-dimensional numerical simulations (initial conditions are perturbed by a 10% amplitude random noise).

(Bergé and Couairon, 2000; Sprangle *et al.*, 2002). Separate dynamical systems for the transverse width $[L(z)]$, the temporal duration $[T(z)]$ and the intensity factor $[\mathcal{J}(z)]$ of the pulse are then analytically established as

$$\frac{L_{zz}}{4} = \frac{1}{L^3} - \frac{\mathcal{J}T(0)}{4TL^3} + \frac{\Gamma\sqrt{\pi K}\mathcal{J}^K}{2(K+1)^2 L^{2K+1} T^{K-1}} + \dots \quad (59a)$$

$$\frac{T_{zz}}{4} = \frac{\delta^2}{T^3} + \frac{\delta\mathcal{J}T(0)}{4L^2 T^2} + \dots, \quad (59b)$$

$$\mathcal{J}_z = -\frac{2\nu}{K^{3/2}} \frac{\mathcal{J}^K}{(L^2 T)^{K-1}} + \dots \quad (59c)$$

where final dots formally omit contributions from MPA, Raman-delayed, quintic and steepening effects. With $\mathcal{J}(0) = 2\sqrt{2}P_{\text{in}}/P_{\text{cr}}$ imposed by the initial power, Eqs. (59) yield qualitative behaviors for the propagation of a single femtosecond pulse preserving its cylindrical symmetry. It, of course, cannot depict any temporal or spatial splitting phenomenon, but offers a global evolution of the beam intensity. This evolution fairly supports the comparison with (3 + 1)-dimensional numerical simulations (Champeaux and Bergé, 2005), apart from an overestimated nonlinear focus. Figure 5 shows an example of peak intensity reached by Gaussian pulses with parameters $P_{\text{in}}/P_{\text{cr}} = 22$, $w_0 = 1$ mm, $t_p = 100$ fs at the wavelength $\lambda_0 = 800$ nm in the limit $T \rightarrow 1$ and dispersion limited to GVD. Collapse is arrested by plasma generation. The dashed curve corresponds to the solution reconstructed from the two-scale variational method. The solid one shows the result obtained from numerical integration of the propagation equations.

Besides, alternative procedures, such as perturbative methods, may provide qualitative information about

the changes in the scale $L(z, t)$ induced by contributions that can stop the collapse. Here, the radial size $L(z, t)$ tends to zero in the diffraction plane as $z \rightarrow z_c$, but it now depends on time. The principle is to perturb a collapsing state that naturally tends to the Townes mode R , by means of L^2 orthogonal perturbative modes. These will provide an integral relation for the z -dependent function β [Eq. (57)], directly depending on \mathcal{F} (Fibich and Papanicolaou, 1999). At the critical dimension, the zeroth-order collapsing solution, whose core converges as

$$\psi \rightarrow \psi_s = L^{-1} R(\vec{r}/L) \exp(i\zeta + iL_z r^2/4L), \quad (60)$$

has its mean radius $L(z, t)$ modified by the perturbation $|\mathcal{F}| \ll 1$. Appropriate functions \mathcal{F} are then capable of turning the sign of $\beta = -\frac{1}{4}L^3 L_{zz}$ from positive to negative, which predicts the arrest of collapse. This method was applied to many "perturbations" of NLS, such as normal GVD, steepening and non-paraxial deviations (Fibich, 1996; Fibich and Papanicolaou, 1997) as well as for NLS with attractive potentials (leMesurier *et al.*, 2004; Schjdt-Eriksen *et al.*, 2001a). It was later extended to a variational system formally avoiding the constraints $\epsilon, \beta, \mathcal{F} \ll 1$ by introducing an amplitude factor accounting for dissipative losses, $\psi \rightarrow \sqrt{\mathcal{J}(z, t)}\psi_s$ (Berg  and Couairon, 2001b). Applied to Eqs. (51) for pulses having a Gaussian distribution in time, this procedure involves the substitution

$$\psi \rightarrow \sqrt{\mathcal{J}(z, t)}\psi_s; \quad \mathcal{J}(z=0, t) = P_{\text{in}} e^{-2t^2}/P_{\text{cr}}, \quad (61)$$

and leads to the dynamical equations

$$\frac{M}{4P_c} L^3 L_{zz} = 1 - \mathcal{J} + 4\epsilon \frac{\mathcal{J}^2}{L^2} - \frac{L^2}{2P_c} \int R^2 \xi \partial_\xi \rho d\vec{\xi} \quad (62a)$$

$$\frac{\mathcal{J}_z}{\mathcal{J}} \simeq 2\delta\zeta_{tt} - 2\nu A \frac{\mathcal{J}^{K-1}}{L^{2K-2}} - \frac{B(L^{-2})_t}{t_p \omega_0}, \quad (62b)$$

where $M = \int \xi^2 R^2(\xi) d\vec{\xi}$, $A = \int R^{2K} d\vec{\xi}/P_c$, $B = 3\mathcal{J} + 1$, and $C = \int R^{2K+2} d\vec{\xi}/P_c$. Equation (62b) originates from the power variations, assuming $\mathcal{J}_z/\mathcal{J} \ll 1$. The first term refers to GVD, the second one to MPA and the last term corresponds to pulse steepening.

Figure 6 depicts the normalized maximum intensity and temporal pulse distortions driven by MPI alone at $z = 2.4$ cm for the solution to Eqs. (62) in the absence of dissipation ($\mathcal{J}_z = 0$). The Townes mode is here approached by a Gaussian profile for a beam containing 1.85 critical powers. The temporal dependencies in $L(z, t)$ alter the pulse profile. Note that discrepancies occur in the maximal amplitude, in the location of the first focus and in the temporal shapes. Because they rely on trial functions that capture the same power and shape as initial, variational procedures cannot accurately describe fluctuations in the wave envelope. They should therefore be employed for what they are, i.e., as qualitative procedures yielding first indications on the beam dynamics.

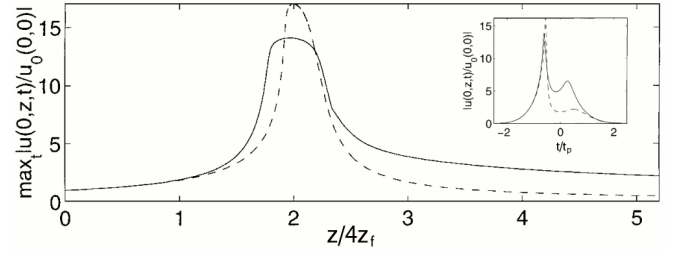


FIG. 6 Normalized maximum intensity of Gaussian pulses in argon with power of $1.85 P_{\text{cr}}$ integrated from Eqs. (62) (dashed curves) and from a numerical integration of Eqs. (45) (solid curves). Inset shows temporal profiles at $z = 2.4$ cm.

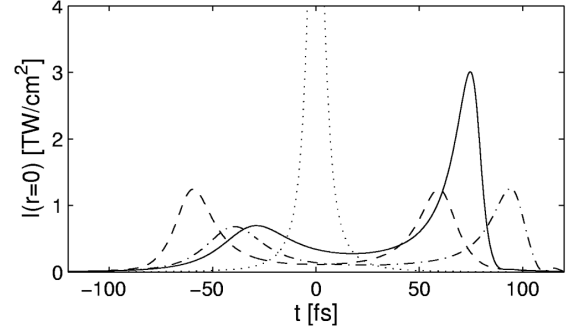


FIG. 7 Temporal profiles of Gaussian pulses ($w_0 = 130 \mu\text{m}$, $t_p = 85$ fs) near the nonlinear focus with power $P_{\text{in}} = 3P_{\text{cr}}$ for the Kerr response alone (dotted curve), for Kerr + normal GVD (dashed curve), for Kerr + GVD + T, T^{-1} (solid curve), for Kerr + GVD + T, T^{-1} + higher-order dispersion (dash-dotted curve). In all cases, plasma response is omitted.

B. Saturation by temporal dispersion

By mixing GVD and spatial diffraction when $T \simeq 1$, the Kerr nonlinearity causes defocusing in time for $k'' > 0$ (normal dispersion) and temporal compression for $k'' < 0$ (anomalous dispersion), besides wave focusing in the transverse direction. The interplay of these processes results in the symmetric splitting of the pulse along the time axis with normal GVD (Chernev and Petrov, 1992a,b) and to a 3D spatiotemporal collapse with anomalous GVD (Berg , 1998). In addition, when ultrashort pulses develop sharp temporal gradients, the operator T in front of the Kerr term (self-steepening) induces a shock dynamics: The field develops a singular profile with $|\psi_t| \rightarrow +\infty$ in the trail ($t > 0$) of the pulse (Anderson and Lisak, 1983). This dynamics is reinforced by space-time focusing (Rothenberg, 1992). Figure 7 depicts temporal profiles of pulses undergoing steepening effects in normally dispersive regime (silica glass at 790 nm), together with a transverse collapse.

To understand these dynamics, we can consider ultrashort pulses as being stacked along the temporal direction into different time slices having each their own power, e.g., $P(t) = P_{\text{in}} e^{-2t^2}$ for Gaussian profiles. Slices located at times $t < 0$ correspond to the front (or leading) pulse;

those at $t > 0$ constitute the back (trailing) pulse. Each time slice self-focuses at its respective singularity point, $z_c(t)$, according to Eq. (50) in which the ratio $P_{\text{in}}/P_{\text{cr}}$ must be replaced by $P_{\text{in}}e^{-2t^2}/P_{\text{cr}}$. This scenario is known as the "moving-focus" model (Lugovoi and Prokhorov, 1974; Shen, 1976) and yields simple comprehension elements to figure out the pulse distortions. Here, the central time slice focuses at the shortest distance $z_c(t = 0)$. Furthermore, $\dot{z}_c(t)$ is positive for $t > 0$ and negative for $t < 0$ [$\dot{z}_c(0) = 0$], whereas $\ddot{z}_c(t)$ always remains positive. Near the collapse distance, we can replace all time derivatives by $\partial_t = -\dot{z}_c\partial_z$, $\partial_t^2 = -\ddot{z}_c\partial_z + \dot{z}_c^2\partial_z^2$ (Fibich and Papanicolaou, 1997; Luther *et al.*, 1994b). Power fluctuations (62b) are then given by

$$\frac{\mathcal{J}_z^{\text{disp}}}{\mathcal{J}} = 2\delta[-\ddot{z}_c/L^2 + \dot{z}_c^2(1/L^2)_z] + \frac{2B}{\omega_0 t_p} \dot{z}_c(L^{-2})_z, \quad (63)$$

where $L_z < 0$ in compression regime. With $\delta > 0$, Eq. (63) describes defocusing around the central slice: Normal GVD transfers power towards non-zero instants, symmetrically located with respect to $t = 0$. Self-steepening and space-time focusing moreover produce a transfer of power from the leading ($\dot{z}_c < 0$) to the trailing portion of the pulse ($\dot{z}_c > 0$). This asymmetrizes the temporal profile, which was retrieved by direct experiments (Ranka and Gaeta, 1998). Normal GVD alone "splits" a focusing pulse into two regular, symmetric spikes at powers $< 2P_c$. For higher powers, the peak edges develop shock profiles and disintegrate into ripplelike cells (Fibich *et al.*, 2003; Germaschewski *et al.*, 2001). Because of the hyperbolicity of the operator $\nabla_{\perp}^2 - \delta\partial_t^2$, one splitting event transforms the optical field in the (r, t) plane into an X -shaped waveform (Bergé *et al.*, 2002; Christodoulides *et al.*, 2004; Conti *et al.*, 2003; Di Trapani *et al.*, 2003; Litvak *et al.*, 2000a,b; Zharova *et al.*, 2003).

Normal GVD ($k'' > 0$) and plasma formation compete at powers moderately above critical to halt the wave collapse. The stronger the GVD coefficient, the larger the power interval in which the collapse is arrested by pulse splitting. By solving the cubic NLS equation with normal GVD, a boundary $\delta_{\text{crit}}(\bar{p})$, function of the ratio of input power over critical, $\bar{p} = P_{\text{in}}/P_{\text{cr}}$, can be calculated in such a way that initial conditions fulfilling $\delta > \delta_{\text{crit}}(\bar{p})$ will limit the Kerr self-focusing through GVD splitting instead of letting the solution diverge into a singular state (Luther *et al.*, 1994a). Higher-order dispersion together with steepening effects (T, T^{-1}) modify this curve in the sense of "delaying" the self-focusing threshold to higher powers (Skupin and Bergé, 2006; Skupin *et al.*, 2006a). In particular, third-order dispersion tends to delocalize the pulse by pushing the temporal centroid to the back (Fibich and Ilan, 2004).

In contrast, for anomalous GVD ($k'' < 0$) power is transferred to center, as seen from Eq. (63) with $\delta < 0$. Ultrashort pulses thus collapse both in space and time. A mapping $|\delta| > \delta_{\text{crit}}(\bar{p})$ can again be constructed on the basis of virial-type arguments (Bergé and Skupin, 2005;

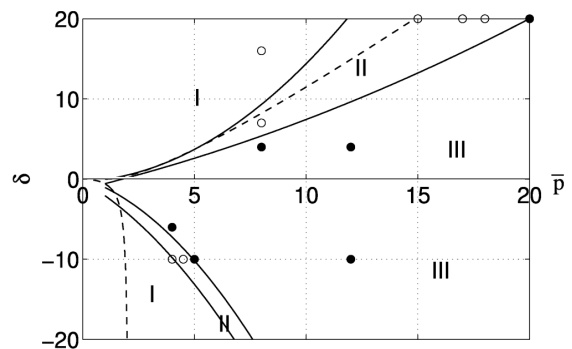


FIG. 8 Collapse regions in the plane (δ, \bar{p}) . The solid curves extrapolate results from the propagation equations. The dashed curves represent theoretical limits estimated from Eqs. (51), above which dispersion inhibits the self-focusing. Regions I, II and III are explained in the text.

Kuznetsov *et al.*, 1995). It predicts pulse spreading when the dispersion length $\sim t_p^2/|k''|$ is short enough to prevail over diffraction and Kerr nonlinearity. As for normal GVD, the theoretical boundaries are modified by higher-order dispersion and steepening terms to some extent.

Figure 8 summarizes the zone of collapse and no-collapse in the plane (δ, \bar{p}) for both normally and anomalously dispersive media computed from Eqs. (45). Open circles represent initial conditions that do not collapse. Close ones result in a strong divergence of the beam intensity. Three zones clearly occur: (I) A dispersion-dominated domain leading to pulse spreading; (II) A transition zone in which GVD and steepening operators inhibit the self-focusing; (III) A Kerr-dominated region, in which chromatic dispersion is unable to stop the wave blow-up. Here, the field intensity can increase by several decades before reaching the ionization threshold. Note that for anomalous GVD, the collapse process, which encompasses spatial and temporal compressions, makes the intermediate zone II almost meaningless.

C. Saturation by plasma defocusing

The action of MPI is to deplete the pulse temporal profile through the sudden emergence of an ionization front near the focus point z_c . In the absence of time dispersion and nonlinear losses, the plasma equation $\partial_t \rho = \Gamma|\psi|^{2K}$ can be integrated with the *ansatz* (61) as

$$\rho(r, t, z) \simeq \sqrt{\frac{\pi}{8K}} \Gamma \left(\frac{P_{\text{in}} R^2}{P_{\text{cr}}} \right)^K \frac{\text{Erf}(\sqrt{2K}t) + 1}{L^{2K}(z, t)}, \quad (64)$$

where $\text{Erf}(x) = (2/\sqrt{\pi}) \int_0^x e^{-u^2} du$ denotes the error function. The last term of Eq. (62a) then scales as $L^{2(1-K)}\partial_{\xi}\rho$ where $\partial_{\xi}\rho \sim \partial_{\xi}R^{2K}$ is negative. As $L \rightarrow 0$, this term efficiently competes with the Kerr contribution $\mathcal{J} \sim P_{\text{in}}e^{-2t^2}/P_{\text{cr}}$. With the step function $\text{Erf}(\sqrt{2K}t)+1$, the plasma response arises like a defocusing plateau, as the field intensity reaches its maximum near the focus

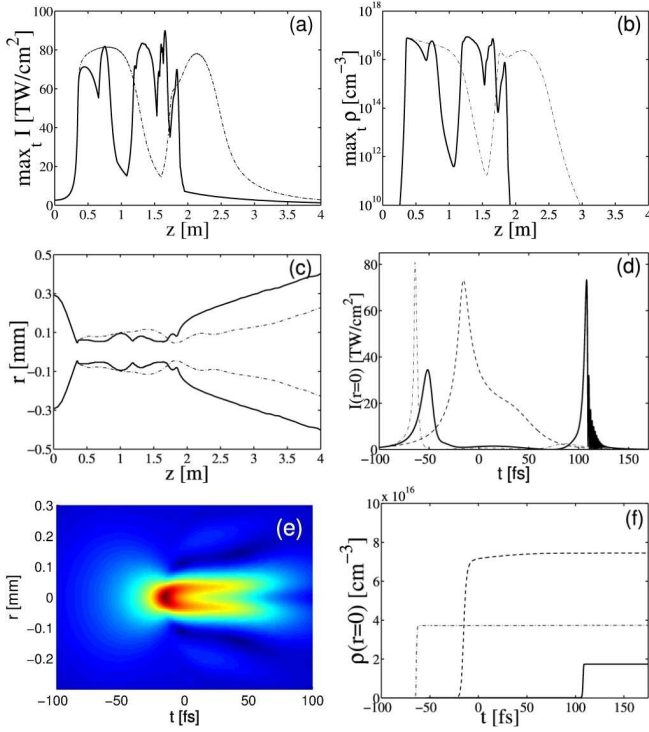


FIG. 9 (a) Maximum intensity, (b) peak electron density and (c) mean radius (FWHM of the fluence) of a 150-fs, 0.5 mm-waisted Gaussian pulse with $4P_{cr}$ in air at $\lambda_0 = 800$ nm. Dash-dotted curves refer to the case when $T, T^{-1} = 1$ and chromatic dispersion is limited to GVD ($k'' = 0.2$ fs²/cm). Solid curves refer to the full model (45). (d) Temporal profiles at $z = 0.8$ m. The dashed curve refers to the distribution at $z = 0.4$ m (identical for both models). (e) Radial profile vs time near z_c . (f) Plasma responses associated with (d).

point z_c . All time slices belonging to the interval $t > 0$ are defocused. At negative times, the pulse continues to self-focus and feeds plasma defocusing until forming a single time slice located near $t = t^* \simeq -[\ln \sqrt{P_{in}/P_{cr}}]^{1/2}$ at powers close to critical (Bergé and Couairon, 2001a; Henz and Herrmann, 1999). Thus, plasma generation is accompanied by a sharp duration shortening of the pulse (see, e.g., inset of Fig. 6).

When GVD and MPA come into play, the leading peak becomes unstable and refocusing of the trail occurs at high enough input powers. With MPA, the leading component is partly damped in the intensity ratio $\mathcal{J}_z/\mathcal{J} \simeq -2\nu A(\mathcal{J}/L^2)^{K-1}$, as the peak electron plasma forms a density plateau [see Eq. (62b)]. Consequently, the electron density attains much lower levels and permits the emergence of a trail. This complex dynamics leads to two following signatures for plasma defocusing: (i) MPI shortens the pulse duration near the nonlinear focus; (ii) Because ρ scales as R^{2K} , the spatial zone of plasma defocusing takes place inside a narrow region ($\sim 1/\sqrt{K}$ times the beam width) of the intensity distribution, which creates spatial rings. This "self-guiding" mechanism is therefore not static. Certain pulse compo-

nents are defocused to the benefit of the others. To clear it up, Figure 9 depicts focusing/defocusing cycles affecting the peak intensity, electron density, beam radius and the distribution in space and time of a 150-fs pulse for atmospheric propagation. Note the rings formed just at the stage of plasma defocusing [Fig. 9(e)] and the occurrence of a sharp trail when steepening effects (T, T^{-1}) are included [Fig. 9(d)].

D. Saturation by optical nonlinearities

Additional defocusing quintic nonlinearities produce stable solitons in continuous-wave (cw) media (Trillo and Torruellas, 2001). This property follows from a balance between diffraction, Kerr focusing and nonlinear saturation. When a quintic contribution is added ($\mathcal{F} = -\epsilon|\psi|^4\psi$), the beam starts to self-focus and evacuates part of power into diffracting components to reach a stable ground state of Eqs. (51) (Gatz and Herrmann, 1997; Kolokolov, 1976; Malkin, 1993; Vakhitov and Kolokolov, 1975; Vidal and Johnston, 1996). This property is partly reflected by Eqs. (62) emphasizing an arrest of collapse like $\beta = -\frac{1}{4}L^3L_{zz} \sim 1/L^2$, which induces regular oscillations of the size $L(z)$ beyond the focus point.

Reframed in the present context, several papers addressed the question of limiting self-focusing by nonlinear optical saturations, instead of relying on plasma generation alone (Gaeta and Wise, 2001; Koprinkov *et al.*, 2000, 2001). In fact, it appears that the weight of $\chi^{(5)}$ susceptibility depends on the actual pulse length, on the ratio of instantaneous over delayed Kerr responses and on the ionization sources, that influence the maximum intensity attained by the beam (Aközbek *et al.*, 2001; Couairon, 2003a; Vinçotte and Bergé, 2004). This property can be seen from the zeroes of the nonlinear refraction index

$$\Delta n = [(1 - x_K) + x_K G(t)]|\psi|^2 - \epsilon|\psi|^4 - \rho, \quad (65)$$

in which the Raman-delayed response has been introduced by changing the Kerr term $|\psi|^2$ of Eqs. (51) into $[(1 - x_K) + x_K G(t)]|\psi|^2$. Here, the function $G(t)$ follows from computing the integral $\int h(t - t')|\psi(t')|^2 dt' \sim G(t)|\psi|^2$ over the initial pulse profile (52). High-order saturation prevails over ionization and induces a soliton-like dynamics at high enough values of n_4 , before the occurrence of an electron plasma. Relevance of higher-order optical nonlinearities above all depends on the ionization rate: For example in air, if the laser intensity saturates above 10^{14} W/cm² by plasma generation alone, then even weak values of n_4 can soften this peak intensity. At lower intensities, quintic saturation has a more limited role. For instance, Fig. 10 displays the peak intensities, beam radius (FWHM of the fluence distribution), maximum electron density and energy losses of a 70-fs, 0.5 mm-waisted unchirped Gaussian pulse propagating in parallel geometry in air. Limitation of the

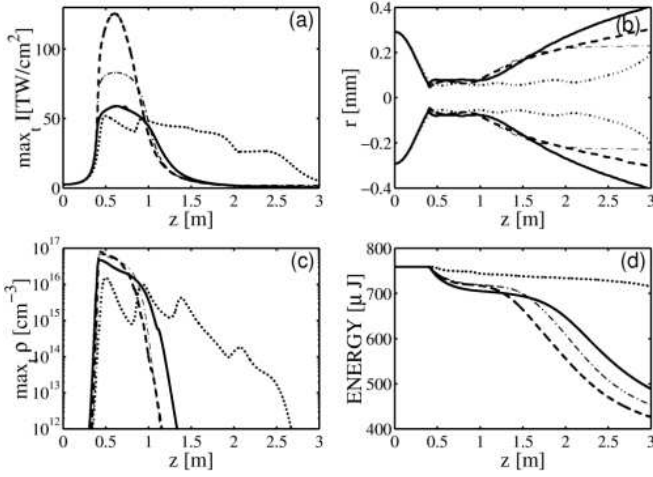


FIG. 10 (a) Peak intensities, (b) pulse radii, (c) electron density and (d) energy losses for Gaussian pulses with $w_0 = 0.5$ mm, $t_p = 70$ fs, $T = T^{-1} = 1$ and different ionization models: PPT (solid curves), ADK molecular (dashed curves), ADK molecular + $\chi^{(5)}$ susceptibility (dotted curves) and the MPI-like approximation of Fig. 2 (dash-dotted curves).

pulse growth depends on the ionization model employed. One of them involves the ADK molecular rate without (dashed curve) and with (dotted curve) a weak quintic saturation ($n_4 = 2.5 \times 10^{-33}$ cm⁴/W²). The measured intensity peak of 5×10^{13} W/cm² is refound in the latter configuration. $\chi^{(5)}$ susceptibility lowers the peak intensity and density, which stays close to 10^{16} cm⁻³. Energy losses are weaker, which increases the self-guiding range.

Other high-order effects may soften the Kerr focusing of nonlinear waves. For instance, the Raman response function (27) becomes all the weaker as the pulse is short, which affects the critical power for self-focusing like $P_{cr} \rightarrow P_{cr}/[1 - x_K + x_K G(t)]$ (Ting *et al.*, 2005a). Unlike long pulses, for which $G(t) \rightarrow 1$, the non-instantaneous nonlinearity reduces the effective value of the Kerr index and results in delaying the nonlinear focus from which a filament emerges (Aközbek *et al.*, 2001; Chiron *et al.*, 1999; Liu and Chin, 2005). In connection, modulational instabilities have their growth rate decreasing as the ratio x_K is augmented (Wyller, 2001).

Besides, the cubic polarization $\sim E^3$ generates third-order harmonics as

$$E \rightarrow U_\omega e^{ik(\omega)z - i\omega t} + \tilde{U}_{3\omega} e^{ik(3\omega)z - 3i\omega t} + c.c. \quad (66)$$

at $\omega = \omega_0$ (Agrawal, 2001). Two coupled equations can then be derived under the basic assumptions of slowly-varying envelopes and narrow-spectral bandwidths $\Delta\omega_j/\omega_j \ll 1$ ($j = \omega, 3\omega$). The coupling is insured by cross-phase modulation (XPM) and four-wave mixing (FWM) induced by the cubic nonlinearity. By substituting $\tilde{U}_{3\omega} \rightarrow U_{3\omega} e^{i\Delta k z}$, where $\Delta k = 3k(\omega) - k(3\omega)$ is the linear wavevector mismatch parameter, the propagation equations read like Eq. (51) where the function \mathcal{F} for the

two components U_ω and $U_{3\omega}$ must be adapted as

$$\mathcal{F}_\omega \rightarrow \mathcal{F}_\omega + 2|\psi_{3\omega}|^2 \psi_\omega + (\psi_\omega^*)^2 \psi_{3\omega}, \quad (67a)$$

$$\mathcal{F}_{3\omega} \rightarrow \mathcal{F}_{3\omega} + 2|\psi_\omega|^2 \psi_{3\omega} + \frac{\psi_\omega^3}{3} + \left(\frac{i}{\Delta v} \partial_t - \frac{\Delta k}{(4z_0)^{-1}}\right) \psi_{3\omega}, \quad (67b)$$

that includes the group-velocity mismatch responsible for temporal walk-off, $\Delta v = [v_g(3\omega)^{-1} - v_g(\omega)^{-1}]^{-1}$. In self-focusing regimes, the third-harmonic intensity usually contributes by a little percentage to the overall beam fluence (Aközbek *et al.*, 2002). Despite the smallness of the TH field, this component may act as a saturable nonlinearity for the pump component when the term containing $|\Delta k|$ has an order of magnitude comparable with the FWM and XPM terms, $\psi_{3\omega} \sim \psi_\omega^3 / (3(4z_0|\Delta k| + 2|\psi_\omega|^2))$, and all other contributions driving the TH component are neglected. Once inserted into the pump wave equation, this so-called "cascading" limit (Buryak *et al.*, 1999) introduces a saturable quintic nonlinearity that lowers the peak intensity and enhances the propagation over longer distances (Bergé *et al.*, 2005).

So far, we have been dealing with linearly-polarized waves. However, by writing the electric field as $\mathcal{E} = (\mathcal{E}_x, \mathcal{E}_y)$, each polarization component undergoes optical nonlinearities as

$$P_{NL} \sim |\psi_j|^2 \psi_j + \frac{2}{3} |\psi_k|^2 \psi_j + \frac{1}{3} \psi_j^2 \psi_k^*, \quad (68)$$

with $j, k = x, y$ ($j \neq k$). A linearly-polarized state is described by the single-component NLS equation with, e.g., $\psi_y = 0$. A circularly-polarized state corresponds to the configuration $\psi_y = \pm i\psi_x$. In between, elliptically-polarized states facilitate energy transfers through the phase-dependent terms $\psi_j^2 \psi_k^*/3$ from one orthogonal component to the other (Schjødt-Eriksen *et al.*, 2001b). These energy transfers increase the power threshold for self-focusing (Bergé *et al.*, 2003). For circular polarization, the collapse threshold for the total power $P = \int (|\psi_x|^2 + |\psi_y|^2) d\vec{r}$ is increased by a factor 3/2 when passing from linearly- to circularly-polarized geometries. In addition, circular polarizations on femtosecond filaments self-channeling in the atmosphere produce stabler patterns than those issued from linear polarization (Kolesik *et al.*, 2001). They moreover weaken the MPI efficiency and decrease ion signals by a couple of decades in the fluorescence of N_2 molecules collected from infrared pulses (Petit *et al.*, 2000).

Compared with plasma formation and chromatic dispersion, quintic saturation and polarization effects have a limited impact on the nonlinear dynamics. Therefore, we shall henceforth focus on the first two players mainly.

E. Self-phase modulation and supercontinuum generation

The Kerr effect creates spectral broadening through self-phase modulation (SPM). The solving for $i\partial_z \psi =$

$-|\psi|^2\psi$ indeed yields the exact solution $\psi = \psi_0 e^{i|\psi_0|^2 z}$ [$\psi_0 \equiv \psi(z=0)$], which describes a self-induced phase modulation experienced by the optical field during its propagation. This intensity-dependent phase shift is responsible for spectral broadening by virtue of the relation $\Delta\omega = -\partial_t \arg(\psi)$ (Agrawal, 2001; Shen, 1984). Because the frequency spectrum is expanded by the nonlinearity, SPM leads to supercontinuum generation and white-light emission, as the wave intensity strongly increases through the self-focusing process. With plasma generation, this phenomenon can be described by employing the following approximations. First, we assume that the MPI response behaves like a static density plateau [see, e.g., Fig. 9(f)], so that the ratio $\rho/|\psi|^2$ is either zero or close to unity with $\partial_z(\rho/|\psi|^2) \simeq 0$. Second, omitting GVD and MPA for simplicity we retain self-steepening to the detriment of space-time focusing, i.e., we neglect diffraction in Kerr-dominated regimes. Phase and amplitude of solutions $\psi = Ae^{i\varphi}$ to Eq. (51a) satisfy $\varphi_z + \frac{A^2}{t_p\omega_0}\partial_t\varphi = A^2 - \rho$ and $A_z + \frac{3}{t_p\omega_0}A^2\partial_t A = 0$, respectively. If we model the pulse initially located at $t = t_0$ by $A^2 = A_0^2/\cosh(\tau)$, $\tau = (t - t_0)/\tau_0$, and suppose that the amplitude does not change too much, then

$$A^2 \simeq A_0^2/\cosh(\tau - 3QA^2/A_0^2), \quad (69a)$$

$$\begin{aligned} \varphi \simeq t_p\omega_0\tau_0 \int_{-\infty}^{\tau} \left(1 - \frac{\rho}{A^2}\right) d\tau' \\ - t_p\omega_0\sinh^{-1}[\sinh(\tau) - Q], \end{aligned} \quad (69b)$$

where $Q \equiv zA_0^2/t_p\omega_0\tau_0$ is linked to self-steepening. These expressions yield the spectral broadening

$$\frac{\Delta\lambda}{\lambda_0} \simeq 1 - \frac{\rho}{A^2} - \left[1 + \frac{Q^2 - 2Q\sinh(\tau)}{\cosh^2(\tau)}\right]^{-1/2}, \quad (70)$$

valid under the basic assumption $\Delta\omega/\omega_0 = -\Delta\lambda/\lambda_0 \ll 1$. As long as $Q \ll 1$ and in the absence of MPI, variations in wavelength $\Delta\lambda/\lambda_0 \approx -Q\sinh(\tau)/\cosh^2(\tau)$ starting with $t_0 = 0$ represent the early symmetric broadening through SPM (Yang and Shen, 1984). When MPI forms a defocusing plateau, $\Delta\lambda/\lambda_0$ then becomes larger in the region where $\rho = 0$ (non-defocused leading pulse), than when $\rho \rightarrow A^2$ (defocused trail). Consequently, as the beam reaches the first focus point z_c , the dominant part of the pulse is the front edge ($\rho = 0$) and MPI creates a primary redshift (Lehner and Auby, 2000). In the trail, full plasma coupling ($\rho/A^2 \rightarrow 1$) limits the spectral enlargement to the opposite side. However, self-steepening induced at increasing Q inhibits the MPI redshifting and instead displaces more the spectrum to the blue side. As a result, this creates an asymmetric spectral broadening with a prominent blueshift $\Delta\lambda < 0$ for $\tau > 0$ (Berkovsky *et al.*, 2005; Champeaux and Bergé, 2003; Gaeta, 2000; Ward and Bergé, 2003; Yang and Shen, 1984).

Figure 11 shows spectral modifications around 790 nm induced by SPM affected by space-time focusing

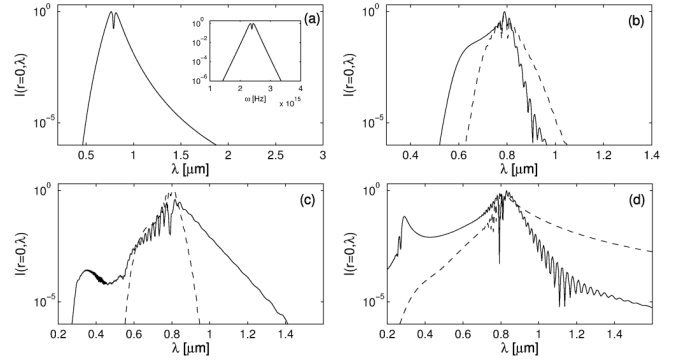


FIG. 11 Spectral broadening induced by SPM and steepening effects in fused silica: (a) with purely cubic nonlinearity (inset shows the spectrum in frequency for comparison), (b) with Kerr + GVD only (dashed curve) and when adding space-time focusing and self-steepening (solid curve) for $P_{in} = 3P_{cr}$, (c) same with plasma generation that remains inefficient at this power level (dashed curve, see Fig. 8), but strongly affects the spectrum when $P_{in} = 6P_{cr}$ (solid curve). For comparison, 11(d) shows supercontinuum with (solid) and without (dash-dotted) T, T^{-1} in air for the initial data of Fig. 9.

and self-steepening in the presence (or not) of ionization in fused silica. The properties stressed by Eq. (70) can be refound. Note the asymmetry in the SPM profile when the Fourier transform of the on-axis field intensity is expressed in wavelengths [Fig. 11(a)], since $\Delta\omega = -2\pi c\Delta\lambda/\lambda^2$. For comparison, Fig. 11(d) illustrates supercontinuum reached in air with or without pulse steepening at 800 nm. In all cases, we can observe a clear amplification of UV/blue wavelengths due to steepening terms. Because the spectral component rapidly decreases outside the central wavelength, the principal source of ionization (scaling as I^K in MPI regime), however, remains given by that operating at λ_0 .

F. Modulational instabilities: The route to multiple filamentation

In the context of nonlinear optics, an intense wave propagating in a focusing Kerr medium can break up into several spots from the inhomogeneities affecting its initial distribution. This phenomenon was first evidenced by self-focusing experiments in liquids (Bespalov and Talanov, 1966; Campillo *et al.*, 1973) and the resulting small-scale structures are usually named "filaments". Because it mostly concerns spatial distortions, this process of "multifilamentation" can be understood from Eqs. (51), where temporal variations are discarded. (2 + 1)-dimensional models freezing temporal dependencies were used to simulate the early filamentation stage of high-power beams in various transparent media, yielding rather good qualitative agreements with experimental measurements (Dubietis *et al.*, 2004a,c; Fibich *et al.*, 2005, 2004; Kandidov *et al.*, 2005, 1999; Porrás *et al.*, 2004). In plasma regimes, 2D mod-

els can also simulate complex multifilamentation patterns created from terawatt laser pulses (Bergé *et al.*, 2004; Skupin *et al.*, 2004b). For instance, by assuming that MPI mainly counterbalances Kerr focusing at a dominant time slice $t = t_c(z)$, the field envelope can be decomposed as $\psi = \tilde{\psi}(x, y, z) \times \chi[t, t_c(z)]$ where the temporal distribution for the highest-intensity peak is modeled by the Gaussian $\chi[t, t_c(z)] = e^{-[t-t_c(z)]^2/\tau^2}$ with constant extent τ . Plugging the above expression into Eqs. (51), computing the expression of ρ and averaging the result over the entire time domain supplies the extended NLS equation for the spatial profile ψ :

$$i\partial_z \tilde{\psi} = -\nabla_{\perp}^2 \tilde{\psi} - f(|\tilde{\psi}|^2) \tilde{\psi} \quad (71a)$$

$$f(s) = \alpha s - \frac{\epsilon s^2}{\sqrt{3}} - \sqrt{\frac{\pi}{8K}} \tau \Gamma s^K + i \frac{\nu s^{K-1}}{\sqrt{K}}, \quad (71b)$$

where the coefficient α averages the Raman delayed response. This model does not formally depend on the longitudinal location of the time slice $t = t_c(z)$. The only arbitrariness is the choice of the peak duration τ . Because MPI shortens pulses to mean duration reaching 1/10 of their initial values, the value $\tau = 0.1$ was found to provide the best approximations of fluence patterns developed by (3 + 1)-dimensional fs pulses.

Modeling filament formation then requires a perturbation theory involving a steady-state solution, expressed as $\tilde{\psi}_s(\vec{r}, z) = \phi(\vec{r})e^{i\lambda z}$. Defined in the limit of no dissipation ($\nu \rightarrow 0$), ϕ satisfies the differential equation

$$-\lambda\phi + \vec{\nabla}_{\perp}^2 \phi + f(\phi^2)\phi = 0 \quad (72)$$

and $\lambda = \text{const}$. Stability of ϕ is investigated from perturbations $v + iw$ with small real-valued components (v, w) acting against this stationary mode. Linearizing Eqs. (71) yields the eigenvalue problem (Kuznetsov *et al.*, 1986)

$$\partial_z v = L_0 w, \quad L_0 = \lambda - \vec{\nabla}_{\perp}^2 - f(\phi^2), \quad (73a)$$

$$-\partial_z w = L_1 v, \quad L_1 = \lambda - \vec{\nabla}_{\perp}^2 - [f(\phi^2) + 2f'(\phi^2)\phi^2], \quad (73b)$$

where L_0 and L_1 are self-adjoint operators with $f'(\phi^2) = \partial f(u)/\partial u|_{u=\phi^2}$. Combining Eqs. (73), we then obtain $\partial_z^2 v = -L_0 L_1 v$, from which different kinds of instabilities may be investigated.

Modulational instabilities: Originally proposed by Bespalov and Talanov (Bespalov and Talanov, 1966), the modulational instability (MI) theory involves oscillatory perturbations with an exponential growth rate, that split the beam envelope approximated by a background uniform solution. Perturbative modes are chosen as $v, w \sim \cos(k_x x) \cos(k_y y) e^{\gamma z}$ and they apply to a plane wave ϕ which satisfies $\vec{\nabla}_{\perp}^2 \phi = 0$ and $\lambda = f(\phi^2)$. The growth rate γ is then given by

$$\gamma^2 = k_{\perp}^2 (2A - k_{\perp}^2), \quad A \equiv u f'(u)|_{u=\phi^2}. \quad (74)$$

Plane waves are unstable with $\gamma^2 > 0$ in the range $0 < k_{\perp} < \sqrt{2A}$ and the maximum growth rate $\gamma_{\text{max}} = A$ is attained for $k_{\perp} = k_{\text{max}} = \sqrt{A}$. This instability promotes the beam breakup into arrays of small-scale filaments periodically distributed in the diffraction plane with the transversal spacing $\lambda_{\text{mod}} \simeq 2\pi/k_{\text{max}}$ and longitudinal length $\sim \gamma_{\text{max}}^{-1}$. The number of filaments is close to the ratio $P_{\text{in}}/P_{\text{fil}}$, where P_{fil} is the power enclosed in one filament. Considering each filament with radial symmetry, the evaluation $P_{\text{fil}} \simeq 2\pi \int_0^{\lambda_{\text{mod}}/2} r |\phi|^2 dr \simeq 2.65 P_c$ holds for unsaturated Kerr media [$f(s) = s$].

Because they constitute rough representations of physical beams, plane waves can be replaced by the soliton modes of the NLS equation (72). The resulting instability appears when a soliton ϕ is perturbed by oscillatory modulations developing along one transverse axis. Perturbations are, e.g., local in x and they promote the formation of bunches periodically distributed over the y axis. The operators L_0 and L_1 in Eqs. (73) are transformed as $L_0 = \lambda - \partial_x^2 - f(\phi^2) + k_y^2$ and $L_1 = L_0 - 2f'(\phi^2)\phi^2$. Numerical computations are then often required for solving the spectral problem (73) (Akhmediev *et al.*, 1992; Rypdal and Rasmussen, 1989; Zakharov and Rubenchik, 1974).

Azimuthal instabilities: For broad beams, self-focusing takes place as a regular distribution of dots located upon ring diffraction patterns (Feit and Fleck, 1988). To model this instability, the Laplacian in Eq. (71a) must be rewritten as $\vec{\nabla}_{\perp}^2 = r^{-1} \partial_r r \partial_r + r^{-2} \partial_{\theta}^2$, where θ denotes the azimuthal angle. Within a first approximation, unstable modes $v, w \sim \cos(M\theta) e^{\gamma M z}$ with azimuthal index number M break up a spatial ring, which is modeled by a uniform background solution ϕ lying on a circular path with length $s = \bar{r}\theta$, and mean radius \bar{r} . Eqs. (73) then yield (Atai *et al.*, 1994; Soto-Crespo *et al.*, 1992)

$$\gamma_M^2 = \left(\frac{M}{\bar{r}}\right)^2 \left(2A - \frac{M^2}{\bar{r}^2}\right), \quad (75)$$

and the maximum number of modulations on the ring is provided by the integer part of $M_{\text{max}} = \bar{r}\sqrt{A}$.

In this regards, solitary waveforms having a ring-shaped distribution may also exhibit a phase singularity with an integer number of windings, m (topological charge). Such structures are termed "optical vortices". They convey a constant orbital angular momentum (Kruglov *et al.*, 1992; Kruglov and Vlasov, 1985) and are experimentally designed by means of phase masks and holographic techniques (Desyatnikov *et al.*, 2005; Petrov *et al.*, 1998; Tikhonenko *et al.*, 1996). For cubic media, they undergo azimuthal MI, which make vortex solitons decay into $M_{\text{max}} \sim 2|m| + 1$ filaments (Vinçotte and Bergé, 2005; Vuong *et al.*, 2006). For cubic-quintic nonlinearities, optical vortices may be linearly stable for $|m| = 1$ (Berezhiani *et al.*, 2001; Desyatnikov *et al.*, 2000; Quigora-Teixeiro and Michinel, 1997; Skarka *et al.*, 2003; Towers *et al.*, 2001), but they decay into $M_{\text{max}} \sim 2|m|$ filaments otherwise

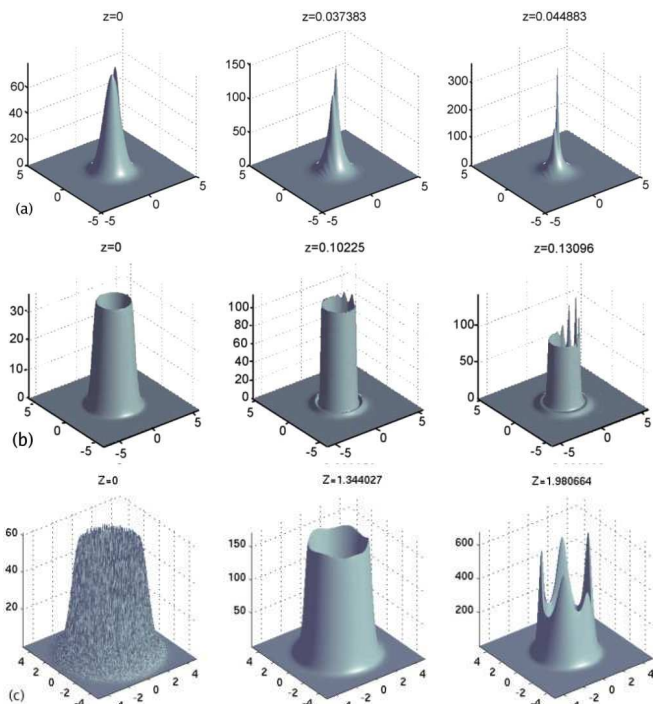


FIG. 12 Multifilamentation patterns in Kerr focusing regime at powers above critical ($P_{\text{in}} \leq 30P_{\text{cr}}$) for (a) a Gaussian beam ($x_0 = 0.35, y_0 = 0, \epsilon = 0.1$) and (b) an annular ring with flat phase ($x_0 = 1.7, y_0 = 0, \epsilon = 0.01$). These two beams undergo MI from a local defect with relative amplitude ϵ located at the coordinates (x_0, y_0) . (c) Vortex-shaped beams with charge $|m| = 2$ initially perturbed by a 10% random noise.

(Firth and Skryabin, 1997; Skryabin and Firth, 1998). The orbital motion confers robustness to vortex solitons, which can propagate powerful beams beyond several tens of Rayleigh distances (Michinel *et al.*, 2001), before they break up into filaments.

Figure 12 shows the multifilamentation of (a) a Gaussian beam, (b) a flat-phase, ring-shaped waveform and (c) an $m = 2$ vortex breaking up into $2|m| + 1$ filaments in a cubic medium. MI is triggered either from an initial defect or from random noise (Bergé *et al.*, 2003). Note the robustness of the Gaussian profile, whose shape definitively differs from that of a plane wave.

Modulational instabilities rather affect the early Kerr stage in the beam propagation. At later stages, the resulting filaments become fully nonlinear and they may interact mutually. From the interplay between diffraction and nonlinearity, two filaments can fuse, whenever their separation distance is below a critical value, function of their individual powers (Bergé *et al.*, 1997; McKinstrie and Russell, 1988). With no saturation, each filament whose power is above critical creates its own attractor, at which it freely collapses. By including saturation, filaments with powers above critical are able to coalesce into an intense central lobe and develop various patterns (Konno and Suzuki, 1979). Without any control, multifilamentation happens as a harmful insta-

bility destroying the homogeneity of the energy distribution. It has detrimental consequences on the quality of the beam shape.

IV. UNIVERSAL FEATURES OF FEMTOSECOND FILAMENTATION

For an efficient propagation, the beam intensity and electron density must both remain below their so-called "laser-induced breakdown" (LIB) limits. LIB means the breakdown of the beam that results in damage or tremendous energy absorption in dielectrics as well as in liquids (Kennedy, 1995). It involves three major processes, namely, (i) ionization, (ii) heating of the "free" electrons by the radiation, and (iii) transfer of plasma energy to the medium. Once generated, the electron plasma absorbs and scatters the remaining pulse energy. Assuming free electrons seeded by avalanche ionization, $\partial_t \rho \simeq (\sigma/U_i)\rho I$, an incident pulse launched in tightly focused geometry will be significantly attenuated by energy absorption at density levels above a critical value, ρ_{cr} . An estimate of the LIB intensity then follows as $I_{\text{LIB}} \sim (U_i/\sigma t_p)\ln(\rho_{\text{cr}})$ (Feng *et al.*, 1995). For subpicosecond pulses, multiphoton processes mostly provide the dominant breakdown mechanism, such that the estimate $I_{\text{LIB}} \sim (\rho_{\text{cr}}/\rho_{\text{nt}}\sigma_K t_p)^{1/K}$ applies (Feng *et al.*, 1997). Ranges of values for ρ_{cr} are often close to 10% of ρ_{nt} (e.g., $\rho_{\text{cr}} = 10^{21} \text{ cm}^{-3}$ in silica or water) when using femtosecond pulses (Lenzner *et al.*, 1998; Noack and Vogel, 1999).

In what follows, characteristics of ultrashort pulse propagation are mostly depicted for peak electron densities less than the LIB threshold. Density levels maintain the pulse in self-channeled state without significant conversion of beam energy into the plasma.

A. Radial self-focusing and temporal splittings

The self-channeling mechanism relies on the balance between Kerr focusing and plasma generation. The most illuminating example is given by "femtosecond filaments" in air, as presented in Fig. 1. Atmospheric filaments form microstructures exhibiting $\sim 100 - 150 \mu\text{m}$ in FWHM diameter and $\sim 1 \text{ mJ}$ in energy at infrared wavelengths (800 nm). They are accompanied by a strong SPM-induced spectral broadening and cover several tens of meters, whenever the input pulse power exceeds $\sim 10 \text{ GW}$ (Braun *et al.*, 1995; Brodeur *et al.*, 1997; Nibbering *et al.*, 1996). Propagation distances in excess of 200 m were even reported for 60 fs, 795 nm pulses with 4 mm diameter, traveling thus upon a few Rayleigh distances z_0 . These experiments revealed, after a possible short stage of multiple filamentation, the emergence of one robust filament coupled to electron densities of a few times 10^{16} cm^{-3} (LaFontaine *et al.*, 1999b). Further measurements of infrared filaments specified a peak intensity of about $5 \times 10^{13} \text{ W/cm}^2$ (Kasparian *et al.*,

2000a). Similar behaviors involving slightly higher peak intensities were also reported in N_2 molecular gases at different pressures (Becker *et al.*, 2001).

The "moving-focus" model was first revisited to yield qualitative explanations of this phenomenon (Brodeur *et al.*, 1997; Chin *et al.*, 1999a). Though pleasant and rather intuitive, this model, however, failed at describing the self-guiding of light that persists beyond the linear focus of convergent beams (Lange *et al.*, 1998b). The appropriate scenario for long distance propagation, called "dynamical spatial replenishment", was specified by numerical simulations. During the focusing stage, the beam generates a narrow plasma that strongly defocuses the trailing part of the pulse and creates one leading peak. Once the intensity decreases enough (via, e.g., MPA), plasma generation turns off. The back pulse can then refocus, which produces a two-spiked temporal profile (Mlejnek *et al.*, 1998a,b). In space, plasma defocuses only the inner part of the beam intensity, so that the trailing edge decays into spatial rings (Kandidov *et al.*, 1994). With increasing propagation distances and as the front pulse intensity decreases, the spatial rings coalesce under Kerr compression and allow refocusing of the trail. Although the beam radius may look "quasi-static", the temporal and spatial distributions of the pulse strongly fluctuate (see, e.g., Figs. 9 and 10). At high enough powers, self-channeling is supported by several focusing/defocusing cycles triggered from a dynamical interplay between multiple, stringent peaks alternating in the temporal pulse profile. "Pushed" by steepening effects, these peaks are responsible for the formation of optical shocks in the medium. This complex dynamics was reported by several authors, dealing with pulse propagation either in air (Aközbek *et al.*, 2001; Bergé and Couairon, 2000; Chiron *et al.*, 1999; Couairon *et al.*, 2002), in argon cells (Champeaux and Bergé, 2003; Nurhuda *et al.*, 2002a), or even in fused silica (Tzortzakis *et al.*, 2001d).

Because the fundamental scenario for self-channeling is that aforementioned, estimates for peak intensities (I_{\max}), electron densities (ρ_{\max}) and filament radius (L_{\min}) can be deduced from equating diffraction, Kerr and ionization responses. This yields the simple relations

$$I_{\max} \simeq \frac{\rho_{\max}}{2\rho_c n_0 \bar{n}_2}, \quad \rho_{\max} \simeq t_p \rho_{\text{nt}} W(I_{\max}), \quad (76a)$$

$$L_{\min} \sim \pi(2k_0^2 \bar{n}_2 I_{\max}/n_0)^{-1/2}, \quad (76b)$$

where

$$\bar{n}_2 = n_2(1 - x_K) + n_2 x_K \max_t G(t), \quad (77)$$

represents the effective Kerr index when the Raman-delayed response is maximum over the initial pulse profile and $W(I_{\max})$ reduces to $W(I_{\max}) = \sigma_K I_{\max}^K$ in MPI regime. Some parameter values for different material used throughout this review have been indicated in Table I. From these values the above relations supply filament diameters of the order of $150\mu\text{m}$ in air at 800 nm and

TABLE I Parameter values for dioxygen molecules (air) at 800 nm ($U_i = 12.1$ eV, $\rho_{\text{nt}} = 5.4 \times 10^{18}$ cm^{-3}), fused silica at $\lambda_0 = 790$ nm and 1550 nm ($U_i = 7.8$ eV, $\rho_{\text{nt}} = 2.1 \times 10^{22}$ cm^{-3}), and water at 527 nm ($U_i = 7$ eV, $\rho_{\text{nt}} = 3.32 \times 10^{22}$ cm^{-3}).

λ_0 [nm]	n_2 [cm^2/W]	k'' [fs/cm^2]	σ_K [$\text{s}^{-1}\text{cm}^{2K}/\text{W}^K$]	K
800/O ₂	4×10^{-19}	0.2	2.9×10^{-99}	8
248/O ₂	8×10^{-19}	1.21	2×10^{-28}	3
790/SiO ₂	3.2×10^{-16}	370	6.8×10^{-56}	5
1550/SiO ₂	2.2×10^{-16}	-280	1.5×10^{-119}	10
527/H ₂ O	2.7×10^{-16}	500	1.07×10^{-28}	3

$10 - 20 \mu\text{m}$ in dense transparent media (dielectrics, water), which agrees with current numerical data. Note that for laser wavelengths about $1\mu\text{m}$, the requirement (9) is always fulfilled. As inferred from Table I, the critical power for self-focusing exceeds the GW level in gases, but remains limited to a few MW in dense materials.

Plasma generation is mostly expected to stop the divergence of the beam caused by self-focusing, except for specific values of the parameters $P_{\text{in}}/P_{\text{cr}}$ and $\delta \sim k''$ that privilege collapse arrest by dispersion (see Fig. 8). For $\lambda_0 = 800$ nm, nonlinear fluorescence techniques (Liu *et al.*, 2005b) recently revealed that small-scale filaments created in water at powers lower than $8P_{\text{cr}}$ did not need plasma saturation. With 38-fs, $110\text{-}\mu\text{m}$ pulses and $k'' \simeq 560$ fs^2/cm , the normalized dispersion length is $\delta \sim 4.9$, for which the plasma response may indeed be inhibited, following Fig. 8. Pulses are then subject to space-frequency coupling from the interplay among SPM, dispersion and phase mismatching, that produces conical emission (see below). The energy loss caused by the conical wave depends on the energy contained in the colored part of the spectrum. Liu *et al.* (Liu *et al.*, 2005b) suggests that if the phase matching width of light waves whose frequencies experience self-focusing is small enough compared with the spectral width of the on-axis laser pulse, the spectral energy going into the self-focusing components is small and the energy loss caused by conical emission becomes large. This phase matching width is all the smaller as GVD is large and the spread of energy can stop the Kerr focusing without the help of plasma defocusing at powers moderately above critical.

Nonetheless, there exist different scenarios having attracted attention in the past few years. For instance, research groups led by P. Di Trapani and A. Dubietis (Dubietis *et al.*, 2004a, 2003; Porras *et al.*, 2004) emphasized the apparent absence of free electron emission in the self-guiding of 527 nm, 200 fs pulses with $\sim 100 \mu\text{m}$ waist and powers up to $10 P_{\text{cr}}$, propagating in water in loosely focused geometry. Numerical simulations outlined the filament reshaping into a nonlinear X (bi-conical) wave, driven by the combination between linear diffraction, normal GVD, self-focusing and nonlinear losses (Kolesik *et al.*, 2002). Whereas GVD cannot halt the beam collapse even in these configurations (δ

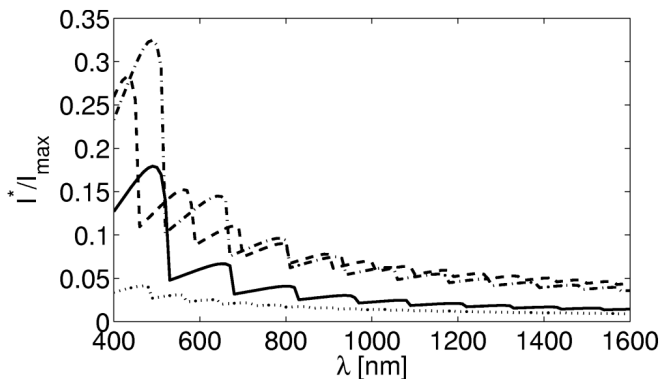


FIG. 13 I^*/I_{\max} versus λ_0 for different pulse durations t_p in air (70 fs, dotted curve), in fused silica (20 fs, dashed curve), and in water (170 fs, solid curve; 50 fs, dash-dotted curve).

is too small), normal dispersion plays an important role by dispersing the most intense time slices of the pulse. Instead of an extensive production of free electrons, the nonlinear losses (MPA) inherent to this process moreover dominate at laser wavelengths as low as 527 nm. From Eqs. (76a), it is always possible to compute numerically the ratio I^*/I_{\max} that dictates the MPA efficiency [$\sim U_i \rho_{\text{nt}} W(I)/I$] compared with plasma defocusing [$\sim ik_0 \rho / \rho_c$] in Eq. (43). This ratio involves the quantity

$$I^* = n_0^2 \rho_c U_i / (k_0 t_p), \quad (78)$$

that scales like $n_0 / (\lambda_0 t_p)$. The resulting curve is displayed in Fig. 13 for fused silica, water and air at different pulse durations. Keldysh ionization rate for crystals is used for dense media, while the PPT rate is employed for air (O_2 molecules). This figure shows that the percentage of MPA over the emission of free electrons augments all the more as the laser wavelength is low and the pulse duration is short. In air, MPA becomes negligible compared with MPI. For dense materials, Fig. 13 points out to a sudden change in the influence of MPA whenever $\lambda_0 < 600$ nm. This mainly follows from the dependences over λ_0 of both the critical plasma density (37) and the photo-ionization rate $W(I)$. As a result, self-focusing is stopped at lower intensities and the free electron density is maintained at lower levels (Skupin *et al.*, 2006a).

B. Robustness and multifilamentation

Femtosecond filaments are remarkably robust, in the sense that they can propagate over several meters and even reform after hitting an obstacle. In the atmosphere, aerosol particles, like water droplets or dust, may have dimensions comparable with the filament diameter, which could seriously harm the dynamical balance required to propagate filaments. However, even opaque droplets as large as $100 \mu\text{m}$ in diameter do not block filamentation. More intriguing, energy losses are limited to 15% of the

filament energy (Courvoisier *et al.*, 2003). The filament rapidly self-heals and seems unaffected by the droplet, so that an energy balance between the filament core and the unfocused part of the beam was conjectured to explain the rebuilding of the pulse. Unfocused parts of the beam refer to the "photon bath", i.e., the low-amplitude background surrounding the filament core.

Numerical simulations constrained to the radial symmetry reproduced the smallness of the immediate energy losses in air and the interaction dynamics was similar whatever the pulse self-channels in the first (leading edge) or in the second (trailing edge) focusing stage (Kolesik and Moloney, 2004b). From water experiments (Dubietis *et al.*, 2004b), analogous conclusions were drawn, which insisted more on the linear contribution from the outer conical waves to the filament reconstruction. The "active zone" of the photon bath must, however, keep time slices with power above critical to re-localize the beam at center. The filament must also be somehow delocalized in space, in order to justify the smallness of energy losses during the collision. Answering this point, simulations revealed that the breakup of rotational symmetry of pulsed beams can push the focusing components, still untouched by the plasma, out of axis. The defocused time slices diffract to the low-intensity background, but the focusing ones exit out of center (Skupin *et al.*, 2003, 2002). A femtosecond filament thus consists of a "spatially-extended" structure, whose most intense components can move within a zone of several hundreds of μm around the origin. Through a collision, just a few components are involved, which explains the smallness of the losses. Three-dimensional simulations enclosing the filament inside a circular disk of $300 \mu\text{m}$ in diameter clearly showed that over the 2 cm of self-healing the beam components outside this zone play no significant role in the filament reconstruction (Skupin *et al.*, 2004a). Some of these results are summarized in Fig. 14. Recent experiments using pinholes to block the photon bath confirmed these theoretical predictions. The energy reservoir actively feeding the filament core was measured within a diameter of $220 - 440 \mu\text{m}$ and was found to contain up to 50% of the pulse energy (Liu *et al.*, 2005c).

Whereas a single filament appears as a robust object, broad pulses having many critical powers become subject to modulational instability. The background energy reservoir favors energy exchanges between the different optical cells, that focus under Kerr compression and defocus by plasma generation. A sea of collapsing spots is thus nucleated, forming an "optically turbulent femtosecond light guide" along which nonlinear dissipation consumes small energy per filament (Mlejnek *et al.*, 1999). Inside the bundle, the filaments are able to merge and relaunch recurrent collapse events at further distances. They gather into long-range clusters composed of secondary cells that occur around the primary filaments created from the initial beam defects (Bergé *et al.*, 2004; Skupin *et al.*, 2004b). For broad pulses ($w_0 > 1$ cm) en-

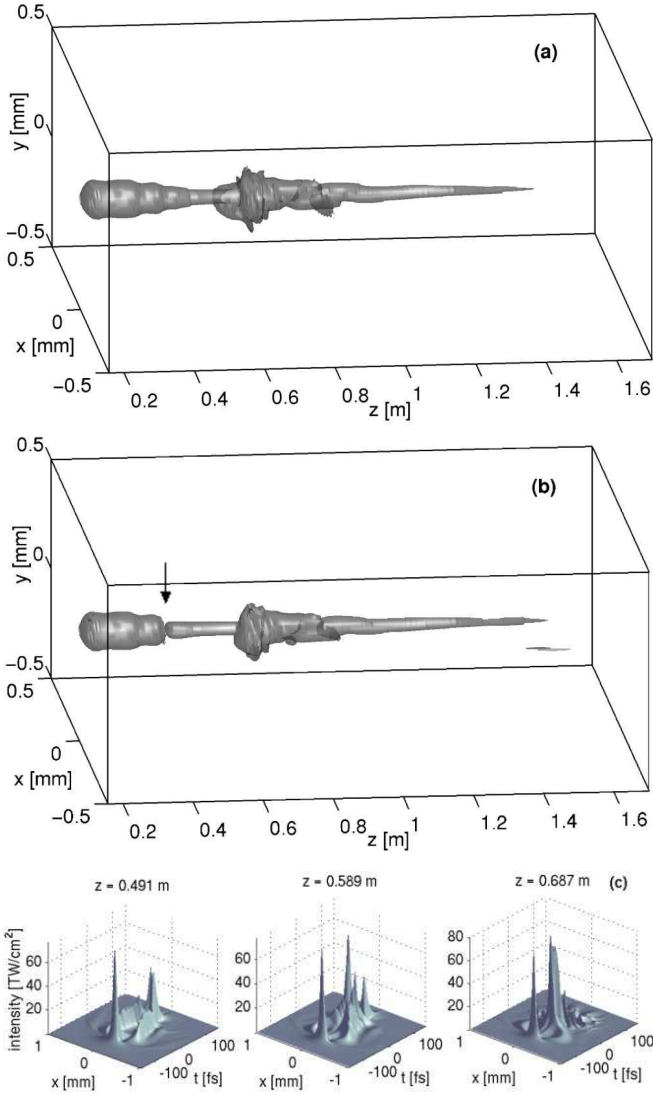


FIG. 14 (a,b) 3D surface plots of plasma strings in cases of (a) free propagation or (b) an impact with a $95 \mu\text{m}$ large droplet located at $z = 0.4 \text{ m}$ (see arrow), computed from $(3 + 1)$ -dimensional numerical simulations. Note the convected components at $z \sim 0.65 \text{ m}$, corresponding to the second focusing sequence when the trail peak takes over the front pulse and develops azimuthal instabilities in space. (c) Temporal profiles occupying an active zone of $\sim 300 \mu\text{m}$ in diameter.

closing enough power (e.g., more than $100 P_{\text{cr}}$), the self-focusing distance is close to the MI filamentation distance $z_{\text{fil}} \sim 1/n_2 I_0$, which varies like $1/P_{\text{in}}$ whenever $I_0 \ll I_{\text{max}}$ (Campillo *et al.*, 1974; Fibich *et al.*, 2005).

For narrower beams, experiments exploring mJ, mm-waisted pulses (Hosseini *et al.*, 2004a; Liu *et al.*, 2004; Tzortzakis *et al.*, 2001a) reported the beam breakup into two filaments that continue to increase in intensity by Kerr focusing. Depending on their separation distance and individual powers, these filaments can merge. An example of this fusion mechanism is shown in Fig 15 for two (plasma-free) optical spots, resulting from the mod-

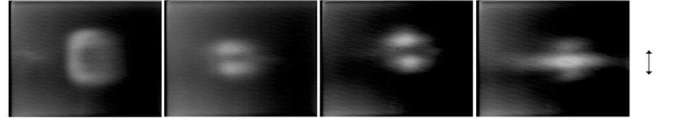


FIG. 15 Merging of two filaments created from mm-waisted, fs pulses with 5 mJ energy. Arrow indicates a scale length of 2 mm.

ulational instability of a 42-fs, 3 mm-waisted collimated pulse in air (Tzortzakis *et al.*, 2001a). In the presence of plasma defocusing, "parent" filaments develop spatial rings whose radius increases with z . Two systems of rings can thus interfere to yield "child" filaments. Each focusing spot triggers a plasma sequence that defocuses the trail pulse and locates the cells at specific negative instants. The number of "filaments" is therefore higher in intensity than in the beam fluence, which sums up all the time slices (Champeaux and Bergé, 2005).

Since multifilamentation emerges from the initial beam defects, several techniques to control this process in shot-to-shot, meter-range experiments have been proposed. Among those, we can mention the introduction of beam ellipticity (Dubietis *et al.*, 2004c; Grow and Gaeta, 2005) or of a tilted lens (Fibich *et al.*, 2004) along the optical path. Strong field gradients or forcing aberrations through phase masks can also be used to control high intensities over long scales (Méchain *et al.*, 2004). Other techniques consist in monitoring the filamentation distance by changing the beam divergence angle with a deformable mirror (Jin *et al.*, 2005). By this method, a single filament has been produced with powers as high as 420 GW, usually yielding multiple filaments in collimated geometry. Alternative methods consist in tuning the focal distance of a telescope setup composed of divergent and convergent lenses (Fibich *et al.*, 2006; Liu *et al.*, 2006). Interesting features have recently been published concerning the fusion, repulsion and spiral co-propagation of two filaments, depending on their relative phase shift and crossing angle, which may further be used to optimize the propagation range (Xi *et al.*, 2006). In the same spirit, arrays of diffractive microlenses (Cook *et al.*, 2005) or periodic meshes (Kandidov *et al.*, 2005) into the propagation path helps in making the multifilamentation "more deterministic". As a matter of fact, these methods amount to altering the background surface of the beam from which small-scale filaments can randomly emerge from modulational instability. Alternative ways may be provided by femtosecond optical vortices (Vinçotte and Bergé, 2005) that keep the filaments rotating along a ring and are nowadays designed experimentally on fs time scales (Mariyenko *et al.*, 2005; Vuong *et al.*, 2006). Further explorations should concern optical smoothing techniques breaking the laser spatial or temporal coherence (Marklund and Shukla, 2006). These techniques are currently employed in laser facilities devoted to the inertial confinement fusion, in order to homogenize the beam distribution (Donnat *et al.*, 1992;

Labaune *et al.*, 1992).

C. White light generation and Conical emission

Spectral broadening has been the topic of intense investigations for several decades (Alfano and Shapiro, 1970). In 1995, Gil'denburg *et al.* (Gil'denburg *et al.*, 1995) performed 2D numerical simulations of ultrashort focused electromagnetic waves creating breakdown plasma due to tunnel gas ionization. High blueshifts of the pulse spectrum up to $\Delta\omega/\omega_0 \equiv \omega/\omega_0 - 1 > 40\%$ were reported. At that time, blueshift was attributed to plasma generation, as the growth of free electrons increases the plasma frequency by $\omega_{pe}^2 = q_e^2 \rho(I)/m_e \epsilon_0$ and implies a positive frequency shift $\Delta\omega_+ \sim \int_0^z \partial_t \rho dl$ (Penetrante *et al.*, 1992; Rae and Burnett, 1992; Yablonovitch, 1974). Later, experimental spectra revealed an "ultrafast white-light continuum". This occurs in a wide variety of condensed and gaseous media, whenever the input beam power exceeds the self-focusing threshold, which fixes a striking "band gap" for supercontinuum generation (Brodeur and Chin, 1998, 1999). Around the central wavelength of 800 nm, blueshifts ($\Delta\omega_+$) down to 0.5 μm in wavelength enlarged the spectra at intensities lower than 10^{-2} times the central one. Spectral enlargements appeared asymmetric, with a limited redshift, which could not be explained by SPM theory alone. Continua emitted from gases were found narrower ($\Delta\omega_+ \simeq 0.5\omega_0$) than those for dense media ($\Delta\omega_+ \simeq 0.8 - 1.6\omega_0$).

Because this process mixes all spectral components in the visible range, the core of the filament evolves like a white spot, which gives rise to a "white-light laser" (Chin *et al.*, 1999b). Noting by $\varphi(\vec{r}, t)$ the phase of the field envelope, frequency variations are dictated by

$$\Delta\omega = -\partial_t \varphi \sim -k_0 \Delta z \partial_t (\bar{n}_2 I - \rho/2n_0 \rho_c), \quad (79)$$

which varies with the superimposed actions of the Kerr and plasma responses. Near the focus point, only the front leading edge survives from this interplay and a redshift is enhanced by plasma generation. At later distances, second focusing/defocusing sequences relax the spectra to the blue side while the redshifted components decrease in intensity. A salient blueshift around the central frequency follows from self-steepening that creates a shock edge at the back of the pulse and amplifies a "blue shoulder" in the spectrum (Aközbek *et al.*, 2001). This spectral dynamics readily follows from Eq. (70). Asymmetries caused by the focusing events are important: They design the pulse spectrum which will be preserved after the nonlinear stage of the beam.

The pulse spectrum is usually computed from the Fourier transform of the field intensity, either at $r = 0$, or being averaged over the filament radius, $S_{\text{fil}}(\omega) = 2\pi \int_0^{r_{\text{fil}}} |\hat{\mathcal{E}}(r, \omega)|^2 r dr$. More insights can be obtained by looking at the frequency-angular spectral function

$S(\theta_x, \theta_y, \omega, z) = |Q(\theta_x, \theta_y, \omega, z)|^2$, defining

$$Q(\theta_x, \theta_y, \omega, z) = \int dx dy dt U(x, y, z, t) e^{i\omega t - i\theta_x k_x - i\theta_y k_y}, \quad (80)$$

where $\theta_x = k_x/k$, $\theta_y = k_y/k$ are the angles at which different frequency components ω propagate in the medium. The dependence of the angle $\theta = \theta_x = \theta_y$ on wavelength defines the supercontinuum cone emission and is obtained by means of the expression $\lambda = 2\pi c/\omega$. Surface plots of $\ln S(\lambda, \theta)$ compared with the spatio-temporal intensity distributions figure out a conical emission (CE) driven by "wings" directed to non-zero angles and connected with the plasma-induced spatial rings (Kandidov *et al.*, 2004, 2003). Nibbering, Kosareva *et al.* (Kosareva *et al.*, 1997; Nibbering *et al.*, 1996) first revealed the existence of this conical emission accompanying femtosecond filamentation in air at 800 nm. Recalled in Fig. 16(a), CE increases in the interval $0 \leq \theta \leq 0.12^\circ$ with decreasing wavelengths $800 \geq \lambda \geq 500$ nm and is independent of the position along the filament. This "conical emission" corresponds to the angular divergence of spectral components. The (half-) angle θ at which the radiation propagates is determined by the spatial gradient

$$\theta(\vec{r}, t) = \arctan[-k_0^{-1} \frac{\partial}{\partial r} \varphi(\vec{r}, t)]. \quad (81)$$

This angle depends on the spatial intensity distribution of the pulse, which strongly evolves in self-channeling regime, as illustrated in Figs. 16(b,c,d,e). By comparing the radial dependences of the divergence angle $\theta(r)$, low-frequency components are located nearest the optical axis. High-frequency components lie near the periphery rings and their radiation is directed out of the axis.

Besides Kerr and plasma effects, the material dispersion can play a relevant role in condensed media, for which the GVD coefficient is usually high. Kolesik *et al.* (Kolesik *et al.*, 2003a,b) compared the extension of supercontinuum wings generated in air ($k'' = 0.2 \text{ fs}^2/\text{cm}$ at 800 nm) and in water ($k'' = 500 \text{ fs}^2/\text{cm}$ at 400 nm). Numerical simulations accounting for the complete linear dispersion relation displayed evidence of that chromatic dispersion becomes a key player (for water above all) in determining the spectral extent of supercontinuum generation: Full chromatic dispersion included in $k(\omega)$ encompasses the T, T^{-1} operators when passing to an envelope description (see Sec. II). These operators induce steepening of the pulse profile and strongly "blueshift" the spectra.

On the other hand, spectral broadening becomes enhanced by harmonic generation. The question of coupling ultrafast IR components with self-induced third-harmonics was raised ten years ago (Backus *et al.*, 1996). While conversion efficiency as high as 0.1% was first reported for third-harmonic (TH) generation in air, higher efficiencies up to 0.2% were next achieved by using focused pulses filamenting over only ~ 10 cm. At 800 nm, the coupling of TH with the IR pump produces

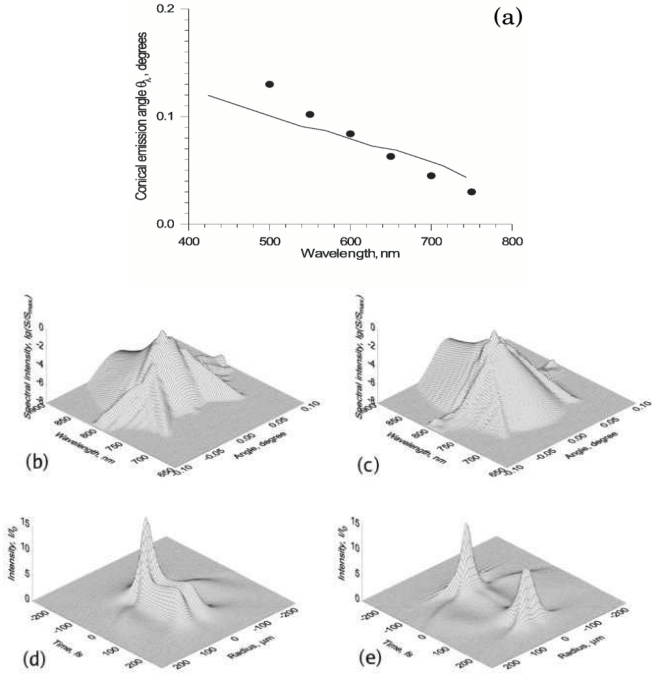


FIG. 16 (a) Measured (symbols) and calculated (curve) CE angles in air. (b,c) Frequency angular spectra and (d,e) spatio-temporal distributions of an atmospheric, fs filament starting from infrared pulses with 6.3 critical powers, 250 fs FWHM duration and 0.18-mm radius at two different propagation distances (b,d) $z = 0.43z_0$; (c,e) $z = 0.6z_0$ (Kandidov *et al.*, 2003). Courtesy of O. Kosareva.

a "two-colored" femtosecond filament from the threshold intensity $I(\omega) \geq 2 \times 10^{13} \text{ W/cm}^2$ (Aközbek *et al.*, 2002; Alexeev *et al.*, 2005; Yang *et al.*, 2003). Along this process, the pump wave injects part of its energy into the third harmonics. The amount of pump energy depends on the linear wave vector mismatch parameter $\Delta k = [3k(\omega) - k(3\omega)]^{-1}$ fixing the coherence length $L_c = \pi/|\Delta k|$. The smaller the coherence length, the weaker TH fields, since most of the pump energy is periodically injected and depleted by the pump. In self-channeling regime, the balance between TH, pump wave nonlinearities and the linear mismatch parameter makes the phase difference $\Delta\varphi = 3\varphi(\omega) - \varphi(3\omega)$ be clamped at a constant value equal to π (Aközbek *et al.*, 2002). Along meter-range distances, the two-colored filament propagates over longer scales than an IR pulse alone, as the TH component stabilizes the pump wave and achieves 0.5% conversion efficiency (Bergé *et al.*, 2005). Experimental identification of the TH component reveals some central spot surrounded by ring structures embarking most of the TH energy and having a half-divergence angle of 0.5 mrad (Théberge *et al.*, 2005a). This contributes to enhance the total conical emission of the beam.

Harmonic generation permits the occurrence of amazing phenomena, such as, e.g., the emergence of new wavelengths with non-trivial relative spectral intensities. Manipulating intense, powerful filaments centered at 800

nm results in supercontinuum generation extending down to 230 nm in air and yielding a continuous spectral band of UV-visible wavelengths (Théberge *et al.*, 2005b). This phenomenon was observed over laboratory scales as well as over LIDAR propagation distances > 200 m (Bergé *et al.*, 2005; Méjean *et al.*, 2006b). Numerical simulations evidenced that UV-visible spectral broadening is created by the overlap of redshift from the TH component and blueshift from the IR pump, $\Delta\omega_j = -\partial_t\varphi_j$ ($j = \omega, 3\omega$), fulfilling the phase-locking constraint $\Delta\varphi = \pi$ mentioned above. Also, TH-induced saturation reinforces the defocusing action of the electron plasma and enlarges the conical emission to $\sim 0.25^\circ$ at $0.26 \mu\text{m}$. UV-visible supercontinuum generation in air is plotted in Figs. 17(a,b) for a meter-range propagation of one filament. Numerical results reproduce the experimental data in the wavelength domain $200 \leq \lambda \leq 500$ nm at the same distances after the nonlinear focus ($\Delta z = z - z_c$). Fig. 17(c) illustrates the maximum TH and pump intensities, calculated from a propagation model accounting for TH generation [see Eqs. (67)] without steepening terms. Resembling spectral dynamics have also been reported from 45-fs, 1-mJ infrared pulses propagating in argon at atmospheric pressure, after subsequent compression by chirped mirrors (Trushin *et al.*, 2005). Simulations of these experiments (Aközbek *et al.*, 2006) were performed from the one-component NEE model (45) in the limit of weak THG. It was found that temporal gradients inherent to the T, T^{-1} operators are sufficient to amplify UV shifts and cover the THG bandwidth for very short pulses (≤ 10 fs) over short conversion lengths that involve a limited number of focusing/defocusing cycles. Huge UV shifts have already been displayed for air propagation in Fig. 11(d). The issue of knowing under which conditions steepening effects or THG prevail in the supercontinuum generation remains open.

D. Role of the laser wavelength

Whereas emphasis was put so far onto optical pulses delivered by Ti:Sa oscillators operating around 800 nm, one could wonder whether the propagation dynamics changes at different laser wavelengths. Besides the Rayleigh length z_0 , several physical parameters become modified when varying λ_0 , namely,

- The Kerr index n_2 , function of the cubic susceptibility $\chi_{\omega_0}^{(3)}$, decreases inversely proportional to λ_0 (Agrawal, 2001; Nibbering *et al.*, 1997).
- The photo-ionization rate and the number of photons consumed by MPI transitions $\sim U_i/\hbar\omega_0$ vary with λ_0 . Even though MPI gain and MPA losses cannot be separated from each other, their respective influence changes with λ_0 and stresses more losses at low wavelengths (see Fig. 13).
- The value and sign of the GVD parameter, $k'' =$

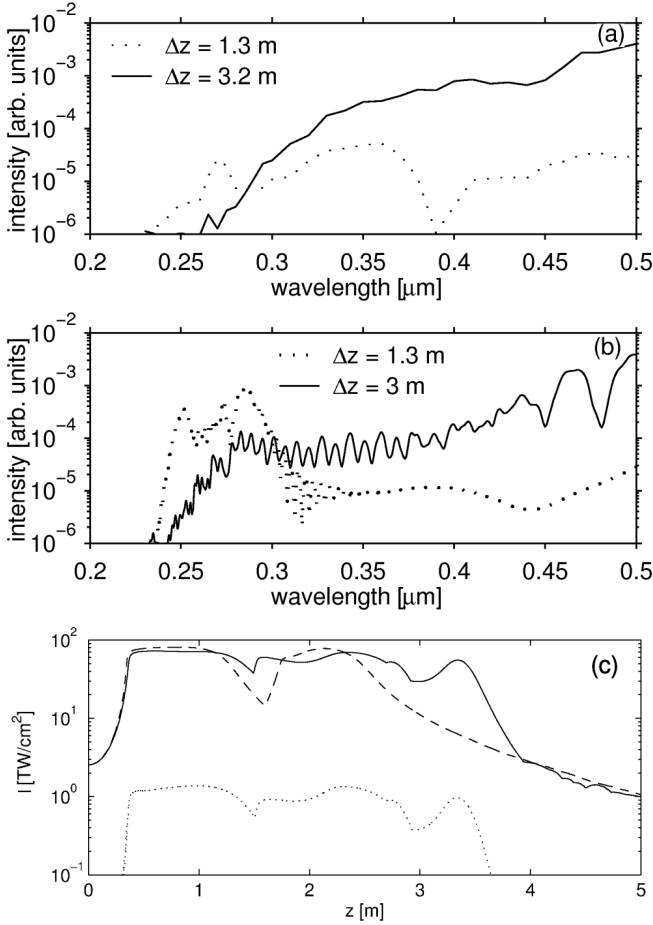


FIG. 17 UV-visible supercontinua (a) measured in laboratory, (b) computed numerically. (c) TH (dotted curve) and pump (solid curve) intensities integrated numerically. The dashed curve represents the same quantity computed using the pump component alone.

$\partial^2 k / \partial \omega^2|_{\omega=\omega_0}$, are modified by varying λ_0 . Depending on the material considered, k'' can turn from positive (normal GVD) to negative (anomalous GVD), which deeply modifies the spatio-temporal structure of the beam.

On this topic, propagation studies mostly concerned the differences between infrared pulses at 800 nm in the atmosphere and ultraviolet ones at, e.g., 248 nm, created by an hybrid, frequency-tripled Ti:Sa/KrF excimer chain. Long distance propagation experiments employing ps, 248-nm pulses (Schwarz *et al.*, 2001, 2000) reported that after a transient stage of multiple filamentation, the beam relaxed to a single filament upon propagation ranges of more than 10 m. The filament length, defined as the spatial region where the plasma couples with the light channel, only covered ~ 1 m, where the electron density, evaluated from the energy consumption per filament, attained $3 \times 10^{15} \text{ cm}^{-3}$. Computed from the MPI rate, the peak intensity was deduced to be about 10^{12} W/cm^2 . Also associated with this fila-

ment, a narrow spectral bandwidth of $\Delta\lambda \sim 10 \text{ nm}$ was measured around 248 nm. Later, Mysyrowicz's group (Tzortzakis *et al.*, 2000a, 2001b) observed the filamentation of UV pulses with durations from 5 ps down to 450 fs. Long, meter-range ($\sim 2 - 4 \text{ m}$) filaments coupled with $10^{15} - 10^{16} \text{ cm}^{-3}$ peak electron densities at intensities of $\sim 10^{11} \text{ W/cm}^2$ were identified. The "apparent" differences between UV and IR peak values follow from the pulse duration between UV and IR experiments, the plasma critical density $\rho_c \sim 1/\lambda_0^2$ together with the number of photons involved in multiphoton transitions. This varies from $K = 8$ at 800 nm to $K = 3$ at 248 nm for O_2 molecules. Numerical simulations, however, showed that, for 50-fs FWHM input pulses, the filament dynamics and length ($< 5 \text{ m}$), starting from the same nonlinear focus, were identical in both cases with peak intensities and electron densities attaining $4 - 8 \times 10^{13} \text{ W/cm}^2$ and 10^{17} cm^{-3} , respectively. Even though the ionization parameters vary with λ_0 , the peak values are fixed by the balance $\rho_{\text{max}}/2\rho_c \sim n_2 I_{\text{max}}$, which remains similar at the two wavelengths. Averaging the peak quantities over a given filament width can justify the different measurements made in this field (Couairon and Bergé, 2002).

Besides, changes in supercontinuum generation were numerically addressed by Aközbek *et al.* (Aközbek *et al.*, 2003), who accounted for THG at other laser wavelengths such as 1064 nm and 1550 nm. The latter corresponds to eye-safety and is particularly important for LIDAR applications. For these wavelengths, the GVD parameters for both pump and TH frequencies are close to each other. However, the wavevector mismatch strongly decreases from -5 cm^{-1} (800 nm) to -0.65 cm^{-1} (1550 nm), whereas the temporal walk-off parameter $\Delta v = [v_g^{-1}(3\omega) - v_g^{-1}(\omega)]^{-1}$ increases from 0.4 to 2.0 cm/s, respectively. Consequently, the coherence length significantly augments at large wavelengths, which allows higher TH intensities and energy conversion efficiency.

More surprising features occur when the laser wavelength is selected in such a way that k'' becomes negative and leads to anomalous dispersion. In that case, the pulse ceases to be dispersed in time and undergoes a temporal compression, in addition to the spatial Kerr focusing. This happens, e.g., in fused silica at $\lambda_0 = 1550 \text{ nm}$, for which $k'' \simeq -280 \text{ fs}^2/\text{cm}$ (see Table I). Recent experiments at this wavelength have shown that collapse events looked "extended" along the z axis, unlike the localized events promoted by normal GVD. Plasma halts the collapse at powers above critical, but anomalous GVD continues to transfer energy into the collapse region, resulting in the formation of longer filaments before the beam eventually defocuses (Moll and Gaeta, 2004). The pulse can thus remain confined along several diffraction lengths and develops very narrow, isolated temporal peaks. A strong temporal compression produces optical spots whose duration is shrunk to the few-cycle limit (Bergé and Skupin, 2005). Sharp shock profiles emerge from this 3D collapsing dynamics and pulse steepening along each focusing/defocusing event tremendously am-

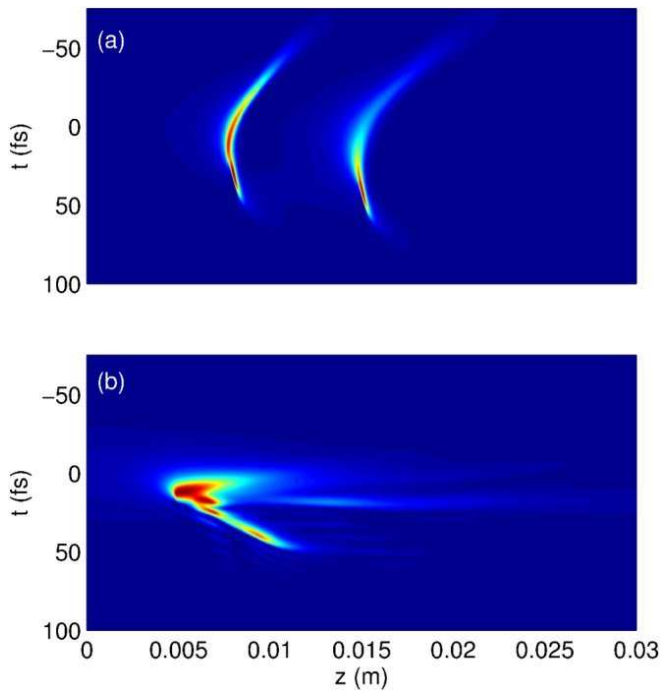


FIG. 18 Temporal dynamics of 42.5-fs pulses with waist $w_0 = 71 \mu\text{m}$ propagating in silica at the laser wavelength (a) $\lambda_0 = 790$ nm with power $P_{\text{in}} = 6P_{\text{cr}}$, (b) $\lambda_0 = 1550$ nm with $P_{\text{in}} = 3P_{\text{cr}}$. Note that the physical value of P_{cr} changes with λ_0 .

plifies the blue part of the spectrum. Fig. 18 displays the temporal distributions of a femtosecond filament created in fused silica at 790 nm ($k'' = 370 \text{ fs}^2/\text{cm} > 0$) and at 1550 nm ($k'' < 0$). At 790 nm, normal GVD stretches the pulse along the time direction. Reversely, at 1550 nm, anomalous GVD compresses it temporally and makes it shift to positive instants through third-order dispersion and self-steepening that push the pulse centroid towards the region $t > 0$.

V. ULTRASHORT FILAMENTS IN GASES

This section is devoted to novel trends opened by the self-guiding of femtosecond pulses over small distances (< 1 m), such as pulse shortening and high-harmonic generation. Most of these applications are conducted in pressurized gas cells, in which the raise of plasma excitations can be controlled by changing the medium pressure.

A. Novel perspectives for pulse shortening

In the last decade, an important challenge has consisted in testing powerful techniques of spectral broadening and ultrabroadband dispersion control, in order to compress pulses to durations of a few optical cycles only ($\tau_{\text{o.c.}} = \lambda_0/c$). Nisoli and co-workers (Nisoli *et al.*, 1997a,b, 1998) achieved the shortest pulse durations from ~ 1 mJ, 20-fs pulses by manipulating the spectral broad-

ening attained along a 60-cm long fused-silica hollow fiber filled with atomic (Ar, Kr) or molecular (N_2) gases. Conditions for optimum pulse compression outlined an appropriate combination of SPM and gas dispersion managed by external chirped compensation systems. Pulses as short as 4.5 fs with output energies up to $70 \mu\text{J}$ could be delivered at 800 nm and 1-kHz repetition rate after using a chirped-mirror delay line. The potential scalability of this system to higher pulse energies was claimed to hold provided that two conditions are fulfilled: (i) The laser peak power must be smaller than P_{cr} ; (ii) The peak intensity must not exceed the ionization threshold, to preserve a flat spectral phase for an efficient recompression. These two requirements could at that time be satisfied by a delicate tuning of the pressure parameter. For a gaseous medium with pressure p , the coefficients affecting Eq. (45a) indeed vary as follows

$$k'' \sim p, \quad \beta^{(K)} \sim p, \quad P_{\text{cr}} \sim 1/n_2 \sim 1/p, \quad \rho_{\text{nt}} \sim p. \quad (82)$$

An optimal compression length can be estimated by $L_{\text{opt}} \approx (6L_{\text{NL}}L_{\text{disp}})^{1/2}$ where $L_{\text{disp}} \sim t_p^2/k''$ and $L_{\text{NL}} \simeq n_2\omega_0 P_{\text{in}}/cS_{\text{eff}}$ are the dispersion and nonlinearity lengths, respectively, with S_{eff} being the effective area of the beam mode (Nisoli *et al.*, 1997a). This distance is tuned by the cell length and the local pressure p , in order to reach the smallest possible pulse duration. Stability of the beam was insured by selecting the EH_{11} hybrid mode with intensity $I(r) = I_0 J_0^2(2.405r/a)$, where I_0 is the peak intensity, J_0 is the zero-order Bessel function and a is the capillary radius (Tempea and Brabec, 1998b). Keeping the beam stable inside the waveguide requires to limit the excitation of higher-order modes owing to the nonlinear spatio-temporal dynamics. The spectral broadening thus inherently depends on how close the initial peak power of the beam is to P_{cr} (Homoelle and Gaeta, 2000). Sub-10 fs pulses are routinely produced through these techniques (Steinmeyer *et al.*, 1999). They can even be applied to bulk (BK7 glass) media, from which pulse shortening by a factor 3-5 and output energies of $220 \mu\text{J}$ have been achieved (Mével *et al.*, 2003).

In this scope, plasma generation may not constitute a drawback for pulse compression. Tempea and Brabec (Tempea and Brabec, 1998a) mentioned the possibility to produce few-cycle optical pulses by compensating the spectral chirp generated by the plasma nonlinearity with a dispersive line delay for intense pulses propagating in filled-gas hollow fibers. This scenario was experimentally confirmed by a JILA team (Wagner *et al.*, 2004), who succeeded in compressing 30 fs pulses to 13 fs in hollow argon capillaries, even without any need of external dispersion compensation. It was recently improved to deliver 5 fs, high energy (1 mJ) pulses following the same scheme supplemented by amplifier systems and chirped-mirror compressors (Verhoef *et al.*, 2006). In Sec. IV, Fig. 9(d) recalled the basic property of pulse compression through the combined effects of Kerr nonlinearity and self-induced ionization. Chromatic dispersion and nonlinear losses, however, saturate the defocusing ac-

tion of free electrons on the leading edge and enable the rear pulse to refocus at later distances. This produces a two-peaked temporal distribution whose time extent is often of the order of the input pulse duration. Achieving an efficient pulse compression, instead, requires to isolate one (at least dominant) peak shrunk in time (Champeaux and Bergé, 2003).

To realize this challenge, Hauri *et al.* used a configuration of two cascaded gas-filled cells with intermittent dispersion compensation for producing sub-mJ light pulses with durations down to 5.7 fs at ~ 800 nm (Hauri *et al.*, 2004). The cells were operated at different pressures. It was later suggested that this scheme could be improved when a single cell with a pressure gradient is used instead, in order to monitor the refocusing stage of the trail and create waveforms with a single-cycle temporal signature (Couairon *et al.*, 2006, 2005). Despite first results mainly directed to higher pulse energies (Suda *et al.*, 2005), further efforts are needed to adjust the pressure gradient for optimum compression to extremely short pulse duration. Alternatively, Stibenz *et al.* recently demonstrated an efficient pure self-compression obliterating the need for any kind of dispersion compensation, pressure gradients, or capillaries for beam guiding (Stibenz *et al.*, 2006). The experimental setup involves beams in convergent geometry with energy up to 5 mJ, $w_0 = 11$ mm, $f = 1.5$ m, FWHM durations of 45 fs and input powers equal to 5 times critical. The beam is initially focused and propagates inside an 1-m long, 50 k-Pa argon cell whose center is positioned at the location of the geometrical focus. Output pulses reach durations down to about 10 fs and develop a strong blue-shift, as reported in Figs. 19(a,b). Figure 19(c) details this self-compression mechanism, reproduced numerically from Eqs. (45). First, near $z_c \simeq 1.45$ m, the front pulse focuses and plasma depletes its rear part. Second, at the linear focus ($z \simeq 1.5$ m), the plasma density decreases, and the back pulse rises again. Finally, from $z \simeq 1.6$ m, only the components close to center, keeping intensity levels above 10^{13} W/cm², are effectively trapped in the filament, whereas the temporal wings diffract rapidly. A robust, temporally-compressed structure of 11 fs forms in the core region of the filament [Fig. 19(d)]. The pulse center relaxes to a narrow "waveguide", preserving its energy at low plasma density levels ($< 10^{14}$ cm⁻³) after the linear focus. Fig. 19(e) shows the on-axis intensity spectra, corresponding to this temporal compression. Not shown here, the spectral phase at the cell exit ($z = 2$ cm) becomes nearly flat in the blue wavelengths with tiny variations comprised in the same proportions as those measured by spectral phase interferometry for direct electric-field reconstruction (SPIDER). The robustness for this self-compression mechanism was numerically found limited to rather long f/w_0 ratios and powers around $5 P_{cr}$, in order to avoid another focusing sequence (Skupin *et al.*, 2006b).

To end with this aspect, let us mention that Chen *et al.* (Chen *et al.*, 2006) also succeeded in achieving pulse self-compression from 50 to 20 fs, by making 800 nm

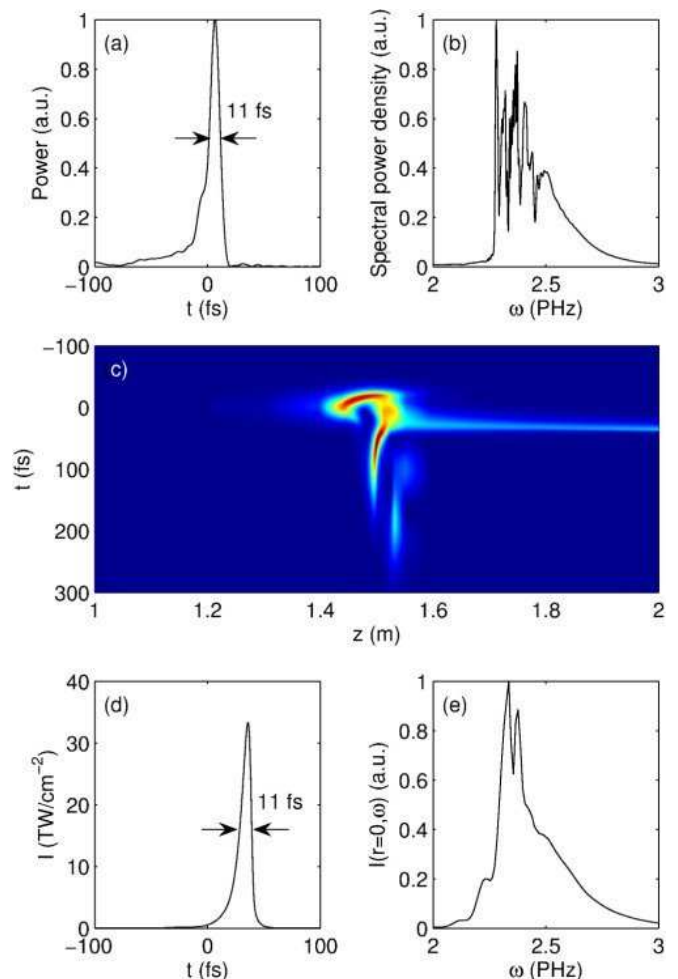


FIG. 19 (a) Experimental pulse shape for the self-compression mechanism in a 50 k-Pa argon cell, (b) associated spectrum. (c) On-axis numerically-computed temporal evolution of 45-fs pulses in the (t, z) plane for a similar setup. (d) On-axis intensity and (e) spectral intensity at $z = 1.6$ m (dashed curve) and $z = 2$ m (solid curve, exit window of the argon cell).

pulses with energy < 1 mJ pass through a thin BK7 glass plate, with no subsequent dispersion compensation. SPIDER and spectral measurements revealed that self-compression takes place as long as the front pulse focuses while plasma cuts off the trail part. At this stage, the spectrum is marked by a strong redshift. By increasing the input peak intensity, the back pulse refocuses and blueshifts the spectrum. Accounting on the balance between plasma-induced negative chirps and SPM-induced positive chirps, the spectral output phase was, again, observed to be flat. All these methods represent new promising techniques to produce high-energy few-cycle laser sources in the future.

B. High-order harmonic generation

The possibility to reduce pulse durations to a single optical cycle provides ideal conditions for high-harmonic generation and laser-assisted X-ray photo-ionization (Drescher *et al.*, 2001). Several fundamental atomic processes such as inner-shell electronic relaxation or ionization take place within a fraction of the oscillation period of visible or near-infrared radiation and they require very short probes for being investigated. For this purpose, bursts of attosecond pulses (1 as = 10^{-18} sec.) need to be isolated. This is now feasible by combining single bursts emitted at extreme ultraviolet (XUV) wavelengths and ultrashort lasers, in order to preserve the coherence properties at so short time scales. In this microcosm, the ionization processes become crucial, and more particularly the transient stage of about half laser period along which an electron is liberated. Developments in attosecond X-ray science have been addressed in several excellent reviews (Brabec and Krausz, 2000; Pfeifer *et al.*, 2006; Scrinzi *et al.*, 2006). Subfemtosecond light pulses can be experimentally obtained by superposing several high harmonics and making them emit simultaneously. By controlling their synchronization, pulses of 130 as in duration have been achieved (Mairesse *et al.*, 2003).

High-Harmonic Generation (HHG) describes the process by which laser light at central frequency ω_0 is converted into integer multiples of ω_0 during the highly non-linear interaction with the medium. In 1993, Corkum (Corkum, 1993) proposed a quasiclassical theory for this process, which can be divided into three steps:

(i) The electron is freed by ionization and driven away from the parent ion.

(ii) Since the laser field changes its sign over times about $\tau_{o.c.}/2$, this electron slows down, stops at a certain position, then re-accelerates towards the ion.

(iii) When the electron recombines with the nucleus, a photon with energy equal to U_i plus the electron kinetic energy is emitted. This gives rise to very high harmonic orders.

Figure 20 illustrates a typical HHG spectrum. The harmonic intensity is rapidly decreasing after an almost flat plateau ($\lambda < 15$ nm). It is terminated by a cut-off, signaling the highest harmonics that can be generated. Among all possible electron trajectories, there indeed exists a maximum kinetic energy corresponding to the maximum photon energy embarked by this process. The numerical solving for the electron trajectories with various phases leads this maximum kinetic energy to be $\sim 3.17 \times U_p$ (Corkum, 1993; Zeng *et al.*, 2003). Here, $U_p = q_e^2 E_p^2 / 4m_e \omega_0^2$ denotes the ponderomotive energy of the electron in the wave field (see Appendix A). Electrons thus produce harmonic photons up to the cut-off energy

$$\hbar\omega_c = 3.17 \times U_p + U_i. \quad (83)$$

The laser pulses employed in HHG experiments are generally short (< 40 fs), with the elementary profile

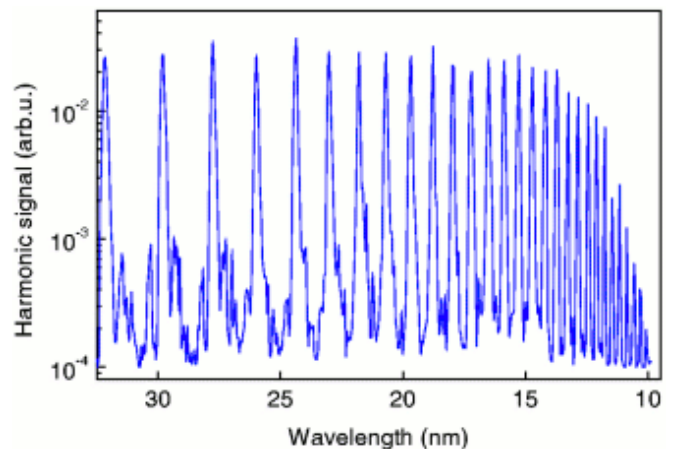


FIG. 20 Harmonic spectrum generated in neon by a 800 nm Ti:Sa laser. 25th to 81st harmonics are displayed (Salières and Lewenstein, 2001).

$E(t) = E_0 \cos(\omega_0 t + \varphi_{CE})$, where the carrier-envelope phase φ_{CE} becomes an important parameter for the conversion efficiency into HHG when approaching the optical cycle (Scrinzi *et al.*, 2006).

In ionized media with symmetry inversion, harmonic peaks only exist at odd integers multiple of ω_0 . The above three-step process repeats every half-cycle of the laser field, so that the Fourier sum in the spectra makes even harmonics cancel each other along one cycle. The analytical description of this process requires a quantum-mechanical approach of the dipole moment associated with the harmonics. To this aim, Lewenstein *et al.* (Lewenstein *et al.*, 1994) derived the time-dependent dipole moment $\vec{d}(t) = q_e \langle \psi(\vec{r}, t) | \vec{r} | \psi(\vec{r}, t) \rangle$ that represents the expected position of the electron in the quantum state $|\psi(\vec{r}, t)\rangle$. Details for computing $\vec{d}(t)$ have been given in Appendix B. The time-dependent dipole takes into account ionization at time t' , energy gain computed from a phase integrand and recombination at time t . Stationary phase conditions yield the information about the electron trajectories. By Fourier transforming the dipole moment, the harmonic spectrum can be calculated and it restores the cut-off law (83).

The challenging issue is then to describe HHG by accounting for the propagation physics of ultrashort pulses having initially a few fs durations. In 1998, Lange *et al.* (Lange *et al.*, 1998a) employed self-guided fs pulses to produce HHG up to the 15th harmonics in noble gases and maintain the longitudinal coherence of the generated harmonics. Tamaki *et al.* (Tamaki *et al.*, 1999) demonstrated experimentally efficient HHG through the phase-matched propagation of laser beams in pressurized Ne with peak intensities up to 10^{15} W/cm². By changing the propagation length, phase-matching magnifies the conversion efficiency around the 49th harmonics by 40 times near the cut-off region. Tosa *et al.* (Tosa *et al.*, 2003) reported the H13 harmonics triggered by the self-guided propagation of a focused pulse inside a 14-cm long cell

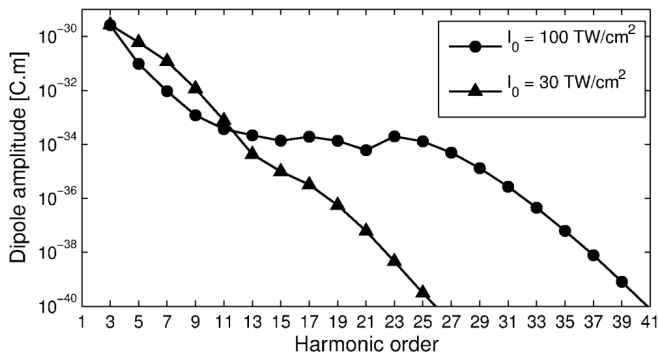


FIG. 21 Harmonic spectrum computed from the dipole moment $\vec{d}(t)$ in pressurized argon for two different pump intensities.

filled with Xe, in which the Kerr response was negligible. From these results, we easily guess that the next step in "attosecond" investigations should concern the optimization of HHG spectra by means of femtosecond filaments. The promising feature of pulse shortening induced by the balance Kerr/plasma could become an excellent technique to produce an isolated XUV pulse. Moreover, the ability to keep the laser pump clamped at sufficient high intensity over several centimeters may magnify the harmonic signal. For instance, figure 21 illustrates the amplitude of the atomic dipole computed numerically for a plane-wave pulse traversing an argon cell pressurized at 60 kPa for two different pump intensities. The HHG spectrum becomes magnified at intensity levels close to 100 TW/cm^2 . This preliminary result keeps us confident with obtaining harmonic signals with high enough energy level.

VI. ULTRASHORT FILAMENTS IN DENSE MEDIA

Below, we review major physical aspects of ultrashort filaments in solid dielectrics and in liquids.

A. Pulse propagation in dielectrics and damages

Transparent dielectrics such as SiO_2 samples were routinely examined during the 90s, in the framework of the optical breakdown on the one hand (see Sec. IV) and of the carrier trapping dynamics of band-gap crystals on the other hand. One of the key parameters being the potential gap (which is the energy difference between valence and conduction band), several investigations were led to identify this gap in silicon dioxide and to measure the ultrafast excitation and relaxation of an electron gas pumped into the conduction band by intense fs laser pulses (Audebert *et al.*, 1994; Martin *et al.*, 1997; Tohmon *et al.*, 1989).

Meanwhile, other researches concerned laser-induced breakdown (LIB) in dielectrics. The threshold damage

fluence varying as $\sqrt{t_p}$ for long pulses in thermal conduction regimes was seen to deviate from this scaling with fs pulses, for which electrons have no time to efficiently couple to the lattice. Du *et al.* (Du *et al.*, 1994) reported a damage threshold fluence higher than the $\sqrt{t_p}$ prediction rule for pulse durations $< 10 \text{ ps}$ and they furthermore underlined that short-pulse damage exhibits a deterministic nature, unlike long pulses. A theoretical model accounting for MPI, avalanche ionization and Joule heating stressed the dominant role of photo-ionization at fs time scales (Stuart *et al.*, 1996). However, both photo-ionization and avalanche come into play during the occurrence of damage. Although the role of the former is initially dominant (Rayner *et al.*, 2005), it can be masked by avalanche from an initially-high electron density ($> \rho_c/100$) (Tien *et al.*, 1999). To complete these two processes, the rapid electron decay over $\sim 100 \text{ fs}$ scales through recombination softens the maximum electron density for LIB (Li *et al.*, 1999).

Investigations mixing propagation and damage in dielectrics started from the early 2000's. Tzortzakis *et al.* (Tzortzakis *et al.*, 2001d) observed the 1-cm long self-channeling of a 160-fs focused pulse conveying 3 critical powers at 800 nm. The pulse traveled across a fused silica sample like a narrow waveguide with $\sim 20 \mu\text{m}$ waist. Local heating caused by the high repetition rate (200 kHz) and damage by local intensities $> 10 \text{ TW/cm}^2$ were avoided by making the sample move in the (x, y) plane. Auto-correlation traces revealed a two-peaked structure and spectra were asymmetrically broadened, which signaled a pulse splitting driven by plasma. Earlier, Brodeur and Chin (Brodeur and Chin, 1999) noticed a similar supercontinuum in glasses and explained it from the multiphoton excitation of electrons into the conduction band at the focus point. The low beam divergence was attributed to the Kerr-lens effect. As an example, Fig. 22(a) shows a transverse photograph of the self-guided filament measured at input energy of $2 \mu\text{J}$ in fused silica. Fig. 22(b) details the filament waist in nonlinear propagation regime and Fig. 22(c) reproduces this waist numerically computed from Eqs. (45).

At higher local intensities, the breakdown limit is approached. Because the plasma generated during breakdown remains at the threshold, a precise control of the interaction region can be reached with ultrashort pulses. This property can be used for material processing, medical laser applications as well as solid-state microelectronics. The major qualitative differences between damages caused by short ($< 10 \text{ ps}$) and longer pulses ($> 50 \text{ ps}$) appear in the damage morphology: Short pulses ablate the material, whereas long pulses produce conventional melting, boiling and fracture. With tightly focused fs pulses, permanent birefringent structures embedded in bulk fused silica have been realized over microscopic dimensions (Sudrie *et al.*, 1999, 2001). Arrays of parallel grooves formed transmission diffraction gratings with periodically-modified index changes. Two distinct types of damages can be created, namely, those consisting of lo-

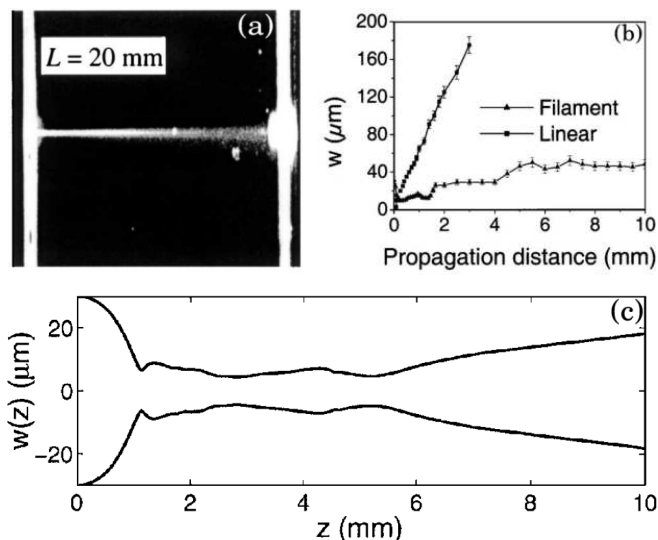


FIG. 22 (a) Transverse photograph of a single filament propagating (from left to right) in fused silica. (b) Measured diameter of the beam comparing high (linear) and low (nonlinear) divergences. (c) Numerically-computed diameter of the nonlinear filament (Tzortzakis *et al.*, 2001d).

cal isotropic increase of the refractive index at subcritical powers, and those inducing local birefringence at powers above critical. The damage track consists of diffusing zones of $\sim 20 \mu\text{m}$ transverse width. The total damage region can extend over a distance reaching 80 μm along the optical path. Numerical simulations accounting for photo-ionization, avalanche, electron recombination and Kerr self-focusing reproduced experimental damage tracks (Sudrie *et al.*, 2002, 2001), along which electron densities up to $3 \times 10^{20} \text{ cm}^{-3}$ resulted from the combined actions of photo- and impact ionization. Accounting moreover for Ohmic heating and thermal cooling by collisional ionization, Peñano *et al.* (Peñano *et al.*, 2005) numerically solved the 1D electromagnetic wave equation to quantify the transmission, reflection and absorption of 100-fs laser pulses by a thin plasma layer formed at the surface of a dielectrics. With a fluence of 3.2 J/cm^2 , the interaction fully ionizes the surface and heats the plasma to $\sim 10 \text{ eV}$. A significant transmission up to 30% of the laser energy is possible even when the plasma density is above critical ($\omega_{pe} > \omega_0$). In the layer, the electron density rapidly becomes supercritical and implies a sharp rise in the reflected pulse amplitude. Compared with MPI alone, collisional ionization increases the peak plasma density by 30%.

B. Pulse propagation in liquids and applications

Similarly to LIB in solids, the optical breakdown in fluids gained considerable interest, because it finds various therapeutic applications for, e.g., plasma-mediated laser surgery and prevention of ocular damages. First simula-

tions in water (Feng *et al.*, 1997) emphasized the dominant role of cascade ionization for long pulses, while multiphoton ionization was expected to prevail for shorter pulses. Further studies (Noack and Vogel, 1999) evaluated the absorption coefficients during the LIB process for 100 ns down to 100 fs pulses. It was established that a critical density threshold for LIB was $\rho_{cr} = 10^{20} \text{ cm}^{-3}$ for long (ns) pulses, but $\rho_{cr} = 10^{21} \text{ cm}^{-3}$ for short (ps) ones. In water and for 100-fs durations, LIB results in bubble formation supported by thermoelastic effects at pulse powers above the self-focusing threshold. This process also causes refractive index changes in the beam path upstream over several hundreds of microns. Within water droplets the tight focusing and the nonlinearities of the LIB process moreover generate a nanosized plasma hot enough to emit in the visible, and preferentially in the backward direction (Favre *et al.*, 2002).

The first experiments on fs pulse self-guiding versus the optical breakdown limit in water were performed by Liu and co-workers for different focusing geometries (Liu *et al.*, 2002). It was found that the shorter the focal length, the larger the transverse size of the optical breakdown plasma is. Self-focusing drives the initial localization of the plasma towards the beam axis. White light is generated along a short ($< 1 \text{ mm}$) filament and deflected at a small constant angle only. The supercontinuum sources for the high-frequencies were identified in the rings formed by plasma defocusing and amplified by the back of the pulse, where shocklike dynamics blueshift the spectrum (Kandidov *et al.*, 2004, 2003).

Far below LIB limits, the self-guided propagation of femtosecond filaments in water was thoroughly examined by Dubietis, Di Trapani and their collaborators a few years ago (Dubietis *et al.*, 2004a, 2003; Porras *et al.*, 2004). By launching a $\sim 3 \mu\text{J}$, 170-fs clean beam with $\sim 100 \mu\text{m}$ FWHM diameter onto a water-filled cuvette in loosely focused ($f \geq 5 \text{ cm}$) geometry, a single filament formed at the wavelength of 527 nm and was capable of covering up to 4 cm along the propagation axis, while keeping a mean FWHM diameter of a few tens of μm . The experiment revealed that the filament dynamics was not sustained by a balance between Kerr-induced self-focusing and plasma-induced defocusing. Numerical simulations outlined, instead, the spontaneous reshaping of the beam into a Bessel-type X -wave fulfilling the requirements of minimum nonlinear losses, maximum stationarity and localization. This scenario has been discussed in Sec. IV.A, where the important role of the laser wavelength in selecting the key player able to saturate the wave collapse and support the self-guiding process was underlined. For this purpose, Fig. 23(a) illustrates the pulse fluence along the self-guiding range measured at the exit plane of a 31-mm long cuvette for $P_{in} = 6.6 P_{cr}$. Fig. 23(b) shows the X -shaped spectral-angular distribution of the radiation. Plots (c,d) represent peak intensities and FWHM diameters reached with similar pulse parameters with and without plasma gain, which evidences the weak influence of plasma defocusing in this dynamics

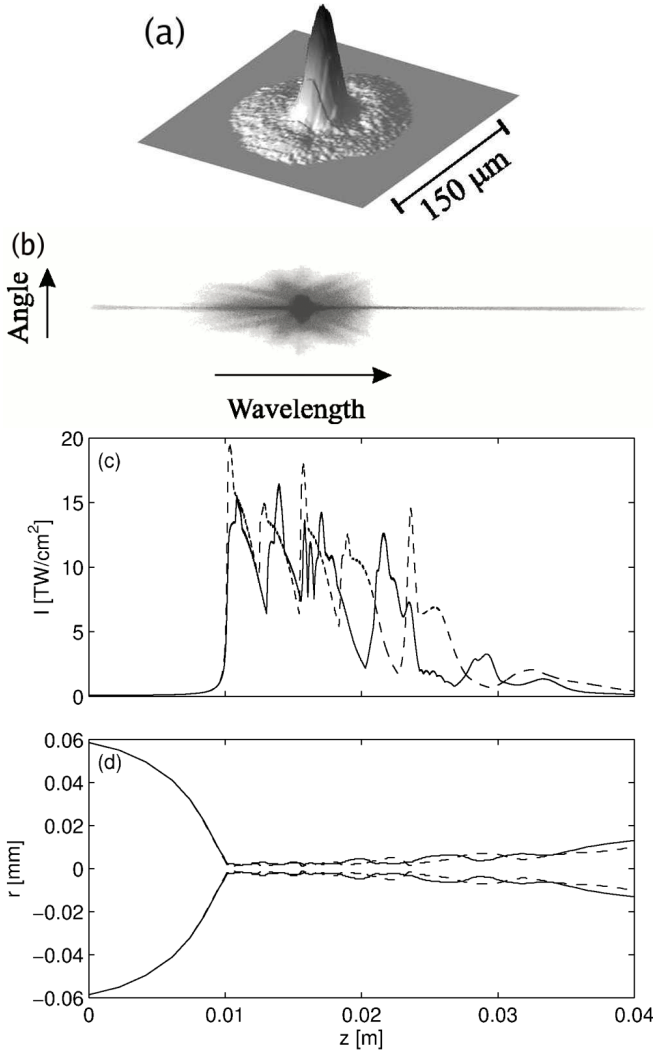


FIG. 23 (a) Normalized 3D beam profile at the output of the water cell (31 mm); (b) Spectral-angular distribution of the radiation (Dubietis *et al.*, 2003). Courtesy of A. Dubietis. (c) Peak intensities computed numerically with (solid curve) and without (dashed curve) plasma gain from 170-fs, 100- μm -waisted pulses focused with $f = 5$ cm ($P_{\text{in}} = 10 P_{\text{cr}}$) in water; (d) Corresponding FWHM radius.

(Skupin *et al.*, 2006a).

Increasing more the pulse power leads to multiple filamentation, which has been addressed in a few papers (Cook *et al.*, 2003; Heck *et al.*, 2006; Schroeder *et al.*, 2004). By using a cylindrical planoconvex lens, Cook *et al.* produced horizontal arrays of stable white-light filaments in water at 800 nm, allowing interference effects between neighboring cells. Similarly to a pair of Young's slits, a filament pair creates interference patterns, which is the signature for a constant phase relationship between the supercontinua generated by the filaments (the same property applies to atmospheric filaments; see Sec. VII.A.4). Those thus appear as coherent sources of white-light. Besides, Schroeder *et al.* demon-

strated the possibility to arrange filaments in water into 1D arrays of parallel, non-overlapping spots by clipping the impinging laser beam by a slit aperture built from razorblades. Metallic wire meshes can also be used to generate space-controlled 2D arrays of filaments. Recently, Heck *et al.* demonstrated the efficiency of an adaptive control over the position and extent of filaments in water tanks, through a closed feedback loop setup employing a spatial light modulator and a genetic algorithm that allow to manipulate the amplitude and phase of the input pulse.

Apart from water, other fluids can support femtosecond filamentation, such as alcohols like ethanol or methanol. Dyes may be introduced into these liquids, in order to visualize the filamentary evolution through one, two or three-photon fluorescence and modify the multifilamentation patterns by varying the dye concentration (Guyon *et al.*, 2006; Liu *et al.*, 2005a, 2003; Schroeder and Chin, 2004). Relying on the dye nonlinear absorption, the structural changes of the filamentation becomes visible to the eyes, due to the fluorescence from the dye molecules excited by multiphoton excitations at visible wavelengths. From a dilute solution of methanol and Rhodamine B, Schroeder and Chin figured out that femtosecond filaments propagate straight, may die off prematurely or fuse into new spots. Along the propagation axis, "mature" filaments ending after the bright fluorescence zone were identified. By means of the same techniques, Liu *et al.* observed multi-focusing events by increasing the beam energy in methanol doped with 0.13% of Coumarin 440 at 800 nm. The photon bath surrounding the 20- μm large filament core was numerically examined: It was found that the near-axis region takes energy from a ring-shaped region limited to $r < 60 \mu\text{m}$ around the filament core. Outside, the peripheral domain ($r > 60 \mu\text{m}$) acquires energy. The resulting energetic balance preserves an almost constant energy in the near-axis region. Nonlinear fluorescence techniques were recently used to discriminate between multiphoton absorption and conical emission by z -scan analysis using metal meshes (Liu *et al.*, 2005a). It appears that the energy loss caused by conversion into CE (40%) is much higher than that caused by MPA ($\sim 3\%$) at powers $< 8P_{\text{cr}}$ (see also Sec. IV.A). Finally, Guyon *et al.* employed Coumarin 153 in dye-doped cells of ethanol. At high dye concentration (4 g/l), the filamentation pattern was shown to self-organize into a latticelike (hexagonal) figure, by letting the two-photon absorption of Coumarin switch out filamentary sites in the (x, y) plane. Pump-dump experiments furthermore revealed that, at all filamentary sites, excited Coumarin molecules could coherently relax by fluorescence and emit in-phase light stimulated by the dump pulse, i.e., a collection of filaments can be used as microscopic laser sources in dense media. Figure 24 summarizes some of these observations.

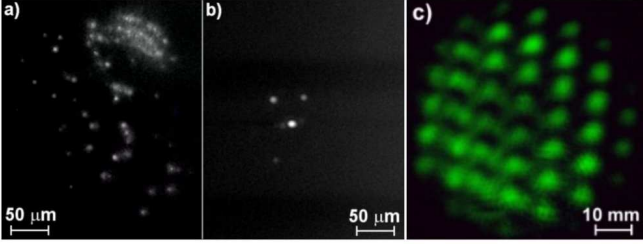


FIG. 24 Filamentation pattern obtained from a 1-cm long cell of (a) pure ethanol, (b) dilute solution of ethanol/Coumarin 153 at 4 g/l, (c) far-field fluence distribution of excited states of Coumarin emitting simultaneously in phase.

VII. FILAMENTS IN THE ATMOSPHERE: CONVEYING INTENSE STRUCTURES OVER KILOMETERS

The final section is devoted to the medium which originally served as the "birthplace" for the science of femtosecond light filaments, namely, the atmosphere. Special emphasis is laid on experimental diagnostics. From the theoretical point of view, filamentation in air is modeled from Eqs. (45), using classical dispersion relation in air (Peck and Reeder, 1972). Although of weaker percentage (20% vs 80% in air), dioxygen molecules have a lower ionization potential than nitrogen and they provide the dominant species prevailing through ionization (Couairon *et al.*, 2002).

A. Long-distance propagation and white-light supercontinuum

1. Temporal chirping and spatial lensing

The propagation of high-power (TW) femtosecond laser pulses in air has attracted considerable attention from the pioneering observation of the white-light supercontinuum beyond 10 km (Wöste *et al.*, 1997). A number of important practical applications have been suggested, including remote sensing (Rairoux *et al.*, 2000), directed energy delivery and artificial lightning (LaFontaine *et al.*, 1999a) among others. Because the filament onset and length are key parameters for spectroscopic measurements and for depositing high intensities on remote targets, monitoring these parameters are of utmost importance. To achieve high intensities at remote distances, a negative frequency chirp can be introduced in the laser pulse (Alexeev *et al.*, 2004; Wille *et al.*, 2002). In addition to transverse self-focusing, the pulse undergoes a temporal compression as it compensates the normal group-velocity dispersion along the propagation axis. Chirping effects can be measured by evaluating differences in the conical emission with and without pulse chirping (Rodriguez *et al.*, 2004). For instance, the vertical propagation of the Teramobile beam, presented in Appendix C, was examined from the ground using the 2-m astronomical telescope of the Thüringer Landesstern-

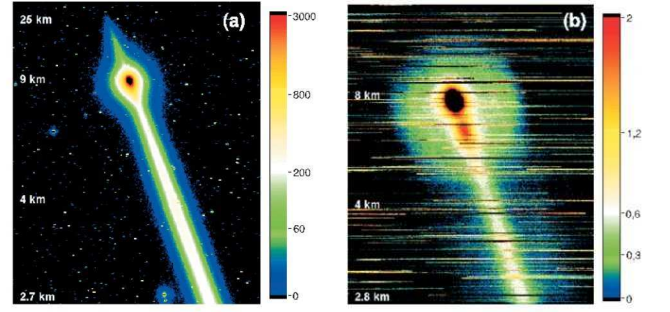


FIG. 25 Typical fs beam image of the Teramobile laser beam from Tautenburg observatory. (a) Fundamental wavelength; (b) Blue-green band of the continuum. The horizontal stripes across the pictures come from stars passing through the telescope field of view. Note the strongly nonlinear altitude scale due to triangulation.

warte (Thuringia State Observatory, Germany). Collected images were a combination of both (i) cross-section images of the beam impinged on the bottom of clouds or haze layers acting as screens, and (ii) side imaging of the Rayleigh-scattered light from the beam over large altitude ranges. Some of these images are shown in Fig. 25 at both the fundamental wavelength and the white-light continuum. In this case, the altitude was retrieved using triangulation. Figure 25(b) demonstrates the efficiency of the supercontinuum generation, since its blue spectral signal has been detected from altitudes beyond 18 km for appropriate chirping. These experiments demonstrated for the first time the possibility to deliver high-intensities and generate white light upon variable km distances, by means of GVD/chirp precompensation techniques. The same observation assessed that the conical emission bears two thirds of the overall white-light energy, while the on-axis, forward-directed central component carries the remaining one third.

To modify the filamentation distance, a chirp is usually introduced by changing the distance between the gratings of CPA laser compressors. Applied to the Gaussian pulse (46), this technique modifies the second-order phase contribution $\varphi'' = d^2\varphi/d\omega^2|_{\omega=\omega_0}$. It enhances the input pulse duration and decreases the beam power as

$$t_p^C = t_p^{C=0} \sqrt{1 + C^2}, \quad P^C = P^{C=0} / \sqrt{1 + C^2} \quad (84)$$

at equal spectral content. As it linearly propagates, the pulse competes with normal GVD and reaches the minimal duration $t_{\min} = t_p^{C=0}$ at the distance

$$z_{\min} = \frac{|C|}{1 + C^2} \frac{t_p^2}{2k''}. \quad (85)$$

Pulse chirping mixes two essential modifications. The first one is dictated by the phase $\sim e^{-iCt^2/t_p^2}$. For input powers above P_{cr} , a positive chirp $C > 0$ delays the occurrence of the self-focus point, whereas this occurs earlier along the optical path for a negative chirp ($C < 0$).

The second one results in diminishing the effective pulse power, which pushes the first focus to later propagation distances and reduces the number of filaments in case of multifilamentation, whatever the sign of C may be. In usual experimental conditions, this second effect prevails over the first one. Despite the strong nonlinearities driving the filament dynamics, the chirped-induced linear compression stage still persists with $C < 0$. It gives rise to additional focusing events and keeps the beam localized at distances close to z_{\min} (Golubtsov *et al.*, 2003; Nuter *et al.*, 2005). Moreover, the generation efficiency of the supercontinuum may vary by several orders of magnitude compared with that of a transform-limited pulse.

The onset distance and longitudinal extent of fs filaments are also conditioned by the initial spatial focusing geometry. No simple analytical rule exists on this point, because of the complex spatial distortions destroying the initial homogeneity of the beam. The filament length moreover depends on the energy consumed by plasma excitation and on the accessible peak intensity. However, most of the experiments emphasize the use of rather large ratios f/w_0 , in order to avoid an immediate plasma defocusing in tightly focused configuration. This property can be refound by integrating the dynamical equations (59) derived from the two-scale variational method. The variational principle indicates that at given $P_{\text{in}}/P_{\text{cr}}$ the ratio f/z_0 must be large enough to insure the self-trapping condition $z_c \leq f$. Otherwise, for $f/z_0 \ll 1$, the beam diffracts just after the focal point. Figure 26(a) shows the beam diameter of 100-fs, 1-mm-waisted pulses in air at $P_{\text{in}} = 10 P_{\text{cr}}$ and various focal lengths f , which confirms the previous belief. Figure 26(b) represents the beam extent along the z axis of temporally-chirped, 3-mm-waisted pulses with $C = 0$ (dash-dotted curve), $C = 1.02$ (dotted pulse) and $C = -1.02$ (solid curve).

2. Plasma and optical field measurements

Plasma detection relies on the existence of a difference of potential produced by the current generated by ionization of air molecules. Working in free atmospheric medium makes it easy to measure the conductivity of the plasma channel, that causes a drastic reduction of air resistivity after the passage of a self-guided filament. This conducting column can directly be evidenced by letting the filament pass between two copper electrodes drilled in their center and between which a DC voltage of typically 1000 V is applied (see Fig. 27). The current circulating through the plasma column is then measured by recording the voltage induced across an external load resistance (Tzortzakis *et al.*, 1999, 2001c). Knowing the current density per ion ($i = 3 \times 10^{-14}$ A/cm²) and taking into account the volume occupied by a plasma filament, peak electron densities of $10^{16} - 10^{17}$ cm⁻³ have been reported in air at 800 nm. Another technique consists in resolving in time small local changes in the atmospheric refractive index by diffractometry

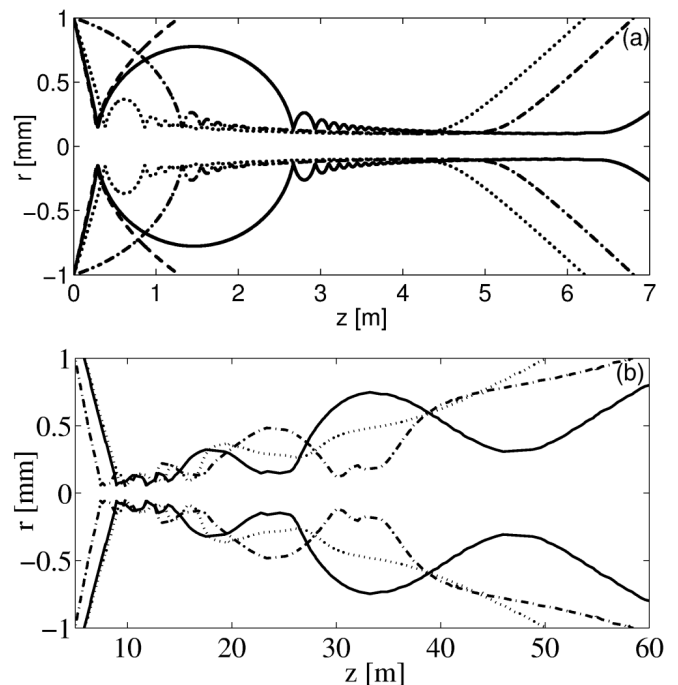


FIG. 26 (a) Beam diameter of pulses spatially focused with $w_0 = 1$ mm, $f = 35$ cm (dashed curve), $f = 37$ cm (solid curve), $f = 50$ cm (dotted curve), $f = 5$ m (dash-dotted curve); (b) Beam diameter vs. $z \geq 5$ m for temporally-chirped, 3-mm-waisted pulses with $C = 0$ (dash-dotted curve), $C = 1.02$ (dotted pulse) and $C = -1.02$ (solid curve).

(Tzortzakis *et al.*, 2000b). The principle is here to use a probe beam that crosses the filament path under a small angle. The far field image of the probe forms fringe patterns, that yield a direct measurement of the accumulated phase containing the plasma-induced defocusing effect. Let us also mention sonographic methods, that take advantage of the sound signals along the plasma column (Hao *et al.*, 2005b; Hosseini *et al.*, 2004b; Yu *et al.*, 2003). This "acoustic" diagnostics employs a microphone placed perpendicularly to the channel and recording the sound signals by a digital oscilloscope. The sound emitted from a plasma string is a portion of the pressure modulation of an acoustic wave from which the absorbed optical energy and plasma density are deduced from the electric peak voltage at a given distance z . By doing so, the variations in the electron density can then be plotted along the propagation axis.

Plasma lengths attained from single \sim mJ femtosecond pulses currently remain of the order of the meter. The combination of twin pulses, launched collinearly in convergent geometry and separated from each other by a suitable time delay, can, however, double this length (Couairon *et al.*, 2003; Tzortzakis *et al.*, 2003). This process, called "concatenation" of plasma filaments, relies on locking together the ionized channels generated by each individual pulse. By tuning their focal lenses ($f_2 - f_1 \sim 1$ m) and their time separation ($\simeq t_p$), the less powerful time slice ending the self-guiding of the first

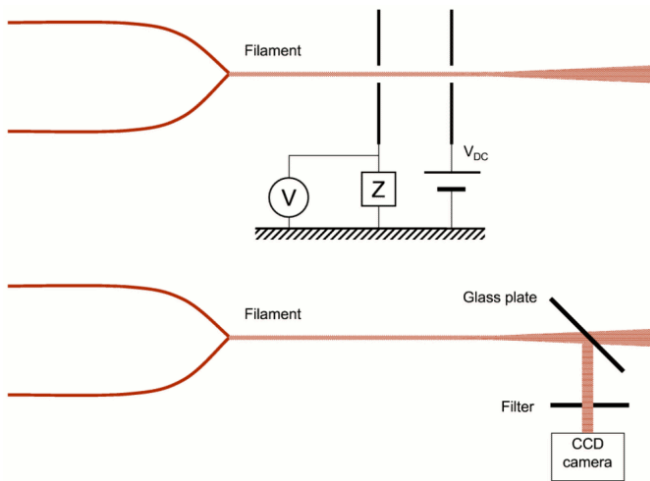


FIG. 27 Schemes of experimental setups for (a) conductivity measurements and (b) CCD imaging for optical field measurements.

pulse coincides with the most powerful one of the second pulse starting a new plasma column (Bergé, 2004).

Experiments over a horizontal path provided more information about the length over which ionized plasma channels are formed (Méchain *et al.*, 2005a). The influence of an initial negative chirp enlarging the pulse duration from 0.2 to 9.6 ps, corresponding to 190 and 4 P_{cr} at constant energy (190 mJ), respectively, was especially examined upon distances up to 2350 m. Whereas ionization is clearly observed over propagation scales < 50 m for short pulse durations (0.2 ps), it becomes more and more sporadic for durations above 3 ps and ceases for 9.6-ps pulses, i.e., at powers becoming close to critical. In this case, a few low-intensity ($\sim 10^{12}$ W/cm²), mm-waisted spots survive inside the photon bath, still capable of covering several hundreds of meters. The bundle does not convey enough power to trigger full ionization. Instead, the beam evolves in a regime along which GVD is able to take over MPI and sustain the beam in a confined state over distances of the order of the input Rayleigh length (Champeaux and Bergé, 2005). When the initial power is too weak, broad beams may produce a few bright spots by modulational instability, but none of these is capable of developing extensive plasma sequences (see Fig. 8).

Several diagnostics exist for optical field measurements. The first consists in recording intensity profiles by a thick glass plate placed on the propagation axis at $\sim 45^\circ$ angle (Fig. 27). The weak reflection from the glass is then imaged with a high-aperture lens onto a linear charge coupled device (CCD) camera (Tzortzakis *et al.*, 2001a). Detection is performed out of the highest-intensity region close to the nonlinear focus, in order to leave the entrance window of the glass plate undamaged and keep up the reflected beam undistorted. Also, the high repetition rate of the laser source may not avoid multi-spot measurements. For this reason, Bernstein *et al.* (Bernstein *et al.*, 2003) reported on single-shot

measurements of self-focusing pulses that do not have the intensity required to produce ionization. Besides a CCD camera, a spectrometer and second-harmonic frequency-resolved optical gating (FROG) device allowed to measure the spatial, spectral and temporal distributions of the pulse, respectively. The data, collected from an initially collimated Gaussian beam, showed spatial and temporal narrowing and spectral broadening at discrete energy levels preceding the ionization stage. They confirmed a critical power value for nonlinear compression effects of 11.5 GW for 800 nm pulses, i.e., about $\sim 10 - 15$ GW. Nowadays, several diagnostics such as SPIDER and crossed (X)FROG traces complete standard auto-correlation pictures and spectra to catch the spatio-temporal structure of a pulse in the (ω, t) plane. To explore the filamentation stage along which intensities as high as 5×10^{13} W/cm² are attained, Ting, Gordon and co-workers (Gordon *et al.*, 2006; Ting *et al.*, 2005a,b) elaborated on a new method following which the filament is propagated into a helium chamber through a nozzle that creates a sharp air-helium interface. Because helium has lower Kerr index and higher ionization potential than air, nonlinear focusing and plasma defocusing are arrested at the transition in the chamber. The filament then expands due to diffraction to larger sizes and lower intensities. A calibrated portion of energy can safely be collected and imaged either directly by a CCD array or through an imaging spectrometer.

3. Multifilamentation

Open-air terawatt laser facilities make it possible to observe optical focal spots formed by a myriad of filamentary cells for input powers containing several thousands of critical powers in air. The 2D reduced model (71) using the experimental fluence as initial condition actually reproduces the evolution of the multifilamentation pattern over long scales, saving computational resources when one neglects the temporal dimension. As an example, Fig. 28 shows the overall envelope of the Teramobile bundle (see Appendix C) launched in parallel geometry. The initial pulse contains 700 critical powers and its transverse profile is scanned at different propagation distances. Filaments rise from the initial beam defects, form a crown of dots growing from the diffraction ring and then excite clusters of cells. These clusters, some of whose are identified by the labels (1), (2) and (3), are faithfully reproduced by the numerics. The filament number remains in the order of P_{in}/P_{fil} , where $P_{fil} \simeq 3 - 5P_{cr}$ is the power in one filament. At large distances, the primary brightest spots decay into secondary filaments by exchanging power through the energy reservoir formed by the background field (Bergé *et al.*, 2004).

When the focusing geometry is changed, the filamentation pattern becomes severely modified. Figure 29 shows a longitudinal visualization of the filaments nucleated in a beam with 760 P_{cr} and focal length $f = 40$ m. The

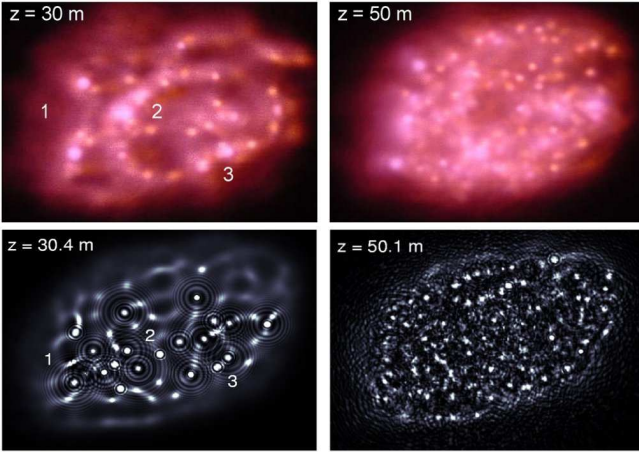


FIG. 28 Filamentation patterns from the Teramobile beam with $w_0 = 2.5$ cm, FWHM duration of 100 fs and input power equal to $700 P_{cr}$ at different distances z . (top) Experiments; (bottom) Numerical computations.

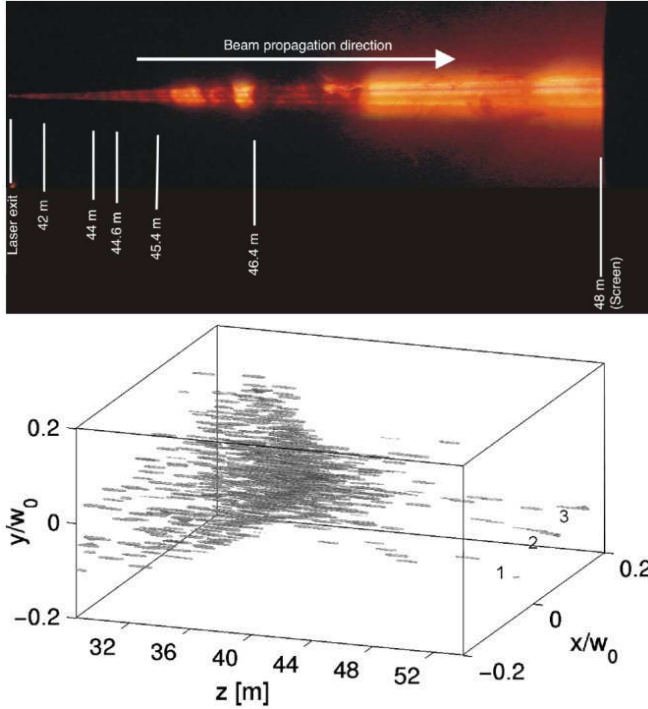


FIG. 29 Teramobile fluence of a focused beam ($f = 40$ m) with 760 critical powers, yielding three filamentary strings beyond the linear focal point: (top) Experiment, (bottom) numerical computation from the 2D model (71).

beam is directed towards an open cloud chamber scattering a weak-density cloud. After the focal point, only three strings of light emerge and cover about ~ 8 m each, while the same beam should produce more than one hundred filaments in parallel geometry. Numerical computations for this configuration clear up that many filaments are created before the linear focus, but they fuse into three strings of light acquiring a high directiv-



FIG. 30 Open cloud chamber. The cloud spans over 10 m.

ity afterwards (Skupin *et al.*, 2004b). The same experimental setup (Fig. 30) put in evidence the robustness of femtosecond filaments through a multitude of $1 \mu\text{m}$ large water droplets randomly-distributed at various densities in the 10-m long cloud chamber. A filament is still transmitted through a cloud with an optical thickness as high as 3.2. For a cloud optical density of 1.2 or below, corresponding to cumulus or stratocumulus, the filamentation does not seem affected. Filaments remain visible at the exit of the fog even for a droplet concentration so high ($8.6 \times 10^4 \text{ cm}^{-3}$) that each filament hits on the average 2000 droplets per propagation meter. The corresponding extinction coefficient is 0.2 m^{-1} . Hence, filamentation can be transmitted through a fog over distances comparable with the visibility length. Energy losses due to random collisions implies an exponential decrease of power, which modifies the number and position of the filaments in the bundle (Méjean *et al.*, 2005). Such experiments, whose results are recalled in Fig. 31, permitted to estimate the power per filament to about $5 P_{cr} \sim 15 \text{ GW}$ in air (see bottom panel).

Pulse propagation in adverse weather becomes an important topic for LIDAR applications. In this scope, Kandidov *et al.* addressed the point of the nucleation of filaments in a turbulent atmosphere supporting statistical fluctuations of the refractive index (Kandidov *et al.*, 1999). These fluctuations naturally arise as the medium becomes, e.g., locally heated. On the basis of a phase screen model, the cubic NLS equation including statistical variations of the linear optical index (Kolmogorov turbulence) describes random paths for the nucleation and position of the nonlinear focus. This focus appears on the average shorter compared with unperturbed air and the beam centroid moves along a random path in the (x, y) plane. This induces a transverse deflection of the beam axis by several mm, which was later observed from experimental averaged data (Chin *et al.*, 2002b). Besides this beam wandering, femtosecond filaments keep their posi-

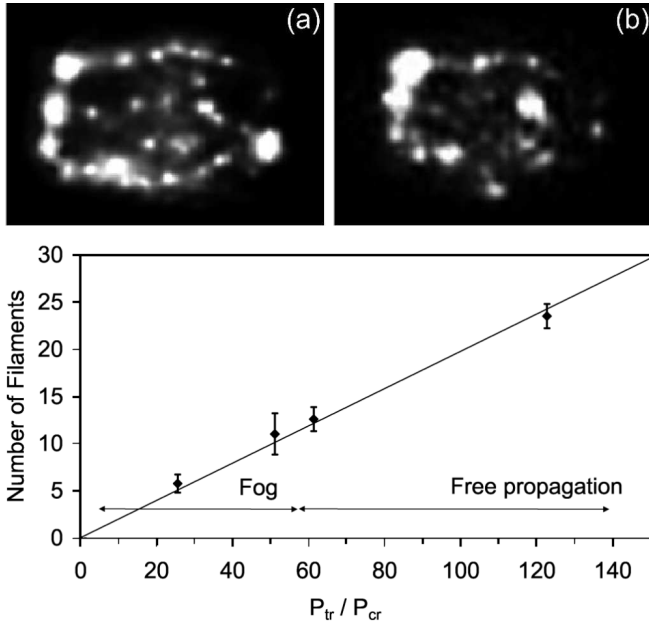


FIG. 31 Modification of a filamentation pattern with $\sim 120P_{cr}$ over 50 m: (a) in dry air and (b) after traversing a 10-m long tube of fog. The bottom panel reports the filament number vs. the transmitted power over critical.

tion stable relatively to the bundle in highly turbulent regions, as the index variation caused by the nonlinearity exceeds turbulent-induced refractive-index gradients by two orders of magnitude (Ackermann *et al.*, 2006b).

Furthermore, the influence of pressure variations on TW laser pulses was recently investigated. This issue is timely, as filaments propagating vertically over several km undergo an exponential decrease of the local pressure, $p(z) = p_0 e^{-z/L_a}$, where $L_a = 8$ km is the attenuation length for air density (Sprangle *et al.*, 2002). Pressure variations induce proportional changes in the GVD coefficient, the Kerr refractive index and molecule density available for ionization, as recalled by Eq. (82). At reduced pressure (0.7 atm), experiments performed at 3230-m altitude above sea level revealed farther filamentation onset and reduction of the filament number linked to the decrease of $n_2(p)$ by 30% (Méchain *et al.*, 2005b). The filamentation process, especially the filament length, was shown to be qualitatively unaffected. Numerical simulations in this field specified that a single atmospheric filament does not indeed significantly change its self-channeling range and keeps an almost constant peak intensity. In contrast, the plasma level, the filament width [Eqs. (76)] and the nonlinear focus (50) evolve with p and \sqrt{p} , respectively, due to the effective increase of $P_{cr}(n_2)$. Multifilamentation patterns have their onset distance governed by the maximum rate for modulation instability $\gamma_{max} \sim 1/n_2(p)I_0$ [see Eq. (74)]. This length thus varies linearly with air pressure (Champeaux and Bergé, 2006).

4. White-light generation

The white-light continuum generated in air by ultra-short laser pulses is essential in view of LIDAR applications, since it constitutes the light source used in multipollutant remote sensing. This white light was characterized over the last years, with progressively extending bandwidths. The supercontinuum has first been characterized in the visible (Alfano and Shapiro, 1970; Nishioka *et al.*, 1995). J. Kasparian *et al.* next investigated the infrared region (Kasparian *et al.*, 2000b). Two different terawatt CPA laser systems (A: 60-mJ energy, 35-fs minimal pulse duration, 25-mm FWHM beam diameter; B: 100-200 mJ, 100-fs minimal pulse duration, 35-mm FWHM diameters) produced spectra measured at a total distance of ~ 30 m from the lens, as the laser beam was diffracting after 20 m of filament propagation. Illustrated in Fig. 32(a), the continuum band developed from laser system A is very broad, extending at least to $4.5 \mu\text{m}$. An almost exponential decay over 4 orders of magnitude up to $2.5 \mu\text{m}$ is observed, followed by a slower decay of one order of magnitude only. As shown from the inset plotting results from laser system B, variations in the input energy makes spectral intensity change by only one decade in some spectral regions. The spectral shape of these different pulses remains, nevertheless, quite similar within one decade in spectral intensity. Extension to the UV-visible domain down to 230 nm (Fig. 17) is not represented, as it was detected later. For comparison, Fig. 32(b) shows the numerically-computed spectrum of a 0.5-mm waisted, $4P_{cr} \sim 10$ GW, 100-fs pulse after a single femtosecond filament has been generated in air by accounting for third-harmonic generation in the limits $T, T^{-1} \rightarrow 1$ (Bergé *et al.*, 2005) and from the full UPPE model (43). The experimental and numerical spectral shapes are similar up to $1.2 \mu\text{m}$. Differences, however, occur at larger wavelengths, as space-time focusing and self-steepening are included, which shortens the red parts of the spectrum to some extent. Recovering the experimental redshifts from the UPPE model in air is still an open issue.

The similarity of white-light spectra emitted by TW laser pulses (experiments) and GW pulses suggests that the multifilamentation produces a spectrum analogous to that generated by a single filament. This conclusion is consistent with Chin *et al.*'s experimental observations about the coherence properties of femtosecond filaments (Chin *et al.*, 2002a). Observation of the interference pattern produced by two or more filaments allowed to predict that they emerge in phase from the background field and they possess the same phase relationship. This means that the laser spectrum around the central wavelength in the conditions of multiple filamentation is in principle identical to that developed by an isolated filament.

The previous property is important for LIDAR applications, because it suggests that the comprehension of the spectral dynamics of one filament is sufficient for understanding the spectral dynamics of multifilamented

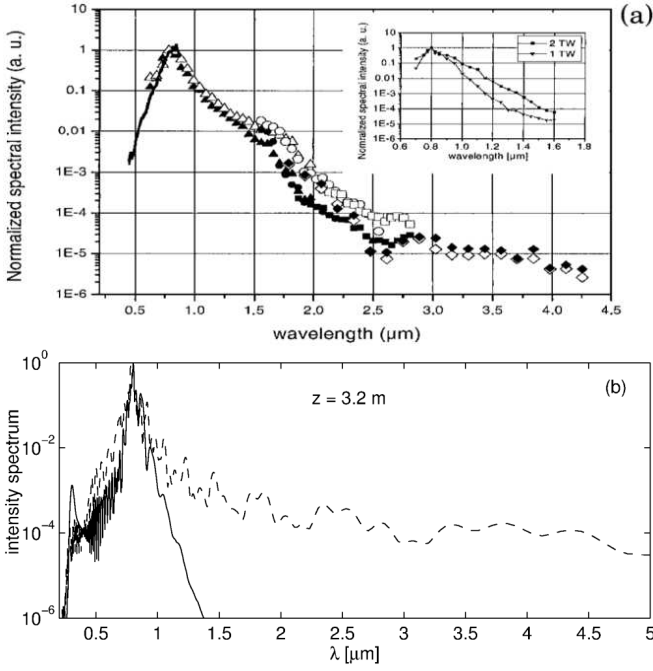


FIG. 32 (a) Measured white-light spectrum by 2-TW laser pulses (laser system A). Chirp settings correspond to 35-fs initial pulse duration without chirp (filled symbols) and 55-fs initial pulse duration with negative chirp (open symbols). Inset, spectrum measured from laser system B. The two curves have the same normalization factor. (b) Spectrum for a single filament numerically computed from Eqs. (45). The dash-dotted curve includes TH generation in the limits $T, T^{-1} \rightarrow 1$, while the solid curve represents the spectrum calculated from the complete equation set.

beams. In addition to the wide spectral region covered by nonlinear femtosecond pulses, the strong enhancement of the backscattered photons in filamentation regime makes ultrashort laser pulses quite promising tools for the remote identification of multipollutants in aerosols. Indeed, the supercontinuum emitted by a filament is enhanced in the backward direction [see Eq. (14)], i.e., towards the laser source, compared with linear Rayleigh-Mie scattering (Yu *et al.*, 2001).

B. Remote sensing (LIDAR) applications

1. Principle of LIDAR: Towards "Femtolidars"

The LIDAR (LIght Detection And Ranging) technique (Fujii and Fukuchi, 2005; Measures, 1984; Theopold *et al.*, 2005; Wolf, 2000) was demonstrated shortly after the advent of the first lasers. In this technique, a laser pulse is emitted into the atmosphere. The backscattered light is collected on a telescope and detected as a function of time, with a typical resolution of 1-10 nanoseconds. This temporal window yields a high spatial resolution, since the flight time of the detected photons is directly proportional to the distance

where they have been backscattered. Such a spatial resolution, combined with the possibility of sweeping the laser beam, provides two- and three-dimensional maps of measured atmospheric species. This is the main advantage of LIDAR over other measurement methods for atmospheric trace-gases. One of the most popular LIDAR techniques is called DIAL (Differential Absorption Lidar). It allows to selectively measure the concentration of gaseous pollutants by comparing the Lidar signals at two wavelengths nearby to one another, one being on an absorption line of the pollutant, and the other just beneath. However, this method is basically limited to pollutants that exhibit a narrow absorption line without interference from the absorption spectra of other atmospheric compounds. Moreover, the need to tune the laser wavelength on the absorption line forbids to simultaneously identify more than one pollutant within one acquisition.

Femtosecond Lidars (or so-called "FemtoLidars") overcome classical DIAL limitations. Exploiting the "Femtosecond atmospheric lamp" discovered in 1997 by Wöste *et al.* (Wöste *et al.*, 1997), high-power ultrashort laser pulses can be shined vertically into the sky, where they generate white-light through the filamentation mechanism. The backscattered light, recorded with a telescope linked to a time-gated spectrometer, then provides a fascinating vector for atmospheric research over km ranges (Rairoux *et al.*, 2000; Rodriguez *et al.*, 2004). The spectral bandwidth developed by fs filaments is very broad, since it spans at least from 230 nm in the ultraviolet to 4.5 μm in the mid-infrared (Figure 33). On the spectrum, the absorption band of water between 1.8 and 2.5 μm is clearly visible, showing the potential of white-light for optical remote sensing in the atmosphere. It also covers the absorption band of volatile organic compounds (VOCs) between 3 and 3.5 μm . VOCs constitute a family of organic compounds with strongly overlapping absorption spectra, which prevents any measurement by classical DIAL techniques. In addition, the flat continuum spanning from the visible down to 230 nm through third-harmonic generation (see Fig. 17) provides a promising light source for the measurement of trace gases that absorb in the blue or the UV, such as ozone, toluene, benzene, SO_2 or nitrogen oxides. Recently, femtosecond laser-induced filaments were also applied for greenhouse gas methane (CH_4) in air (Xu *et al.*, 2006a). Intense filaments dissociate pollutant molecules into small fragments, which emit characteristic fluorescence. This can be used to remotely measure the pollutant concentration at characteristic spectral lines.

Besides, multiparameter measurements are necessary to monitor the dynamics of atmospheric physico-chemistry or to remotely analyze a cocktail of species emitted during a chemical accident. They are also requested to characterize the nucleation and maturation of clouds. Such processes play an important role for atmospheric modeling, both on meteorological and climatological scales. In particular, the droplet growth and

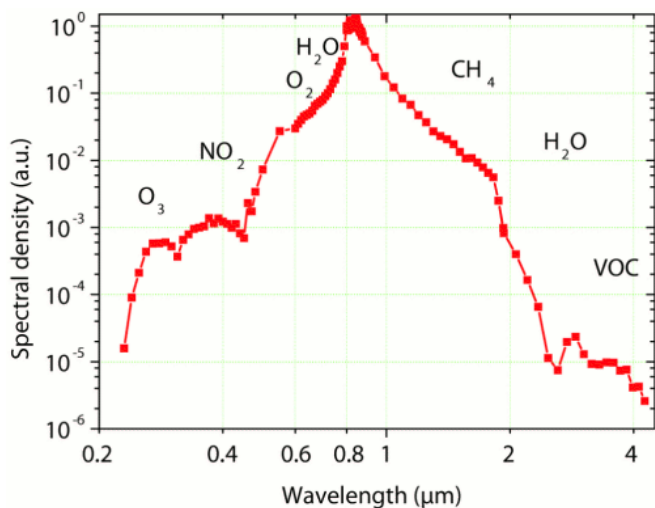


FIG. 33 Spectrum of the white light continuum assembled from five spectral regions. Main atmospheric absorption bands are marked above the curve.

related density have a key influence on the forecast of both precipitations and earth albedo. Their characterization requires continuous measurements of the size distribution inside the clouds, with a temporal resolution of a few tens of minutes, compatible with the evaporation and growth time ranges. While airborne measurements are too expensive for routine monitoring, radiosounding does not provide the adequate repetition of probing. Therefore, optical techniques are promising, and they can be made optimal with fs laser pulses. As an example, a high-resolution absorption spectrum over a spectral interval larger than 200 nm is shown in Fig. 34, based on the white-light continuum, providing both the water vapor concentration and the temperature of air (Bourayou *et al.*, 2005; Kasparian *et al.*, 2003). Once combined, these two parameters supply the relative humidity, which is the relevant factor for atmospheric dynamics. Moreover, angular measurements of the multiple scattering yield the size distribution and concentration within the clouds, through an inversion of the laws of multiple Mie scattering based on a genetic algorithm. These measurements require the same laser source and two independent detectors. With fs Lidar setups, they can be implemented simultaneously so as to yield a complete characterization of the cloud microphysics.

"FemtoLidars" are not restricted to the white-light Lidar. The high intensities carried in the filaments can generate nonlinear effects *in situ* on a target. Such nonlinear processes, which include ablation, ionization and multiphoton-excited fluorescence (M-PEF), constitute a supplementary information channel for remote sensing. An example of this technique has been provided by the remote detection and identification of biological aerosols through 2-PEF Lidar (Méjean *et al.*, 2004). Here, the purpose was to detect and locate rapidly a suspect emission, to map the emitted cloud, and to identify poten-

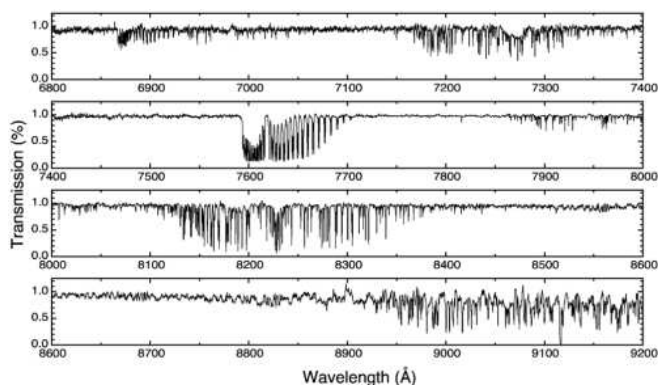


FIG. 34 High-resolution atmospheric absorption spectrum from an altitude of 4.5 km measured in a Lidar configuration. The broad spectrum allowed to simultaneously measure the air temperature and humidity.

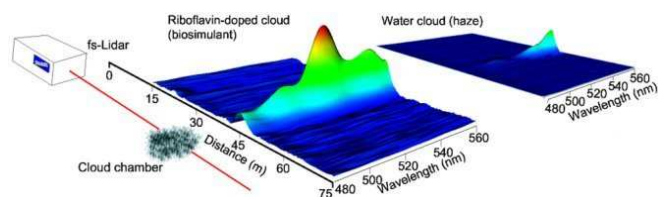


FIG. 35 Remote detection and identification of bioaerosols. The femtosecond laser illuminates a plume of riboflavin (RBF) containing microparticles 45 m away (left). The backward emitted 2-photon excited fluorescence (2-PEF), recorded as a function of distance and wavelength, exhibits the specific RBF fluorescence signature for the bioaerosols (middle) but not for haze (right).

tially pathogen agents among the multiple background atmospheric aerosols, including organic compounds such as soot or pollens. The 2-PEF allowed, for the first time, to remotely identify aerosols simulating biological agents in air by nonlinear Lidar (Fig. 35). Moreover, collected signals based on N-PEF become more efficient than Lidar signals based on 1-PEF for distances above a few kilometers. This is due to two effects: (i) the directional emission of the N-PEF from the aerosol particles minimizes the decrease of the collection efficiency with increasing distances (Boutou *et al.*, 2002), and (ii) the visible or near-infrared wavelengths used for exciting N-PEF, compared to the UV wavelength required for 1-PEF, experiences less attenuation in the atmosphere because of the $1/\lambda^4$ dependence of the Rayleigh scattering.

2. Remote filament-induced breakdown spectroscopy

The ability of the filaments to remotely deliver intensities as high as 50 TW/cm^2 also opens the way to innovative exploration techniques, such as the "remote filament-induced breakdown spectroscopy" (R-FIBS) (Stelmaszczyk *et al.*, 2004). This consists of a combination of Lidar and LIB spectroscopy (LIBS). LIBS

(Cremers and Knight, 2000; Cremers and Radziemski, 2006) is a versatile tool allowing an elemental analysis of surfaces of materials such as metals (Angel *et al.*, 2001), plastics (Jong-Il *et al.*, 2002; Niessner, 1994), minerals (Knight *et al.*, 2000; Sharma *et al.*, 2003; Wiens *et al.*, 2002), aerosols, biological materials (Kyuseok *et al.*, 1997) or liquids as well. It relies on the local ionization of the surface by a strongly focused pulsed laser, typically a Nd:YAG laser. The emission spectrum of the plasma generated at the surface allows a fast analysis, either qualitative or quantitative, with detection limits down to a few parts per million (ppm) for some elements. The use of subpicosecond laser pulses significantly enhances the reproducibility of the measurements, because the lower pulse energy limits the heating of the sample (Albert *et al.*, 2003; Angel *et al.*, 2001; Dou *et al.*, 2003; Rohwetter *et al.*, 2003). The use of broadband detection systems makes LIBS a flexible technique which requires neither preparation of the sample, nor *a priori* knowledge of the elements to be found. Applications such as the identification of highly radioactive nuclear waste or real-time monitoring of melted alloys in industrial processes require a remote analysis technique. LIBS, which is suitable for raw samples, is a good candidate in this regard, since it only requires a direct view to the sample. However, due to the limited size of the optical components, diffraction intrinsically limits the intensity that can be focused on a remote target. On the contrary, self-guided filaments can deliver much higher intensities than the ablation threshold of many species, at distances of hundreds of meters or even kilometers. So, in R-FIBS techniques, the laser-generated filaments are launched on a remote target, and the light emitted by the excited plasma plume is collected through a detection setup comparable to a Lidar-based one (Fig. 36). Although issued from 180 m distances (Stelmaszczyk *et al.*, 2004), the data suggest that measurements can be dimensioned up to the kilometer range (Rohwetter *et al.*, 2003). This technique is currently developed for various applications, e.g., the monitoring of heritage (Tzortzakis *et al.*, 2006) or bacteria (Baudelet *et al.*, 2006; Xu *et al.*, 2006b).

C. Towards a laser lightning rod

Besides remote sensing applications, ultrashort filaments may give access to the control of lightning strikes. Classical techniques to trigger lightning have employed rocket-pulled wires since the 1970's. However, the number of rockets available per storm is necessarily limited and rockets must be launched synchronized with the raise of the ambient electric field. Moreover, the wire falling down may pollute the measurement as well as the environment. Therefore, the idea emerged to apply lasers to control lightning by ionizing the ambient air along the beam and forming a conducting plasma "wire". First attempts used nanosecond pulses (Ball, 1974; Koopman and Wilkerson, 1971; Miki *et al.*,

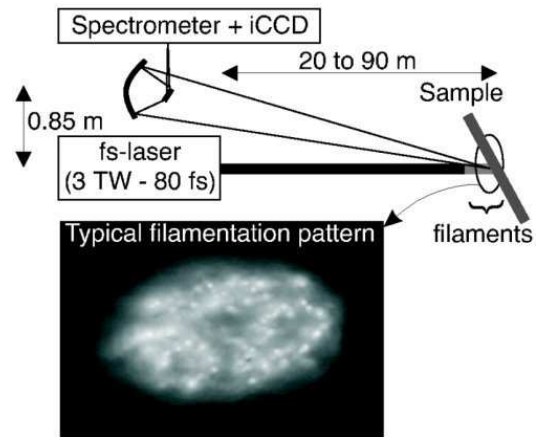


FIG. 36 Principle of Remote filament-induced breakdown spectroscopy (R-FIBS). Bottom: beam profile near to the sample showing multifilamentation with typically 30 filaments across the beam (Stelmaszczyk *et al.*, 2004).

1993). They were unsuccessful, because such lasers could not produce continuously-ionized plasma channels. More recently, this field was renewed by the advent of CPA lasers providing higher intensities in shorter pulses, therefore avoiding laser absorption by inverse bremsstrahlung. Encouraging results have been obtained using focused ultrashort laser pulses to trigger and guide high-voltage discharges over several meters in the laboratory (Comtois *et al.*, 2000; Pépin *et al.*, 2001; Ting *et al.*, 2005a). Others have been obtained on smaller scales using UV ultrashort lasers (Rambo *et al.*, 2001). Since the filaments provide a conducting path over several meters or even longer, they are particularly suitable for the atmosphere. Spectacular experiments with the Teramobile laser installed in a high-voltage facility showed that ultrashort filaments can guide discharges over up to 4.5 m (Ackermann *et al.*, 2006a). Instead of their usual erratic path, discharges are guided along the triggering laser beam (Fig. 37). Moreover, the breakdown voltage is typically reduced by 30% (Rodriguez *et al.*, 2002). Partly guided discharges also occur in sphere-plane gaps, providing valuable information about the mechanism of the initiation and propagation of laser-triggered streamers, with, e.g., plasma lifetimes of about $1\mu\text{s}$ (Ackermann *et al.*, 2006a). Furthermore, an artificial rain does not prevent the laser filaments from triggering such discharges (Ackermann *et al.*, 2004). Current research now focuses on the possibility to extend the plasma lifetime, in order to increase the guiding length and improve scalability to the atmosphere. This approach relies on re-heating and photodetaching electrons of the plasma channel by subsequent pulses, either in the nanosecond (Rambo *et al.*, 2001) or in the femtosecond regime (Hao *et al.*, 2005a). Although high laser powers are usually believed to efficiently detach electrons from O_2^- ions in the plasma, it was recently demonstrated that a subsequent Nd:YAG laser pulse of moderate en-

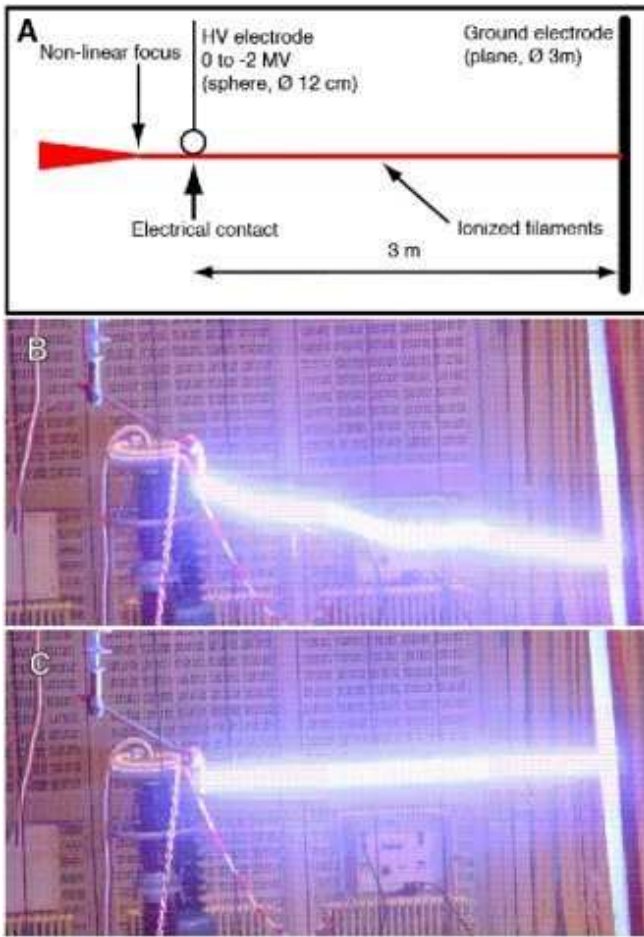


FIG. 37 Laser control of high-voltage discharges. (A) Experimental setup. (B) Free discharge over 3 m, without laser filaments. Note the erratic path. (C) Straight discharge guided along laser filaments (Kasparian *et al.*, 2003).

ergy (sub-Joule) at 532 nm efficiently supports the triggering of discharges by an infrared, femtosecond laser (Méjean *et al.*, 2006a). This effect was interpreted as resulting from a positive retroaction loop where Joule heating of the plasma channel enhances photodetachment, while the resulting higher electron density boosts in turn the Joule effect.

VIII. OUTLOOK

Femtosecond lasers opened up beam parameter ranges from which universal, robust ultrashort filamentary structures conveying high intensities can propagate over long distances in a rich variety of transparent media. These "femtosecond filaments" are characterized by sizes of a few tens up to the hundred of microns and can reach ultrashort FWHM durations down to the optical cycle limit. They design new objects, that can be exploited for delivering few-cycle pulses at very high power levels in the future. Ionization processes do not break this prop-

erty. They even amplify it by cutting the back time slices of the pulse. An accurate control of plasma generation should push the frontiers in nonlinear optics and allow for a precise monitoring of high-order harmonics. The basic scenario of a dynamical balance between Kerr focusing and plasma defocusing explains the existence and the long life of femtosecond filaments in most of propagation configurations. This scenario must, however, be revised at visible wavelengths in condensed materials, in which chromatic dispersion and nonlinear absorption (at high enough power) seem to drive the self-guiding mechanism through an important conical emission managed by X-shaped waveforms in normally dispersive regimes. This aspect requires more investigations. Also, propagation regimes of anomalous dispersion, which promote temporal compression and may further improve self-compression techniques, should be deepened.

In the last years, impressive progresses have been made in the understanding of the nonlinear propagation of high-power laser pulses over long distances in the atmosphere. For broad beams, multiple filamentation becomes more and more controllable by the use of deformable mirrors and genetic algorithms. Besides classical techniques of linear focusing and phase chirping, this will soon enable experimentalists to optimize the propagation range of very powerful pulses. Filaments can therefore be used to remotely deliver high intensities generating *in-situ* nonlinear effects. The spectrum of the white-light continuum is much broader than that expected a few years ago, especially in the ultraviolet where the mixing between the fundamental and third harmonics wavelengths together with the spectral amplification caused by pulse steepening give rise to a spectral plateau extending down to 230 nm. These progresses open the way to applications such as remote sensing of gaseous pollutants and aerosols by Lidar, LIBS analysis of solid samples, or the control of high-voltage electric discharges and lightning strikes. Due to its mobility, the Teramobile allowed to demonstrate the feasibility of many of these techniques. These applications will probably be pushed forward in the future by technological improvements involving more compact systems, diode pumping, as well as spatial and temporal pulse shaping. Novel active media, such as Ytterbium doping or OPCPA, also open the way to new spectral regions, especially the infrared. This spectral region, where eye-safety constraints are easier to fulfill, is nearer the absorption region of many pollutants, such as volatile organic compounds. These more flexible systems will be easier to operate, allowing routine uses for future industrial or atmospheric applications.

Acknowledgments

The Teramobile project is funded by the Centre National de la Recherche Scientifique (CNRS, France) and the Deutsche Forschungsgemeinschaft (DFG, Germany), with contribution by the French and German min-

istries of Foreign Affairs and the Agence Nationale de la Recherche (ANR, France). The authors gratefully acknowledge its team members, formed by the groups of L. Wöste at the Freie Universität Berlin, R. Sauerbrey at the Friedrich Schiller Universität Jena, A. Mysyrowicz at Laboratory for Applied Optics, Palaiseau (France), and the LASIM team led by J.-P. Wolf.

APPENDIX A: Ionization rates for atoms and molecules

This appendix details different photo-ionization theories for gases and dense transparent materials.

1. Ionization in gases

To model the generation of free electrons by an intense light field interacting with a gaseous medium, photo-ionization theories were first developed for atomic systems by Keldysh (Keldysh, 1965), later by Perelomov, Popov and Terent'ev (PPT) (Perelomov *et al.*, 1966, 1967), before being refined by Ammosov, Delone and Krainov (ADK) twenty years after (Ammosov *et al.*, 1986). More recently, Tong *et al.* proposed a theory for molecular species in tunnel ionization regime (Tong *et al.*, 2002).

a. The Keldysh theory

Keldysh's theory is limited to hydrogenoid atoms in their fundamental electronic state and does not consider the Coulomb interaction between the leaving electron and the residual ion. The ionization rate W of an atom irradiated by a laser field $\vec{E}(t) = \vec{E}_p \cos(\omega t)$ is evaluated by

$$W = \frac{q_e^2}{\hbar^2} \lim_{t \rightarrow \infty} \int \frac{d\vec{p}}{(2\pi\hbar)^3} \frac{d}{dt} \left| \int_0^t dt' \cos(\omega t') \right. \\ \left. \times \left\langle \Psi_{\vec{p}}(\vec{r}, t') \middle| \vec{r} \cdot \vec{E}_p \middle| \Psi_g(\vec{r}, t') \right\rangle \right|^2, \quad (\text{A1})$$

where q_e is the electron charge and the ground state of the hydrogenlike atom, characterized by the energy $E_g = -U_i$ (ionization potential), is

$$\Psi_g(\vec{r}, t) = \frac{1}{\sqrt{\pi a^3}} e^{-\frac{r}{a}} e^{-\frac{i}{\hbar} E_g t}. \quad (\text{A2})$$

Here, $a = a_B/Z$ includes the Bohr radius a_B of hydrogen. The continuum electronic states are described with the Volkov functions

$$\Psi_{\vec{p}}(\vec{r}, t) = e^{\frac{i}{\hbar} [(\vec{p} + q_e \vec{A}(t)) \cdot \vec{r} - \frac{1}{2m_e} \int_0^t dt' [\vec{p} + q_e \vec{A}(t')]^2]}, \quad (\text{A3})$$

where $\vec{A}(t)$ is the vector potential of the laser field. Insertion of (A2) and (A3) into Eq. (A1) and integration

over the spatial coordinates result in the expression

$$W = \frac{2}{\hbar^2} \lim_{t \rightarrow \infty} \text{Re} \left[\int \frac{d\vec{p}}{(2\pi\hbar)^3} \right. \\ \left. \times \int_0^t dt' \cos(\omega t) \cos(\omega t') L(\vec{p}, t') L^*(\vec{p}, t) \right], \quad (\text{A4})$$

where $*$ means complex conjugate and

$$L(\vec{p}, t) = V_0 \left[\vec{p} - \frac{q_e}{\omega} \vec{E}_p \sin(\omega t) \right] \\ \times e^{\frac{i}{\hbar} \left\{ U_i t + \frac{1}{2m_e} \int_0^t dt' [\vec{p} - \frac{q_e}{\omega} \vec{E}_p \sin(\omega t')]^2 \right\}}, \quad (\text{A5a})$$

$$V_0(\vec{p}) = -i8q_e \sqrt{\pi a^3} \hbar \vec{E}_p \cdot \vec{\nabla}_{\vec{p}} \left[\frac{1}{(1 + \frac{a^2 p^2}{\hbar^2})^2} \right]. \quad (\text{A5b})$$

The function $L(\vec{p}, t)$ is periodic, with period equal to $T = 2\pi/\omega$. It can then be decomposed into Fourier series. Plugging this series into Eq. (A4) leads to

$$W = \frac{2\pi}{\hbar} \int \frac{d\vec{p}}{(2\pi\hbar)^3} |L(\vec{p})|^2 \\ \times \sum_{n=-\infty}^{+\infty} \delta \left(U_i + \frac{p^2}{2m_e} + \frac{q_e^2 E_p^2}{4m_e \omega^2} - n\hbar\omega \right), \quad (\text{A6})$$

with

$$L(\vec{p}) = 16iq_e \frac{\sqrt{\pi a^7}}{\hbar\pi} U_i^3 \int_{-1}^1 du \frac{\vec{E}_p \cdot \left(\vec{p} - \frac{q_e}{\omega} \vec{E}_p u \right)}{\left[U_i + \frac{1}{2m_e} \left(\vec{p} - \frac{q_e}{\omega} \vec{E}_p u \right)^2 \right]^3} \\ \times e^{\frac{i}{\hbar\omega} \int_0^u \frac{dv}{\sqrt{1-v^2}} \left[U_i + \frac{1}{2m_e} \left(\vec{p} - \frac{q_e}{\omega} \vec{E}_p v \right)^2 \right]}. \quad (\text{A7})$$

Assuming that the electron leaves the atom with a small kinetic energy ($\frac{p^2}{2m_e} \ll U_i$), the poles in the denominator of $L(\vec{p})$ are written as

$$u_s^\pm = i\gamma \left[\pm 1 + i \frac{p \cos(\theta)}{\sqrt{2m_e U_i}} \pm p^2 \frac{\sin^2(\theta)}{2m_e U_i} \right], \quad (\text{A8})$$

where θ is the angle between the impulsion vector \vec{p} and the electric field $\vec{E}(t)$. $\gamma = \omega \sqrt{2m_e U_i} / (|q_e| E_p)$ is the adiabaticity *Keldysh parameter*. It involves the ratio of the ionization potential over the ponderomotive energy $U_p \equiv q_e^2 E_p^2 / 4m_e \omega^2$. By means of the Saddle point method and the residue theorem, Eq. (A7) is next integrated to yield

$$W = 4\sqrt{2}\omega \sqrt{\frac{U_i}{\hbar\omega}} \left[\frac{\gamma}{\sqrt{1+\gamma^2}} \right]^{\frac{3}{2}} \\ \times e^{-\frac{2U_i}{\hbar\omega} \left[\sinh^{-1}(\gamma) - \frac{\gamma\sqrt{1+\gamma^2}}{1+\gamma^2} \right]} S\left(\gamma, \frac{U_i}{\hbar\omega}\right), \quad (\text{A9})$$

where $\tilde{U}_i \equiv U_i + U_p$ and $S(\gamma, x)$ is defined by

$$S(\gamma, x) = \sum_{n=0}^{+\infty} e^{-2 \left[\sinh^{-1}(\gamma) - \frac{\gamma}{\sqrt{1+\gamma^2}} \right] (\langle x+1 \rangle - x+n)} \times \int_0^{\sqrt{\frac{2\gamma}{\sqrt{1+\gamma^2}} (\langle x+1 \rangle - x+n)}} e^{y^2 - \frac{2\gamma}{\sqrt{1+\gamma^2}} (\langle x+1 \rangle - x+n)} dy. \quad (\text{A10})$$

To take electron-ion correlation into account, Keldysh eventually multiplies the ionization rate by the factor $(U_i/\hbar\omega)\gamma/\sqrt{1+\gamma^2}$. Expressed in atomic units (a.u.) $m_e = |q_e| = \hbar = a_B = 1$ (Bransden and Joachain, 2003), the resulting ionization rate expresses

$$W = 2\sqrt{2} \left(\frac{2E_0}{E_p \sqrt{1+\gamma^2}} \right)^{\frac{1}{2}} e^{-2\nu \left[\sinh^{-1}(\gamma) - \frac{\gamma\sqrt{1+\gamma^2}}{1+2\gamma^2} \right]} \times U_i \frac{\gamma^2}{1+\gamma^2} \sum_{\kappa \geq \nu_0}^{+\infty} e^{-\alpha(\kappa-\nu)} \Phi_0(\sqrt{\beta(\kappa-\nu)}), \quad (\text{A11})$$

where $E_0 = (2U_i)^{3/2}$, $\gamma = \omega\sqrt{2U_i}/E_p$, $\nu = \tilde{U}_i/[\hbar\omega]_{\text{a.u.}}$, $\beta = 2\gamma/\sqrt{1+\gamma^2}$, $\alpha = 2 \left[\sinh^{-1}(\gamma) - \gamma/\sqrt{1+\gamma^2} \right]$, $\nu_0 = \langle \nu + 1 \rangle$ and $\Phi_m(x) = e^{-x^2} \int_0^x (x^2 - y^2)^{|m|} e^{y^2} dy$. Equation (A11) differs from the original Keldysh formulation by a factor 4, originating from a corrected version of the residue theorem.

This theory was the first one able to describe atom ionization by an alternating field in low intensity regime ($\gamma \gg 1$) as well as in high intensity regime ($\gamma \ll 1$). The former regime refers to multiphoton ionization (MPI), through which the electron is freed as the atom absorbs $K = \langle U_i/(\hbar\omega) + 1 \rangle$ photons. The latter one corresponds to the tunnel regime, for which the electron leaves the ion by passing through the Coulomb barrier. In MPI regime, the ionization rate is obtained by taking the limit $\gamma \rightarrow +\infty$ in Eq. (A11), which reduces to

$$W = \sigma^{(K)} \times I^K, \quad (\text{A12})$$

where I is the laser intensity and $\sigma^{(K)}$ is the photo-ionization cross-section

$$\sigma^{(K)} = 4\sqrt{2}\omega \left(\frac{U_i}{[\hbar\omega]_{\text{a.u.}}} \right)^{2K+3/2} \times \frac{e^{2K-U_i/[\hbar\omega]_{\text{a.u.}}}}{E_0^{2K}} \Phi_0\left(\sqrt{2K - \frac{2U_i}{[\hbar\omega]_{\text{a.u.}}}}\right), \quad (\text{A13})$$

Expressed in $\text{s}^{-1}\text{cm}^{2K}/\text{W}^K$, the above "cross-section" parameter must be converted as $\sigma^{(K)} \rightarrow \sigma^{(K)}[\text{a.u.}]/[2.42 \times 10^{-17} \times (3.51 \times 10^{16})^K]$.

b. The PPT theory

Later, Perelomov, Popov and Terent'ev (Perelomov *et al.*, 1966, 1967) developed a more

accurate model. First, they included the Coulomb interaction between the ion and the electron, when the latter leaves the atomic core. Second, they considered any atomic bound states as initial. The resulting rate is then

$$W = \frac{4\sqrt{2}}{\pi} |C_{n^*, l^*}|^2 \left(\frac{2E_0}{E_p \sqrt{1+\gamma^2}} \right)^{2n^* - \frac{3}{2} - |m|} \times \frac{f(l, m)}{|m|!} e^{-2\nu \left[\sinh^{-1}(\gamma) - \frac{\gamma\sqrt{1+\gamma^2}}{1+2\gamma^2} \right]} \times U_i \frac{\gamma^2}{1+\gamma^2} \sum_{\kappa \geq \nu_0}^{+\infty} e^{-\alpha(\kappa-\nu)} \Phi_m(\sqrt{\beta(\kappa-\nu)}), \quad (\text{A14})$$

where $n^* = Z/\sqrt{2U_i}$ is the effective quantum number, Z is the residual ion charge, $l^* = n^* - 1$ and n, l, m are the principal quantum number, the orbital momentum and the magnetic quantum number, respectively. The factors $|C_{n^*, l^*}|$ and $f(l, m)$ are

$$|C_{n^*, l^*}|^2 = \frac{2^{2n^*}}{n^* \Gamma(n^* + l^* + 1) \Gamma(n^* - l^*)}, \quad (\text{A15a})$$

$$f(l, m) = \frac{(2l+1)(l+|m|)!}{2^{|m|} |m|! (l-|m|)!}. \quad (\text{A15b})$$

Even if Eq. (A14) is usually presented as the PPT formula, the coefficients $|C_{n^*, l^*}|$ are in fact extracted from the tunneling theory derived by Ammosov, Delone and Krainov (Ammosov *et al.*, 1986). Differences between PPT and ADK coefficients essentially lie in the fact that ADK theory employs electron wavefunctions in a Coulomb potential (Volkov states), which are connected by continuity with the continuum states at large distances ($r \gg 1/\sqrt{2U_i}$).

c. The ADK molecular theory

The PPT rate [Eq. (A14)] holds to describe photo-ionization of atoms. It can lead to some discrepancy when it is applied to molecular systems, because the coefficients $|C_{n^*, l^*}|$, originally evaluated from atomic wavefunctions, cannot reproduce molecular peculiarities, such as, for example, the suppression of ionization observed from the molecule O_2 (DeWitt *et al.*, 2001). To overcome such limitations, we may extend the molecular tunneling theory by Tong *et al.* (Tong *et al.*, 2002) by plugging molecular coefficients into the tunnel limit of the PPT formula and prolonging the latter to low intensity MPI regimes analytically. By doing so, Eq. (A14) is able to describe molecule ionization after the substitution

$$|C_{n^*, l^*}|^2 f(l, m) \rightarrow \left[\sum_l \frac{C_l}{(2U_i)^{(n^*/2)+(1/4)}} \sqrt{\frac{(2l+1)(l+|m|)!}{2^{|m|} |m|! (l-|m|)!}} \right]^2, \quad (\text{A16})$$

where the coefficients C_l have been established for different molecules. For dioxygen, $C_2 = 0.683$ and $C_4 = 0.033$ while $C_1=C_3=0$, and $m = 1$ (Tong *et al.*, 2002).

2. Ionization in dense media

Plasma generation in dense media is described with the ionization rate for crystals developed by Keldysh (Keldysh, 1965). Its analytical evaluation is identical to that applying to atoms, except that the initial states are now modeled by Bloch wave functions. Following similar procedure, the ionization rate for crystals with energy gap E_g irradiated by an electromagnetic field $E_p \cos(\omega t)$ is then

$$W = \frac{2\omega}{9\pi} \left(\frac{\sqrt{1+\gamma^2} m^* \omega}{\gamma \hbar} \right)^{\frac{3}{2}} Q(\gamma, \frac{\tilde{\Delta}}{\hbar\omega}) \times e^{-\pi < \frac{\tilde{\Delta}}{\hbar\omega} + 1 > \times \left[\frac{\tilde{\kappa}(\frac{\gamma^2}{1+\gamma^2}) - \tilde{\varepsilon}(\frac{\gamma^2}{1+\gamma^2})}{\tilde{\varepsilon}(\frac{1}{1+\gamma^2})} \right]} \quad (\text{A17})$$

with $\gamma = \omega \sqrt{m^* E_g} / (|q_e| E_p)$, $m^{*-1} = m_e^{-1} + m_h^{-1}$,

$$\tilde{E}_g = \frac{2}{\pi} E_g \frac{\sqrt{1+\gamma^2}}{\gamma} \tilde{\varepsilon}\left(\frac{1}{1+\gamma^2}\right), \quad (\text{A18a})$$

$$Q(\gamma, x) = \sqrt{\frac{\pi}{2\tilde{\kappa}(\frac{1}{1+\gamma^2})}} \times \sum_{n=0}^{+\infty} e^{-\pi n \left[\frac{\tilde{\kappa}(\frac{\gamma^2}{1+\gamma^2}) - \tilde{\varepsilon}(\frac{\gamma^2}{1+\gamma^2})}{\tilde{\varepsilon}(\frac{1}{1+\gamma^2})} \right]} \times \Phi_0\left(\sqrt{\frac{\pi^2}{4} \frac{2 < x + 1 > - 2x + n}{\tilde{\kappa}(\frac{1}{1+\gamma^2}) \tilde{\varepsilon}(\frac{1}{1+\gamma^2})}}\right). \quad (\text{A18b})$$

Here, the functions $\tilde{\kappa}(x) \equiv \int_0^{\pi/2} (1 - x \sin^2 \theta)^{-1/2} d\theta$ and $\tilde{\varepsilon}(x) \equiv \int_0^{\pi/2} (1 - x \sin^2 \theta)^{1/2} d\theta$ are the complete elliptic integrals of the first and second kind (Abramovitz and Stegun, 1972) and m^* is the reduced mass for the electron/hole pair. The above equation corrects a slip of pen occurring in the original Keldysh's formula. Note that whereas W for gas [Eq. (A11)] is expressed per time unit, W for condensed media [Eq. (A17)] is expressed per time unit and per cubic meter. This ionization rate reduces at low intensities to its multiphoton limit ($\gamma \rightarrow +\infty$) taking the form

$$W = \sigma^{(K)} \times I^K \quad (\text{A19})$$

where

$$\sigma^{(K)} = \frac{2\omega}{9\pi} \left(\frac{m^* \omega}{\hbar} \right)^{\frac{3}{2}} \Phi_0\left(\sqrt{2(K - \frac{E_g}{\hbar\omega})}\right) \times e^{2K} \left(\frac{q_e^2}{8m^* \omega^2 E_g \epsilon_0 c n_0} \right)^K \quad (\text{A20})$$

and $n_0 = n(\omega = \omega_0)$ is the linear refractive index.

APPENDIX B: Atomic dipole for High-Harmonic Generation

The nonlinear polarization vector $\vec{P}_{\text{NL}}(\vec{r}, t)$ used to describe HHG in gases is expressed as

$$\vec{P}_{\text{NL}}(\vec{r}, t) = \rho_{\text{nt}} \vec{d}(\vec{r}, t), \quad (\text{B1})$$

where $\vec{d}(\vec{r}, t)$ is the time-dependent atomic dipole calculated by Lewenstein *et al.* (Lewenstein *et al.*, 1994). For a single electron interacting with a linearly-polarized laser field $\vec{E}(t) = E_p \hat{x} \cos(\omega t)$, the atomic dipole is defined by

$$\vec{d}(\vec{r}, t) = q_e \langle \psi(\vec{r}, t) | \vec{r} | \psi(\vec{r}, t) \rangle. \quad (\text{B2})$$

Solving the time-dependent Schrödinger equation, $\psi(\vec{r}, t)$ denotes the electronic wavefunction

$$|\psi(\vec{r}, t)\rangle = e^{i\frac{U_i t}{\hbar}} \times \left[|0\rangle + \int d^3v b(\vec{v}, t) |v\rangle \right], \quad (\text{B3})$$

where U_i is the ionization potential of the atom, $|0\rangle$ is the ground state and $b(\vec{v}, t)$ is the amplitude of the continuum states $|v\rangle$, respectively. In Eq. (B3), several assumptions have been made, which limits the validity domain of this theory:

- All excited electronic states are ignored, reducing the model to the harmonic production of orders $2K + 1 \geq \frac{U_i}{\hbar\omega}$.
- The depletion of the ground state is neglected such that the ground state amplitude is equal to 1.
- Electrons in the continuum are treated as free particles moving in an oscillating laser field, with no Coulomb potential. This assumption is valid when the ponderomotive energy U_p is higher than the ionization potential.

Inserting (B3) into Eq. (B2), we obtain

$$\vec{d}(t) = i \frac{q_e^2 E_p \hat{x}}{\hbar\omega} \int_0^{\omega t} d(\omega t') \cos(\omega t') \int d^3p d_x^* [\vec{p} + q_e \vec{A}(t)] \times e^{-i\frac{S(\vec{p}, t, t')}{\hbar\omega}} \times d_x [\vec{p} + q_e \vec{A}(t')] + c.c., \quad (\text{B4})$$

where $\vec{d}(\vec{p} + q_e \vec{A}(t))$ is the field-free dipole transition matrix element between the ground state and the continuum state characterized by the momentum $\vec{v} = \vec{p} + q_e \vec{A}(t)$. Here, \vec{p} is the canonical momentum and $\vec{A}(t)$ is the vector potential of the laser field [$\vec{E}(t) = -\partial \vec{A}(t) / \partial t$]. Its formulation for transition from state $|1s\rangle$ is

$$\vec{d}(\vec{p}) = -i\hbar \frac{2^{7/2}}{\pi} (2m_e U_i)^{5/4} \frac{\vec{p}}{(\vec{p}^2 + 2m_e U_i)^3}, \quad (\text{B5})$$

where m_e is the electron mass. $S(\vec{p}, t, t')$ is the quasi-classical action describing the motion of an electron freely moving in the laser field with constant momentum \vec{p} as

$$S(\vec{p}, t, t') = \int_{\omega t'}^{\omega t} \left\{ U_i + \frac{[\vec{p} + q_e \vec{A}(t'')]^2}{2m_e} \right\} d(\omega t''). \quad (\text{B6})$$

The harmonic amplitude \vec{d}_{2K+1} follows from Fourier transforming the time-dependent dipole moment $\vec{d}(t)$

$$\vec{d}_{2K+1} = \frac{1}{T} \int_0^T \vec{d}(t) e^{i(2K+1)\omega t} dt. \quad (\text{B7})$$

For isotropic media, only odd harmonics are produced. The dominant contributions to \vec{d}_{2K+1} comes from the stationary points of the Legendre-transformed quasi-classical action, for which the derivatives of $S(\vec{p}, t, t') - (2K+1)\hbar\omega \times \omega t$ with respect to \vec{p} , t and t' vanish. Introducing the returning time $\tau = t - t'$, the Saddle point

equations read

$$\vec{\nabla}_{\vec{p}} S = \vec{p}_{st} \omega \tau + q_e \int_{\omega(t-\tau)}^{\omega t} \vec{A}(t'') d(\omega t'') = 0 \quad (\text{B8a})$$

$$\frac{\partial S}{\partial(\omega \tau)} = U_i + \frac{[\vec{p}_{st} + q_e \vec{A}(t-\tau)]^2}{2m_e} = 0 \quad (\text{B8b})$$

$$\frac{\partial S}{\partial(\omega t)} = \frac{[\vec{p}_{st} + q_e \vec{A}(t)]^2}{2m_e} - \frac{[\vec{p}_{st} + q_e \vec{A}(t-\tau)]^2}{2m_e} = (2K+1)\hbar\omega \quad (\text{B8c})$$

Equation (B8a) reduces to $\vec{\nabla}_{\vec{p}} S(\vec{p}, t, t') = \vec{x}(t) - \vec{x}(t') = \vec{0}$ where $\vec{x}(t) \equiv \int_0^t v(t') dt'$. This relation imposes that the electron trajectories return at time t to the same point they left at the time t' of ionization. Using Eqs. (B8b) and (B8c) together with the Fourier expansion of $[(\vec{p}_{st} + q_e \vec{A}(t-\tau))^2 / (m_e \hbar \omega) + 2U_i / (\hbar \omega)]^{-3}$ yields the final expression for the Fourier component of the dipole, i.e.,

$$\begin{aligned} \vec{d}_{2K+1} = & -i \frac{q_e \left(\frac{U_p}{\hbar\omega}\right)^{\frac{3}{2}} \frac{32\hbar}{\pi^2} \left(\frac{2U_i}{\hbar\omega}\right)^{\frac{5}{2}}}{(2K+1)^3 \sqrt{m_e \hbar \omega}} \sum_{M=-\infty}^{\infty} \int_0^{+\infty} d\Phi \left[\frac{\pi}{\epsilon + i\frac{\Phi}{2}} \right]^{\frac{3}{2}} b_M(\Phi) e^{-i\frac{F_K(\Phi)}{\hbar\omega}} i^{K-M} \\ & \times \left\{ -B(\Phi) J_{K-M+2} \left[\frac{U_p C(\Phi)}{\hbar\omega} \right] - iB(\Phi) e^{i\Phi} J_{K-M-1} \left(\frac{U_p C(\Phi)}{\hbar\omega} \right) \right. \\ & \left. + i [B(\Phi) e^{i\Phi} + D(\Phi)] J_{K-M+1} \left(\frac{U_p C(\Phi)}{\hbar\omega} \right) + [B(\Phi) + D(\Phi) e^{i\Phi}] J_{K-M} \left(\frac{U_p C(\Phi)}{\hbar\omega} \right) \right\}, \end{aligned} \quad (\text{B9})$$

where $F_K(x) = (U_i + U_p - K\hbar\omega)x - 2U_p[1 - \cos(x)]/x$, $B(x) = -\frac{1}{2} + \sin(x)/x - 2\sin^2(x/2)/x^2$ and $D(x) = -2B(x) - 1 + \cos(x)$. The function $b_M(\Phi)$ has a cumbersome expression, whose analytical methods to compute it can be found in (Antoine *et al.*, 1996).

APPENDIX C: The Teramobile laser

Field experiments are required to characterize the filamentation over long distances as well as to develop atmospheric applications in real scale. Such experiments demand mobility to perform investigations at adequate locations. Studies of high-power fs-laser beam propagation over km-range distances can only be performed outdoors, where relevant aerosol pollutants take place, e.g., in urban areas or at industrial sites. Laser-induced lightning investigations require spots where the lightning probability is high, as well as test experiments at high voltage facilities. These considerations clearly define the need for a mobile fs-TW laser system, embedded in a standard freight container-integrated laboratory equipped with the necessary Lidar detection, power and cooling supplies, temperature stabilization, vibration control, and an addi-

tional standard Lidar system to assure eye safety. These specifications were first achieved by the Teramobile system (Wille *et al.*, 2002). The laser itself is based on a Ti:Sapphire CPA oscillator and a Nd:YAG pumped Ti:Sa amplification chain. It provides 350 mJ pulses with 70 fs duration resulting in a peak power of 5 TW at around 800 nm and with a repetition rate of 10 Hz. Its integration in the reduced space of the mobile laboratory required a particularly compact design (Fig. 38). The classical compressor setup has been improved into a chirp generator to pre-compensate the group velocity dispersion in air. Combined with an adjustable focus, this permits to control the location of the onset of filamentation and its length. Mechanical and thermal stabilities of the mobile laboratory are kept under control, so that the Teramobile can be transported to any place in the world and operated even under adverse weather conditions.

The Teramobile container also includes a Lidar detection chain based on a 40 cm receiving telescope, a high-resolution spectrometer equipped with a set of gratings and detectors allowing simultaneous temporal and spectral analysis of the return signal in a wavelength range comprised between 190 nm and 2.5 μm .

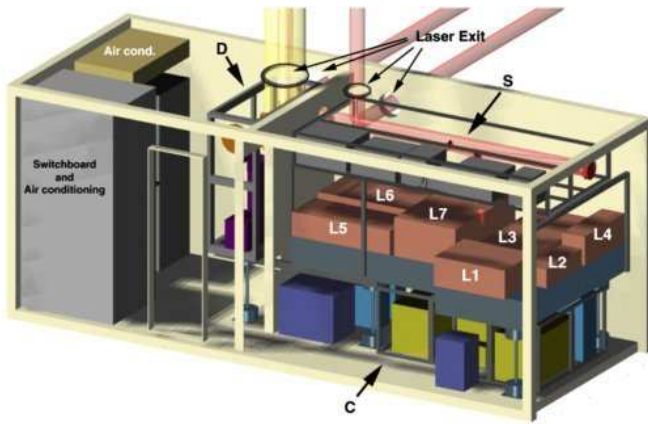


FIG. 38 Three-dimensional view of the Teramobile. (L): Laser system: Ti:Sa oscillator and its Nd:YAG pump laser (L1), stretcher (L2), regenerative amplifier, multipass preamplifier (L3) and their Nd:YAG pump laser (L4); Multipass main amplifier (L5) pumped by two Nd:YAG units (L6); Compressor (L7). (S) Beam expanding system; (C) Power supplies; (D) Lidar detection system.

References

- Abramovitz, M., and I. A. Stegun, 1972, *Handbook of Mathematical Functions* (Dover, New York).
- Ackermann, R., G. Méchain, G. Méjean, R. Bourayou, M. Rodriguez, K. Stelmasczyk, J. Kasparian, J. Yu, E. Salmon, S. Tzortzakis, Y.-B. André, J.-F. Bourrillon, *et al.*, 2006a, *Appl. Phys. B: Lasers & Optics* **82**, 561.
- Ackermann, R., G. Méjean, J. Kasparian, J. Yu, E. Salmon, and J.-P. Wolf, 2006b, *Opt. Lett.* **31**, 86.
- Ackermann, R., K. Stelmasczyk, P. Rohwetter, G. Méjean, E. Salmon, J. Yu, J. Kasparian, G. Méchain, V. Bergmann, S. Schaper, B. Weise, T. Kumm, *et al.*, 2004, *Appl. Phys. Lett.* **85**, 5781.
- Agostini, P., F. Fabre, G. Mainfray, G. Petite, and N. K. Rahman, 1979, *Phys. Rev. Lett.* **42**, 1127.
- Agrawal, G. P., 2001, *Nonlinear Fiber Optics* (Academic Press, San Diego), third edition.
- Akhmediev, N. N., V. I. Korneev, and R. F. Nabiev, 1992, *Opt. Lett.* **17**, 393.
- Aközbek, N., A. Becker, M. Scalora, S. L. Chin, and C. M. Bowden, 2003, *Appl. Phys. B: Lasers & Optics* **77**, 177.
- Aközbek, N., A. Iwasaki, A. Becker, M. Scalora, S. L. Chin, and C. M. Bowden, 2002, *Phys. Rev. Lett.* **89**, 143901.
- Aközbek, N., M. Scalora, C. M. Bowden, , and S. L. Chin, 2001, *Opt. Commun.* **191**, 353.
- Aközbek, N., S. A. Trushin, A. Baltuška, W. Fuss, E. Goulielmakis, K. Kosma, F. Krausz, S. Panja, M. Uiberacker, W. E. Schmid, A. Becker, M. Scalora, *et al.*, 2006, *New J. Phys.* **8**, 177.
- Albert, O., S. Roger, Y. Glinec, J. C. Loulergue, J. Etchepare, C. Boulmer-Leborgne, J. Perière, and E. Millon, 2003, *Appl. Phys. A: Materials Science & Processing* **76**, 319.
- Alexeev, I., A. Ting, D. F. Gordon, E. Briscoe, J. R. Peñano, R. F. Hubbard, and P. Sprangle, 2004, *Appl. Phys. Lett.* **84**, 4080.
- Alexeev, I., A. C. Ting, D. F. Gordon, E. Briscoe, B. Hafizi, and P. Sprangle, 2005, *Opt. Lett.* **30**, 1503.
- Alfano, R. R., and S. L. Shapiro, 1970, *Phys. Rev. Lett.* **24**, 584.
- Amosov, M. V., N. B. Delone, and V. P. Krainov, 1986, *Sov. Phys. JETP* **64**, 1191.
- Anderson, D., 1983, *Phys. Rev. A* **27**, 3135.
- Anderson, D., and M. Bonnedal, 1979, *Phys. Fluids* **22**, 105.
- Anderson, D., M. Bonnedal, and M. Lisak, 1979, *Phys. Fluids* **22**, 1838.
- Anderson, D., and M. Lisak, 1983, *Phys. Rev. A* **27**, 1393.
- Angel, S. M., D. N. Stratis, K. L. Eland, T. Lai, M. A. Berg, and D. M. Gold, 2001, *Fresenius J. Anal. Chem.* **369**, 320.
- Antoine, P., A. L'Huillier, M. Lewenstein, P. Salières, and B. Carré, 1996, *Phys. Rev. A* **53**, 1725.
- Arévalo, E., and A. Becker, 2005, *Phys. Rev. E* **72**, 026605.
- Askar'yan, G. A., 1962, *Sov. Phys. JETP* **15**, 1088.
- Atai, J., Y. Chen, and J. M. Soto-Crespo, 1994, *Phys. Rev. A* **49**, R3170.
- Audebert, P., P. Daguzan, A. Dos Santos, J.-C. Gauthier, J.-P. Geindre, S. Guizard, G. Hamoniaux, K. Krastev, P. Martin, G. Petite, and A. Antonetti, 1994, *Phys. Rev. Lett.* **73**, 1990.
- Augst, S., D. D. Meyerhofer, D. Strickland, and S. L. Chin, 1991, *J. Opt. Soc. Am. B* **8**, 858.
- Backus, S., J. Peatross, Z. Zeek, A. Rundquist, G. Taft, M. M. Murnane, and H. C. Kapteyn, 1996, *Opt. Lett.* **21**, 665.
- Ball, L. M., 1974, *Appl. Opt.* **13**, 2292.
- Baudelet, M., L. Guyon, J. Yu, J.-P. Wolf, T. A. E. Fréjafon, and P. Laloi, 2006, *J. Appl. Phys.* **99**, 084701.
- Becker, A., N. Aközbek, K. Vijayalakshmi, E. Oral, C. M. Bowden, and S. L. Chin, 2001, *Appl. Phys. B: Lasers & Optics* **73**, 287.
- Berezhiani, V. I., V. Skarka, and N. B. Aleksić, 2001, *Phys. Rev. E* **64**, 057601.
- Bergé, L., 1998, *Phys. Rep.* **303**, 259.
- Bergé, L., 2004, *Phys. Rev. E* **69**, 065601(R).
- Bergé, L., and A. Couairon, 2000, *Phys. Plasmas* **7**, 210.
- Bergé, L., and A. Couairon, 2001a, *Phys. Rev. Lett.* **86**, 1003.
- Bergé, L., and A. Couairon, 2001b, *Physica D* **152-153**, 752.
- Bergé, L., K. Germaschewski, R. Grauer, and J. J. Rasmussen, 2002, *Phys. Rev. Lett.* **89**, 153902.
- Bergé, L., C. Gouédard, J. Schjødt-Eriksen, and H. Ward, 2003, *Physica D* **176**, 181.
- Bergé, L., M. R. Schmidt, J. J. Rasmussen, P. L. Christiansen, and K. Ø. Rasmussen, 1997, *J. Opt. Soc. Am. B* **14**, 2550.
- Bergé, L., and S. Skupin, 2005, *Phys. Rev. E* **71**, 065601(R).
- Bergé, L., S. Skupin, F. Lederer, G. Méjean, J. Yu, J. Kasparian, E. Salmon, J. P. Wolf, M. Rodriguez, L. Wöste, R. Bourayou, and R. Sauerbrey, 2004, *Phys. Rev. Lett.* **92**, 225002.
- Bergé, L., S. Skupin, G. Méjean, J. Kasparian, J. Yu, S. Frey, E. Salmon, and J. P. Wolf, 2005, *Phys. Rev. E* **71**, 016602.
- Berkovsky, A. N., S. A. Kozlov, and Y. A. Shpolyanskiy, 2005, *Phys. Rev. A* **72**, 043821.
- Bernstein, A. C., J.-C. Diels, T. S. Luk, T. R. Nelson, A. McPherson, and S. M. Cameron, 2003, *Opt. Lett.* **28**, 2354.
- Bespalov, V. I., and V. I. Talanov, 1966, *JETP Lett.* **3**, 307.
- Bondeson, A., M. Lisak, and D. Anderson, 1979, *Phys. Scr.* **20**, 479.
- Bourayou, R., G. Méjean, J. Kasparian, M. Rodriguez, E. Salmon, J. Yu, H. Lehmann, B. Stecklum, U. Laux, J. Eisloffel, A. Scholz, A. P. Hatzes, *et al.*, 2005, *J. Opt. Soc. Am. B* **22**, 369.
- Boutou, V., C. Favre, S. C. Hill, Y. L. Pan, R. K. Chang, and

- J.-P. Wolf, 2002, *Appl. Phys. B: Lasers & Optics* **75**, 145.
- Boyd, R. W. (ed.), 1992, *Nonlinear Optics* (Academic Press, San Diego).
- Brabec, T., and F. Krausz, 1997, *Phys. Rev. Lett.* **78**, 3282.
- Brabec, T., and F. Krausz, 2000, *Rev. Mod. Phys.* **72**, 545.
- Bransden, B. H., and C. J. Joachain, 2003, *Physics of Atoms and Molecules* (Pearson Education Limited, Prentice Hall).
- Braun, A., G. Korn, X. Liu, D. Du, J. Squier, and G. Mourou, 1995, *Opt. Lett.* **20**, 73.
- Brodeur, A., C. Y. Chien, F. A. Ilkov, S. L. Chin, O. G. Kosareva, and V. P. Kandidov, 1997, *Opt. Lett.* **22**, 304.
- Brodeur, A., and S. L. Chin, 1998, *Phys. Rev. Lett.* **80**, 4406.
- Brodeur, A., and S. L. Chin, 1999, *J. Opt. Soc. Am. B* **16**, 637.
- Buryak, A. V., V. V. Steblina, and R. A. Sammut, 1999, *Opt. Lett.* **24**, 1859.
- Campillo, A. J., S. L. Shapiro, and B. R. Suydam, 1973, *Appl. Phys. Lett.* **23**, 628.
- Campillo, A. J., S. L. Shapiro, and B. R. Suydam, 1974, *Appl. Phys. Lett.* **24**, 178.
- Cerullo, G., A. Dienes, and V. Magni, 1996, *Opt. Lett.* **21**, 65.
- Champeaux, S., and L. Bergé, 2003, *Phys. Rev. E* **68**, 066603.
- Champeaux, S., and L. Bergé, 2005, *Phys. Rev. E* **71**, 046604.
- Champeaux, S., and L. Bergé, 2006, *Opt. Lett.* **31**, 1301.
- Chen, X., Y. Leng, J. Liu, Y. Zhu, R. Li, and Z. Xu, 2006, *Opt. Commun.* **259**, 331.
- Cheng, C.-C., E. M. Wright, and J. V. Moloney, 2001, *Phys. Rev. Lett.* **87**, 213001.
- Cheng, C.-C., E. M. Wright, and J. V. Moloney, 2002, *Phys. Rev. Lett.* **89**, 139302.
- Chernev, P., and V. Petrov, 1992a, *Opt. Lett.* **17**, 172.
- Chernev, P., and V. Petrov, 1992b, *Opt. Commun.* **87**, 28.
- Chiao, R. Y., E. Garmire, and C. H. Townes, 1964, *Phys. Rev. Lett.* **13**, 479.
- Chin, S. L., A. Brodeur, S. Petit, O. G. Kosareva, and V. P. Kandidov, 1999a, *J. Nonlinear Opt. Phys. Mater.* **8**, 121.
- Chin, S. L., S. Petit, F. Borne, and K. Miyazaki, 1999b, *Jpn. J. Appl. Phys.* **38**, L126.
- Chin, S. L., S. Petit, W. Liu, A. Iwasaki, M.-C. Nadeau, V. P. Kandidov, O. G. Kosareva, and K. Y. Andrianov, 2002a, *Opt. Commun.* **210**, 329.
- Chin, S. L., A. Talebpour, J. Yang, S. Petit, V. P. Kandidov, O. G. Kosareva, and M. P. Tamarov, 2002b, *Appl. Phys. B: Lasers & Optics* **74**, 67.
- Chiron, A., B. Lamouroux, R. Lange, J.-F. Ripoché, M. Franco, B. Prade, G. Bonnaud, G. Riazuelo, and A. Mysyrowicz, 1999, *Eur. Phys. J. D* **6**, 383.
- Christodoulides, D. N., N. K. Efremidis, P. Di Trapani, and B. A. Malomed, 2004, *Opt. Lett.* **29**, 1446.
- Comtois, D., C. Y. Chien, A. Desparois, F. Guérin, G. Jarry, T. W. Johnston, J.-C. Kieffer, B. LaFontaine, F. Martin, C. Potvin, A. Bondiou-Clergerie, and I. Gallimberti, 2000, *Appl. Phys. Lett.* **76**, 819.
- Conti, C., S. Trillo, P. Di Trapani, G. Valiulis, A. Piskarskas, O. Jedrkiewicz, and J. Trull, 2003, *Phys. Rev. Lett.* **90**, 170406.
- Cook, K., A. K. Kar, and R. A. Lamb, 2003, *Appl. Phys. Lett.* **83**, 3861.
- Cook, K., R. McGeorge, A. K. Kar, M. R. Taghizadeh, and R. A. Lamb, 2005, *Appl. Phys. Lett.* **86**, 021105.
- Corkum, P. B., 1993, *Phys. Rev. Lett.* **71**, 1994.
- Corkum, P. B., N. H. Burnett, and F. Brunel, 1989, *Phys. Rev. Lett.* **62**, 1259.
- Cornaggia, C., and P. Hering, 2000, *Phys. Rev. A* **62**, 023403.
- Couairon, A., 2003a, *Phys. Rev. A* **68**, 015801.
- Couairon, A., 2003b, *Eur. Phys. J. D* **27**, 159.
- Couairon, A., and L. Bergé, 2002, *Phys. Rev. Lett.* **88**, 135003.
- Couairon, A., J. Biegert, C. P. Hauri, W. Kornelis, F. W. Helbing, U. Keller, and A. Mysyrowicz, 2006, *J. Mod. Opt.* **53**, 75.
- Couairon, A., M. Franco, A. Mysyrowicz, J. Biegert, and U. Keller, 2005, *Opt. Lett.* **30**, 2657.
- Couairon, A., G. Méchain, S. Tzortzakis, M. Franco, B. Lamouroux, B. Prade, and A. Mysyrowicz, 2003, *Opt. Commun.* **225**, 177.
- Couairon, A., S. Tzortzakis, L. Bergé, M. Franco, B. Prade, and A. Mysyrowicz, 2002, *J. Opt. Soc. Am. B* **19**, 1117.
- Courvoisier, F., V. Boutou, J. Kasparian, E. Salmon, G. Méjean, J. Yu, and J. P. Wolf, 2003, *Appl. Phys. Lett.* **83**, 213.
- Cremers, D. A., and A. K. Knight, 2000, *Encyclopedia of Analytical Chemistry*, in (Meyers, 2000), p. 9595.
- Cremers, D. A., and L. J. Radziemski, 2006, *Handbook of Laser-Induced Breakdown measurements* (John Wiley & Sons, Chichester).
- Desaix, M., D. Anderson, and M. Lisak, 1991, *J. Opt. Soc. Am. B* **8**, 2082.
- Desyatnikov, A., A. Maimistov, and B. Malomed, 2000, *Phys. Rev. E* **61**, 3107.
- Desyatnikov, A., L. Torner, and Y. S. Kivshar, 2005, *Prog. in Opt.* **47**, 291.
- DeWitt, M. J., E. Wells, and R. R. Jones, 2001, *Phys. Rev. Lett.* **87**, 153001.
- Di Trapani, P., G. Valiulis, A. Piskarskas, O. Jedrkiewicz, J. Trull, C. Conti, and S. Trillo, 2003, *Phys. Rev. Lett.* **91**, 093904.
- Donnat, P., C. Gouedard, D. Veron, O. Bonville, C. Sauteret, and A. Migus, 1992, *Opt. Lett.* **17**, 331.
- Dou, K., E. T. Knobbe, R. L. Parkhill, B. Irwin, L. Matthews, and K. H. Church, 2003, *Appl. Phys. A: Materials Science & Processing* **76**, 303.
- Drescher, M., M. Hentschel, R. Kienberger, G. Tempea, C. Spielmann, G. A. Reider, P. B. Corkum, and F. Krausz, 2001, *Science* **291**, 1923.
- Du, D., X. Liu, G. Korn, J. Squier, and G. Mourou, 1994, *Appl. Phys. Lett.* **64**, 3071.
- Dubietis, A., E. Gaižauskas, G. Tamošauskas, and P. Di Trapani, 2004a, *Phys. Rev. Lett.* **92**, 253903.
- Dubietis, A., E. Kučinska, G. Tamošauskas, E. Gaižauskas, M. A. Porras, and P. Di Trapani, 2004b, *Opt. Lett.* **29**, 2893.
- Dubietis, A., G. Tamošauskas, I. Diomin, and A. Varavičius, 2003, *Opt. Lett.* **28**, 1269.
- Dubietis, A., G. Tamošauskas, G. Fibich, and B. Ilan, 2004c, *Opt. Lett.* **29**, 1126.
- Esarey, E., P. Sprangle, J. Krall, and A. Ting, 1997, *IEEE J. Quant. Electron.* **33**, 1879.
- Favre, C., V. Boutou, S. C. Hill, W. Zimmer, M. Krenz, H. Lambrecht, J. Yu, R. K. Chang, L. Woeste, and J.-P. Wolf, 2002, *Phys. Rev. Lett.* **89**, 035002.
- Feit, M. D., and J. A. Fleck, 1974, *Appl. Phys. Lett.* **24**, 169.
- Feit, M. D., and J. A. Fleck, 1988, *J. Opt. Soc. Am. B* **5**, 633.
- Feng, Q., J. V. Moloney, A. C. Newell, and E. M. Wright, 1995, *Opt. Lett.* **20**, 1958.
- Feng, Q., J. V. Moloney, A. C. Newell, E. M. Wright, K. Cook, P. K. Kennedy, D. X. Hammer, B. A. Rockwell, and C. R.

- Thompson, 1997, *IEEE J. Quant. Electron.* **33**, 127.
- Fibich, G., 1996, *Phys. Rev. Lett.* **76**, 4356.
- Fibich, G., S. Eisenmann, B. Ilan, Y. Erlich, M. Fraenkel, Z. Henis, A. L. Gaeta, and A. Zigler, 2005, *Opt. Express* **13**, 5897.
- Fibich, G., S. Eisenmann, B. Ilan, and A. Zigler, 2004, *Opt. Lett.* **29**, 1772.
- Fibich, G., and B. Ilan, 2001a, *Opt. Lett.* **26**, 840.
- Fibich, G., and B. Ilan, 2001b, *Physica D* **157**, 112.
- Fibich, G., and B. Ilan, 2004, *Opt. Lett.* **29**, 887.
- Fibich, G., B. Ilan, and S. Tsynkov, 2002, *J. Scien. Comput.* **17**, 351.
- Fibich, G., and G. Papanicolaou, 1999, *SIAM J. Appl. Math.* **60**, 183.
- Fibich, G., and G. C. Papanicolaou, 1997, *Opt. Lett.* **22**, 1379.
- Fibich, G., W. Ren, and X.-P. Wang, 2003, *Phys. Rev. E* **67**, 056603.
- Fibich, G., Y. Sivan, Y. Ehrlich, E. Louzon, M. Fraenkel, S. Eisenmann, Y. Katzir, and A. Ziegler, 2006, *Opt. Express* **14**, 4946.
- Firth, W. J., and D. V. Skryabin, 1997, *Phys. Rev. Lett.* **79**, 2450.
- Fraïman, G. M., 1985, *Sov. Phys. JETP* **61**, 228.
- Fujii, T., and T. Fukuchi (eds.), 2005, *Femtosecond white-light lidar* (Marcel Dekker, Inc., New York).
- Gaeta, A. L., 2000, *Phys. Rev. Lett.* **84**, 3582.
- Gaeta, A. L., and F. Wise, 2001, *Phys. Rev. Lett.* **87**, 229401.
- Gatz, S., and J. Herrmann, 1997, *J. Opt. Soc. Am. B* **14**, 1795.
- Geissler, M., G. Tempea, A. Scrinzi, M. Schnürer, F. Krausz, and T. Brabec, 1999, *Phys. Rev. Lett.* **83**, 2930.
- Germaschewski, K., R. Grauer, L. Bergé, V. K. Mezentsev, and J. J. Rasmussen, 2001, *Physica D* **151**, 175.
- Gil'denburg, V. B., V. I. Pozdnyakova, and I. A. Shereshevskii, 1995, *Phys. Lett. A* **203**, 214.
- Glasse, R. T., 1977, *J. Math. Phys.* **18**, 1794.
- Golubtsov, I. S., V. P. Kandidov, and O. G. Kosareva, 2003, *Quant. Electron.* **33**, 525.
- Gong, Q.-H., J.-L. Li, T.-Q. Zhang, and H. Yang, 1998, *Chin. Phys. Lett.* **15**, 30.
- Gordon, D. F., A. C. Ting, I. Alexeev, R. P. Fischer, and P. Sprangle, 2006, *IEEE Trans. Plasma Sc.* **34**, 249.
- Grow, T. D., and A. L. Gaeta, 2005, *Opt. Express* **13**, 4594.
- Guyon, L., F. Courvoisier, V. Boutou, R. Nuter, A. Vinçotte, S. Champeaux, L. Bergé, P. Glorieux, and J.-P. Wolf, 2006, *Phys. Rev. A* **73**, 051802(R).
- Hao, Z., J. Zhang, Y. T. Li, X. Lu, X. H. Yuan, Z. Y. Zheng, Z. H. Wang, W. J. Ling, and Z. Y. Wei, 2005a, *Appl. Phys. B: Lasers & Optics* **80**, 627.
- Hao, Z.-Q., J. Yu, J. Zhang, Y.-T. Li, X.-H. Yuan, Z.-Y. Zheng, P. Wang, Z.-H. Wang, W.-J. Ling, and Z.-Y. Wei, 2005b, *Chin. Phys. Lett.* **22**, 636.
- Hauri, C. P., W. Kornelis, F. W. Helbing, A. Heinrich, A. Couairon, A. Mysyrowicz, J. Biegert, and U. Keller, 2004, *Appl. Phys. B: Lasers & Optics* **79**, 673.
- He, G. S., and S. H. Liu, 1999, *Physics of Nonlinear Optics* (World Scientific, Singapore).
- Heck, G., J. Sloss, and R. J. Levis, 2006, *Opt. Commun.* **259**, 216.
- Hellwarth, R. W., D. M. Pennington, and M. A. Henesian, 1990, *Phys. Rev. A* **41**, 2766.
- Henz, S., and J. Herrmann, 1999, *Phys. Rev. A* **59**, 2528.
- Homoelle, D., and A. L. Gaeta, 2000, *Opt. Lett.* **25**, 761.
- Hosseini, S. A., Q. Luo, B. Ferland, W. Liu, S. L. Chin, O. G. Kosareva, N. A. Panov, N. Aközbe, and V. P. Kandidov, 2004a, *Phys. Rev. A* **70**, 033802.
- Hosseini, S. A., J. Yu, Q. Luo, and S. L. Chin, 2004b, *Appl. Phys. B: Lasers & Optics* **79**, 519.
- Husakou, A. V., and J. Herrmann, 2001, *Phys. Rev. Lett.* **87**, 203901.
- Jin, Z., J. Zhang, M. H. Xu, X. Lu, Y. T. Li, Z. H. Wang, Z. Y. Wei, X. H. Yuan, and W. Yu, 2005, *Opt. Express* **13**, 10424.
- Jong-Il, Y., R. Klenze, and J. I. Kim, 2002, *Appl. Spectroscopy* **56**, 852.
- Kandidov, V. P., N. Aközbe, M. Scalora, O. G. Kosareva, A. V. Nyakk, Q. Luo, S. A. Hosseini, and S. L. Chin, 2005, *Appl. Phys. B: Lasers & Optics* **80**, 267.
- Kandidov, V. P., I. S. Golubtsov, and O. G. Kosareva, 2004, *Quant. Electron.* **34**, 348.
- Kandidov, V. P., O. G. Kosareva, I. S. Golubtsov, W. Liu, A. Becker, N. Aközbeck, C. M. Bowden, and S. L. Chin, 2003, *Appl. Phys. B: Lasers & Optics* **77**, 149.
- Kandidov, V. P., O. G. Kosareva, and S. A. Shlenov, 1994, *Quant. Electron.* **24**, 905.
- Kandidov, V. P., O. G. Kosareva, M. P. Tamarov, A. Brodeur, and S. L. Chin, 1999, *Quant. Electron.* **29**, 911.
- Karlsson, M., D. Anderson, and M. Desaix, 1992, *Opt. Lett.* **17**, 22.
- Kasparian, J., M. Rodriguez, G. Méjean, J. Yu, E. Salmon, H. Wille, R. Bourayou, S. Frey, Y. B. André, A. Mysyrowicz, R. Sauerbrey, J. P. Wolf, *et al.*, 2003, *Science* **301**, 61.
- Kasparian, J., R. Sauerbrey, and S. L. Chin, 2000a, *Appl. Phys. B: Lasers & Optics* **71**, 877.
- Kasparian, J., R. Sauerbrey, D. Mondelain, S. Niedermeier, J. Yu, J. P. Wolf, Y. B. André, M. Franco, B. Prade, S. Tzortzakis, A. Mysyrowicz, M. Rodriguez, *et al.*, 2000b, *Opt. Lett.* **25**, 1397.
- Kath, W. L., and N. F. Smyth, 1995, *Phys. Rev. E* **51**, 1484.
- Keldysh, L. V., 1965, *Sov. Phys. JETP* **20**, 1307.
- Kelley, P. L., 1965, *Phys. Rev. Lett.* **15**, 1005.
- Kennedy, P. K., 1995, *IEEE J. Quant. Electron.* **31**, 2241.
- Knight, A. K., N. L. Scherbarth, D. A. Cremers, and M. J. Ferris, 2000, *Appl. Spectroscopy* **54**, 331.
- Kolesik, M., G. Katona, J. V. Moloney, and E. M. Wright, 2003a, *Phys. Rev. Lett.* **91**, 043905.
- Kolesik, M., G. Katona, J. V. Moloney, and E. M. Wright, 2003b, *Appl. Phys. B: Lasers & Optics* **77**, 185.
- Kolesik, M., and J. V. Moloney, 2004a, *Phys. Rev. E* **70**, 036604.
- Kolesik, M., and J. V. Moloney, 2004b, *Opt. Lett.* **29**, 590.
- Kolesik, M., J. V. Moloney, and M. Mlejnek, 2002, *Phys. Rev. Lett.* **89**, 283902.
- Kolesik, M., J. V. Moloney, and E. M. Wright, 2001, *Phys. Rev. E* **64**, 046607.
- Kolokolov, A. A., 1976, *Radiophys. Quant. Electron.* **17**, 1016.
- Konno, K., and H. Suzuki, 1979, *Phys. Scr.* **20**, 382.
- Koopman, D. W., and T. D. Wilkerson, 1971, *J. Appl. Phys.* **42**, 1883.
- Koprinkov, I. G., A. Suda, P. Wang, and K. Midorikawa, 2000, *Phys. Rev. Lett.* **84**, 3847.
- Koprinkov, I. G., A. Suda, P. Wang, and K. Midorikawa, 2001, *Phys. Rev. Lett.* **87**, 229402.
- Kosareva, O., V. P. Kandidov, A. Brodeur, C. Y. Chien, and S. L. Chin, 1997, *Opt. Lett.* **22**, 1332.
- Kosmatov, N. E., V. F. Shvets, and V. E. Zakharov, 1991,

- Physica D **52**, 16.
- Krainov, V. P., 1997, J. Opt. Soc. Am. B **14**, 425.
- Kruglov, V. I., Y. A. Logvin, and V. M. Volkov, 1992, J. Mod. Opt. **39**, 2277.
- Kruglov, V. I., and R. A. Vlasov, 1985, Phys. Lett. **111A**, 401.
- Kuznetsov, E. A., 1996, CHAOS **6**, 381.
- Kuznetsov, E. A., J. J. Rasmussen, K. Rypdal, and S. K. Turitsyn, 1995, Physica D **87**, 273.
- Kuznetsov, E. A., A. M. Rubenchik, and V. E. Zakharov, 1986, Phys. Rep. **142**, 103.
- Kyuseok, S., L. Yong-Ill, and J. Sneddon, 1997, Appl. Spectroscopy Reviews **32**, 183.
- Labauve, C., S. Baton, T. Jalinaud, H. A. Baldis, and D. Pesme, 1992, Phys. Fluids B **4**, 2224.
- LaFontaine, B., F. Vidal, D. Comtois, C.-Y. Chien, A. Desparois, T.-W. Johnston, J.-C. Kieffer, H.-P. Mercure, H. Pépin, and F. A. M. Rizk, 1999a, IEEE Trans. Plasma Sc. **27**, 688.
- LaFontaine, B., F. Vidal, Z. Jiang, C. Y. Chien, D. Comtois, A. Desparois, T. W. Johnston, J. C. Kieffer, H. Pépin, and H. P. Mercure, 1999b, Phys. Plasmas **6**, 1615.
- Landman, M. J., G. C. Papanicolaou, C. Sulem, and P. L. Sulem, 1988, Phys. Rev. A **38**, 3837.
- Lange, H. R., A. Chiron, J.-F. Ripoche, A. Mysyrowicz, P. Breger, and P. Agostini, 1998a, Phys. Rev. Lett. **81**, 1611.
- Lange, H. R., G. Grillon, J.-F. Ripoche, M. A. Franco, B. Lamouroux, B. S. Prade, A. Mysyrowicz, E. T. J. Nibbering, and A. Chiron, 1998b, Opt. Lett. **23**, 120.
- Lehmeier, H. J., W. Leupacher, and A. Penzkofer, 1985, Opt. Commun. **56**, 67.
- Lehner, T., and N. Aubry, 2000, Phys. Rev. E **61**, 1996.
- leMesurier, B. J., 2000, Physica D **138**, 334.
- leMesurier, B. J., P. L. Christiansen, Y. B. Gaididei, and J. J. Rasmussen, 2004, Phys. Rev. E **70**, 046614.
- Lenzner, M., J. Krüger, S. Sartania, Z. Cheng, C. Spielmann, G. Mourou, W. Kautek, and F. Krausz, 1998, Phys. Rev. Lett. **80**, 4076.
- Lewenstein, M., P. Balcou, M. Y. Ivanov, A. L'Huillier, and P. B. Corkum, 1994, Phys. Rev. A **49**, 2117.
- Li, M., S. Menon, J. P. Nibarger, and G. N. Gibson, 1999, Phys. Rev. Lett. **82**, 2394.
- Litvak, A. G., V. A. Mironov, and E. M. Sher, 2000a, J. Exp. Theor. Phys. **91**, 1268.
- Litvak, A. G., V. A. Mironov, and E. M. Sher, 2000b, Phys. Rev. E **61**, 891.
- Liu, J., H. Schroeder, S. L. Chin, R. Li, and Z. Xu, 2005a, Opt. Express **13**, 10248.
- Liu, J., H. Schroeder, S. L. Chin, R. Li, W. Yu, and Z. Xu, 2005b, Phys. Rev. A **72**, 053817.
- Liu, W., and S. L. Chin, 2005, Opt. Express **13**, 5750.
- Liu, W., S. L. Chin, O. Kosareva, I. S. Golubtsov, and V. P. Kandidov, 2003, Opt. Commun. **225**, 193.
- Liu, W., S. A. Hosseini, Q. Luo, B. Ferland, S. L. Chin, O. G. Kosareva, N. A. Panov, and V. P. Kandidov, 2004, New J. Phys. **6**, 1.
- Liu, W., O. Kosareva, I. S. Golubtsov, A. Iwasaki, A. Becker, V. P. Kandidov, and S. L. Chin, 2002, Appl. Phys. B: Lasers & Optics **75**, 595.
- Liu, W., F. Théberge, E. Arevalo, J.-F. Gravel, A. Becker, and S. L. Chin, 2005c, Opt. Lett. **30**, 2602.
- Liu, W., F. Théberge, J.-F. Daigle, P. T. Simard, S. M. Sarifi, Y. Kamali, H. L. Xu, and S. L. Chin, 2006, Appl. Phys. B: Lasers & Optics **85**, 55.
- Lotz, W., 1967a, Zeitschrift Phys. **206**, 205.
- Lotz, W., 1967b, J. Opt. Soc. Am. B **57**, 873.
- Lugovoi, V. N., and A. M. Prokhorov, 1974, Sov. Phys. Usp. **16**, 658.
- Luo, Y., H. Ågren, B. Minaev, and P. Jørgensen, 1995, J. Mol. Struct. **336**, 61.
- Luther, G. G., J. V. Moloney, A. C. Newell, and E. M. Wright, 1994a, Opt. Lett. **19**, 862.
- Luther, G. G., A. C. Newell, and J. V. Moloney, 1994b, Physica D **74**, 59.
- Mairesse, Y., A. de Bohan, L. J. Frasinski, H. Merdji, L. C. Dinu, P. Monchicourt, P. Breger, M. Kovačev, R. Taïeb, B. Carré, H. G. Muller, P. Agostini, *et al.*, 2003, Science **302**, 1540.
- Malkin, V. M., 1990, Phys. Lett. A **151**, 285.
- Malkin, V. M., 1993, Physica D **64**, 251.
- Manassah, J. T., 1992, Opt. Lett. **17**, 1259.
- Manassah, J. T., P. L. Baldeck, and R. R. Alfano, 1988, Opt. Lett. **13**, 589.
- Marburger, J. H., 1975, Prog. Quantum Electron. **4**, 35.
- Mariyenko, I. G., J. Strohaber, and C. J. G. J. Uiterwaal, 2005, Opt. Express **13**, 7599.
- Marklund, M., and P. K. Shukla, 2006, Opt. Lett. **31**, 1884.
- Martin, P., S. Guizard, P. Daguzan, G. Petite, P. D'Oliveira, P. Meynadier, and M. Perdrix, 1997, Phys. Rev. B **55**, 5799.
- McKinstrie, C. J., and D. A. Russell, 1988, Phys. Rev. Lett. **61**, 2929.
- Measures, R. M., 1984, *Laser remote sensing - Fundamentals and applications* (Wiley Interscience, New York).
- Méchain, G., A. Couairon, M. Franco, B. Prade, and A. Mysyrowicz, 2004, Phys. Rev. Lett. **93**, 035003.
- Méchain, G., C. D'Amico, Y.-B. André, S. Tzortzakis, M. Franco, B. Prade, A. Mysyrowicz, A. Couairon, E. Salmon, and R. Sauerbrey, 2005a, Opt. Commun. **247**, 171.
- Méchain, G., G. Méjean, R. Ackermann, P. Rohwetter, Y.-B. André, J. Kasparian, B. Prade, K. Stelmaszczyk, J. Yu, E. Salmon, W. Winn, L. A. V. Schlie, *et al.*, 2005b, Appl. Phys. B: Lasers & Optics **80**, 785.
- Méjean, G., R. Ackermann, J. Kasparian, E. Salmon, J. Yu, J.-P. Wolf, K. Rethmeier, W. Kalkner, P. Rohwetter, K. Stelmaszczyk, and L. Wöste, 2006a, Appl. Phys. Lett. **88**, 021101.
- Méjean, G., J. Kasparian, J. Yu, S. Frey, E. Salmon, R. Ackermann, J.-P. Wolf, L. Bergé, and S. Skupin, 2006b, Appl. Phys. B: Lasers & Optics **82**, 341.
- Méjean, G., J. Kasparian, J. Yu, S. Frey, E. Salmon, and J. P. Wolf, 2004, Appl. Phys. B: Lasers & Optics **78**, 535.
- Méjean, G., J. Kasparian, J. Yu, E. Salmon, S. Frey, J.-P. Wolf, S. Skupin, A. Vinçotte, R. Nuter, S. Champeaux, and L. Bergé, 2005, Phys. Rev. E **72**, 026611.
- Mével, E., O. Tcherbakoff, F. Salin, and E. Constant, 2003, J. Opt. Soc. Am. B **20**, 105.
- Meyers, R. A., 2000, *Encyclopedia of Analytical Chemistry* (John Wiley & Sons, Chichester).
- Michinel, H., J. Campo-Táboas, M. L. Quiroga-Teixeiro, J. R. Sagueiro, and R. García-Fernández, 2001, J. Opt. B: Quantum Semiclass. Opt. **3**, 314.
- Miki, M., Y. Aihara, and T. Shindo, 1993, J. Phys. D: Appl. Phys. **26**, 1244.
- Milsted Jr., C. S., and C. D. Cantrell, 1996, Phys. Rev. A **53**, 3536.
- Mlejnek, M., M. Kolesik, J. V. Moloney, and E. M. Wright,

- 1999, Phys. Rev. Lett. **83**, 2938.
- Mlejnek, M., E. M. Wright, and J. V. Moloney, 1998a, Opt. Lett. **23**, 382.
- Mlejnek, M., E. M. Wright, and J. V. Moloney, 1998b, Phys. Rev. E **58**, 4903.
- Moll, K. D., and A. L. Gaeta, 2004, Opt. Lett. **29**, 995.
- Moll, K. D., A. L. Gaeta, and G. Fibich, 2003, Phys. Rev. Lett. **90**, 203902.
- Mourou, G., T. Tajima, and S. V. Bulanov, 2006, Rev. Mod. Phys. **78**, 309.
- Nibbering, E. T. J., P. F. Curley, G. Grillon, B. S. Prade, M. A. Franco, F. Salin, and A. Mysyrowicz, 1996, Opt. Lett. **21**, 62.
- Nibbering, E. T. J., G. Grillon, M. A. Franco, B. S. Prade, and A. Mysyrowicz, 1997, J. Opt. Soc. Am. B **14**, 650.
- Niessner, R., 1994, Proceedings of the SPIE **2360**, 254.
- Nishioka, H., W. Odajima, K. Ueda, and H. Takuma, 1995, Opt. Lett. **20**, 2505.
- Nisoli, M., S. De Silvestri, O. Svelto, R. Szpöcs, K. Ferencz, C. Spielmann, S. Sartania, and F. Krausz, 1997a, Opt. Lett. **22**, 522.
- Nisoli, M., S. Stagira, S. D. Silvestri, O. Svelto, S. Sartania, Z. Cheng, M. Lenzner, C. Spielmann, and F. Krausz, 1997b, Appl. Phys. B: Lasers & Optics **65**, 189.
- Nisoli, M., S. Stagira, S. D. Silvestri, O. Svelto, S. Sartania, Z. Cheng, G. Tempea, C. Spielmann, and F. Krausz, 1998, IEEE J. Selec. Top. Quant. Electron. **4**, 414.
- Noack, J., and A. Vogel, 1999, IEEE J. Quant. Electron. **35**, 1156.
- Nurhuda, M., A. Suda, M. Hatayama, K. Nagasaka, and K. Midorikawa, 2002a, Phys. Rev. A **66**, 023811.
- Nurhuda, M., A. Suda, and K. Midorikawa, 2002b, RIKEN Rev. **48**, 40.
- Nuter, R., and L. Bergé, 2006, J. Opt. Soc. Am. B **23**, 874.
- Nuter, R., S. Skupin, and L. Bergé, 2005, Opt. Lett. **30**, 917.
- Pan, L., K. T. Taylor, and C. W. Clark, 1990, J. Opt. Soc. Am. B **7**, 509.
- Peck, E. R., and K. Reeder, 1972, J. Opt. Soc. Am. **62**, 958.
- Peñano, J. R., P. Sprangle, B. Hafizi, W. Manheimer, and A. Zigler, 2005, Phys. Rev. E **72**, 036412.
- Peñano, J. R., P. Sprangle, B. Hafizi, A. Ting, D. F. Gordon, and C. A. Kapetanakis, 2004, Phys. Plasmas **11**, 2865.
- Peñano, J. R., P. Sprangle, P. Serafim, B. Hafizi, and A. Ting, 2003, Phys. Rev. E **68**, 056502.
- Penetrante, B. M., J. N. Bardsley, W. M. Wood, C. W. Siders, and M. C. Downer, 1992, J. Opt. Soc. Am. B **9**, 2032.
- Pépin, H., D. Comtois, F. Vidal, C. Y. Chien, A. Desparois, T. W. Johnston, J.-C. Kieffer, B. LaFontaine, F. Martin, F. A. M. Rizk, C. Potvin, P. Couture, *et al.*, 2001, Phys. Plasmas **8**, 2532.
- Perelomov, A. M., and V. S. Popov, 1967, Sov. Phys. JETP **25**, 336.
- Perelomov, A. M., V. S. Popov, and M. V. Terent'ev, 1966, Sov. Phys. JETP **23**, 924.
- Perelomov, A. M., V. S. Popov, and M. V. Terent'ev, 1967, Sov. Phys. JETP **24**, 207.
- Perry, M. D., O. L. Landen, A. Szöke, and E. M. Campbell, 1988a, Phys. Rev. A **37**, 747.
- Perry, M. D., A. Szöke, O. L. Landen, and E. M. Campbell, 1988b, Phys. Rev. Lett. **60**, 1270.
- Petit, S., A. Talebpour, A. Proulx, and S. L. Chin, 2000, Opt. Commun. **175**, 323.
- Petrov, D. V., L. Torner, J. Martorell, R. Vilaseca, J. P. Torres, and C. Cojocar, 1998, Opt. Lett. **23**, 1444.
- Pfeifer, T., C. Spielmann, and G. Gerber, 2006, Rep. Prog. Phys. **69**, 443.
- Pietsch, H., R. Blaha, E. W. Laedke, and A. Kumar, 1991, Europhys. Lett. **15**, 173.
- Porras, M. A., A. Parola, D. Faccio, A. Dubietis, and P. Di Trapani, 2004, Phys. Rev. Lett. **93**, 153902.
- Quigora-Teixeiro, M., and H. Michinel, 1997, J. Opt. Soc. Am. B **14**, 2004.
- Rae, S. C., and K. Burnett, 1992, Phys. Rev. A **46**, 1084.
- Rairoux, P., H. Schillinger, S. Niedermeier, M. Rodriguez, F. Ronneberger, R. Sauerbrey, B. Stein, D. Waite, C. Wedekind, H. Wille, L. Wöste, and C. Ziener, 2000, Appl. Phys. B: Lasers & Optics **71**, 573.
- Rambo, P., J. Schwartz, and J.-C. Diels, 2001, J. Opt. A: Pure Appl. Opt. **3**, 146.
- Ranka, J. K., and A. L. Gaeta, 1998, Opt. Lett. **23**, 534.
- Rasmussen, J. J., and K. Rypdal, 1986, Phys. Scr. **33**, 481.
- Rayner, D. M., A. Naumov, and P. B. Corkum, 2005, Opt. Express **13**, 3208.
- Reiss, H. R., 1980, Phys. Rev. A **22**, 1786.
- Ripoche, J. F., G. Grillon, B. Prade, M. Franco, E. Nibbering, R. Lange, and A. Mysyrowicz, 1997, Opt. Commun. **135**, 310.
- Rodriguez, M., R. Bourayou, G. Méjean, J. Kasparian, J. Yu, E. Salmon, A. Scholz, B. Stecklum, J. Eislöffel, U. Laux, A. P. Hatzes, R. Sauerbrey, *et al.*, 2004, Phys. Rev. E **69**, 036607.
- Rodriguez, M., R. Sauerbrey, H. Wille, L. Wöste, T. Fujii, Y.-B. André, A. Mysyrowicz, L. Klingbeil, K. Rethmeier, W. Kalkner, J. Kasparian, E. Salmon, *et al.*, 2002, Opt. Lett. **27**, 772.
- Rohwetter, P., K. Stelmaszczyk, G. Méjean, J. Yu, E. Salmon, J. Kasparian, J.-P. Wolf, and L. Wöste, 2003, J. Anal. Atom. Spectroscopy **19**, 437.
- Rothenberg, J. E., 1992, Opt. Lett. **17**, 1340.
- Rypdal, K., and J. J. Rasmussen, 1989, Phys. Scr. **40**, 192.
- Rypdal, K., J. J. Rasmussen, and K. Thomsen, 1985, Physica D **16**, 339.
- Salières, P., and M. Lewenstein, 2001, Meas. Sci. Technol. **12**, 1818.
- Schjodt-Eriksen, J., Y. B. Gaididei, and P. L. Christiansen, 2001a, Phys. Rev. E **64**, 066614.
- Schjodt-Eriksen, J., J. V. Moloney, E. M. Wright, Q. Feng, and P. L. Christiansen, 2001b, Opt. Lett. **26**, 78.
- Schroeder, H., and S. L. Chin, 2004, Opt. Commun. **234**, 399.
- Schroeder, H., J. Liu, and S. L. Chin, 2004, Opt. Express **12**, 4768.
- Schwarz, J., P. Rambo, and J.-C. Diels, 2001, Appl. Phys. B: Lasers & Optics **72**, 343.
- Schwarz, J., P. Rambo, J.-C. Diels, M. Kolesik, E. M. Wright, and J. V. Moloney, 2000, Opt. Commun. **180**, 383.
- Scrinzi, A., M. Y. Ivanov, R. Kienberger, and D. M. Villeneuve, 2006, J. Phys. B: At. Mol. Opt. Phys. **39**, 1.
- Sharma, S. K., P. G. Lucey, M. Ghosh, H. W. Hubble, and K. A. Horton, 2003, Spectroch. Acta A **59**, 2391.
- Shen, Y. R., 1976, Rev. Mod. Phys. **1**, 48.
- Shen, Y. R., 1984, *The Principles of Nonlinear Optics* (John Wiley & Sons, New-York).
- Silberberg, Y., 1990, Opt. Lett. **15**, 1282.
- Skarka, V., N. B. Aleksić, and V. I. Berezhiani, 2003, Phys. Lett. A **319**, 317.
- Skryabin, D. V., and W. J. Firth, 1998, Phys. Rev. E **58**, R1252.
- Skupin, S., and L. Bergé, 2006, Physica D **220**, 14.

- Skupin, S., L. Bergé, U. Peschel, and F. Lederer, 2004a, Phys. Rev. Lett. **93**, 023901.
- Skupin, S., L. Bergé, U. Peschel, F. Lederer, G. Méjean, J. Yu, J. Kasparian, E. Salmon, J.-P. Wolf, M. Rodriguez, L. Wöste, R. Bourayou, *et al.*, 2004b, Phys. Rev. E **70**, 046602.
- Skupin, S., R. Nuter, and L. Bergé, 2006a, Phys. Rev. A **74**, 043813.
- Skupin, S., U. Peschel, C. Etrich, L. Leine, F. Lederer, and D. Michaelis, 2003, Opt. Quant. Electron. **35**, 573.
- Skupin, S., U. Peschel, C. Etrich, L. Leine, D. Michaelis, and F. Lederer, 2002, Opt. Lett. **27**, 1812.
- Skupin, S., G. Stibenz, L. Bergé, F. Lederer, T. Sokollik, M. Schnürer, N. Zhavoronkov, and G. Steinmeyer, 2006b, Phys. Rev. E **74**, 056604.
- Soto-Crespo, J. M., E. M. Wright, and N. N. Akhmediev, 1992, Phys. Rev. A **45**, 3168.
- Sprangle, P., E. Esarey, and J. Krall, 1996, Phys. Rev. E **54**, 4211.
- Sprangle, P., J. R. Peñano, and B. Hafizi, 2002, Phys. Rev. E **66**, 046418.
- Sprangle, P., J. R. Peñano, B. Hafizi, and C. A. Kapetanakis, 2004, Phys. Rev. E **69**, 066415.
- Steinmeyer, G., D. H. Sutter, L. Gallmann, N. Matuschek, and U. Keller, 1999, Science **286**, 1507.
- Stelmaszczyk, K., P. Rohwetter, G. Méjean, J. Yu, E. Salmon, J. Kasparian, R. Ackermann, J.-P. Wolf, and L. Wöste, 2004, Appl. Phys. B: Lasers & Optics **85**, 3977.
- Stibenz, G., N. Zhavoronkov, and G. Steinmeyer, 2006, Opt. Lett. **31**, 274.
- Stuart, B. C., M. D. Feit, S. Herman, A. M. Rubenchik, B. W. Shore, and M. D. Perry, 1996, Phys. Rev. B **53**, 1749.
- Suda, A., M. Hatayama, K. Nagasaka, and K. Midorikawa, 2005, Appl. Phys. Lett. **86**, 111116.
- Sudrie, L., A. Couairon, M. Franco, B. Lamouroux, B. Prade, S. Tzortzakis, and A. Mysyrowicz, 2002, Phys. Rev. Lett. **89**, 186601.
- Sudrie, L., M. Franco, B. Prade, and A. Mysyrowicz, 1999, Opt. Commun. **171**, 279.
- Sudrie, L., M. Franco, B. Prade, and A. Mysyrowicz, 2001, Opt. Commun. **191**, 333.
- Sulem, C., and P.-L. Sulem, 1999, *The Nonlinear Schrödinger Equation: Self-focusing and Wave collapse* (Springer-Verlag, New York), first edition.
- Talebpoor, A., J. Yang, and S. L. Chin, 1999, Opt. Commun. **163**, 29.
- Tamaki, Y., J. Itatani, Y. Nagata, M. Obara, and K. Midorikawa, 1999, Phys. Rev. Lett. **82**, 1422.
- Tempea, G., and T. Brabec, 1998a, Opt. Lett. **23**, 1286.
- Tempea, G., and T. Brabec, 1998b, Opt. Lett. **23**, 762.
- Théberge, F., N. Aközbek, W. Liu, J.-F. Gravel, and S. L. Chin, 2005a, Opt. Commun. **245**, 399.
- Théberge, F., W. Liu, Q. Luo, and S. L. Chin, 2005b, Appl. Phys. B: Lasers & Optics **80**, 221.
- Theopold, F. A., J.-P. Wolf, and L. Wöste, 2005, *Dial revisited: Belinda and white-light femtosecond lidar in range-resolved optical sensing of the atmosphere* (Springer Verlag, New York).
- Tien, A.-C., S. Backus, H. Kapteyn, M. Murnane, and G. Mourou, 1999, Phys. Rev. Lett. **82**, 3883.
- Tikhonenko, V., J. Christou, and B. Luther-Davies, 1996, Phys. Rev. Lett. **76**, 2698.
- Ting, A., I. Alexeev, D. Gordon, R. Fisher, D. Kaganovitch, T. Jones, E. Briscoe, J. Peñano, R. Hubbard, and P. Sprangle, 2005a, Phys. Plasmas **12**, 056705.
- Ting, A., D. F. Gordon, E. Briscoe, J. R. Peñano, and P. Sprangle, 2005b, Appl. Opt. **44**, 1474.
- Tohmon, R., H. Mizuno, Y. Ohki, K. Sasagane, K. Nagasawa, and Y. Hama, 1989, Phys. Rev. B **39**, 1337.
- Tong, X. M., Z. X. Zhao, and C. D. Lin, 2002, Phys. Rev. A **66**, 033402.
- Tosa, V., E. Takahashi, Y. Nabekawa, and K. Midorikawa, 2003, Phys. Rev. A **67**, 063817.
- Towers, I., A. V. Buryak, R. A. Sammut, B. A. Malomed, L.-C. Crasovan, and D. Mihalache, 2001, Phys. Lett. A **288**, 292.
- Trillo, S., and W. Torruellas (eds.), 2001, *Spatial Solitons* (Springer, Berlin).
- Trushin, S. A., S. Panja, K. Kosma, W. E. Schmid, and W. Fuss, 2005, Appl. Phys. B: Lasers & Optics **80**, 399.
- Tzortzakis, S., D. Anglos, and D. Gray, 2006, Opt. Lett. **31**, 1139.
- Tzortzakis, S., L. Bergé, A. Couairon, M. Franco, B. Prade, and A. Mysyrowicz, 2001a, Phys. Rev. Lett. **86**, 5470.
- Tzortzakis, S., M. A. Franco, Y.-B. André, A. Chiron, B. Lamouroux, B. S. Prade, and A. Mysyrowicz, 1999, Phys. Rev. E **60**, R3505.
- Tzortzakis, S., B. Lamouroux, A. Chiron, M. Franco, B. Prade, A. Mysyrowicz, and S. D. Moustazis, 2000a, Opt. Lett. **25**, 1270.
- Tzortzakis, S., B. Lamouroux, A. Chiron, S. D. Moustazis, D. Anglos, M. Franco, B. Prade, and A. Mysyrowicz, 2001b, Opt. Commun. **197**, 131.
- Tzortzakis, S., G. Méchain, G. Patalano, Y.-B. André, B. Prade, M. Franco, J.-M. Munier, A. Mysyrowicz, M. Gheudin, G. Beaudin, and P. Encrenaz, 2002, Opt. Lett. **27**, 1944.
- Tzortzakis, S., G. Méchain, G. Patalano, M. Franco, B. Prade, and A. Mysyrowicz, 2003, Appl. Phys. B: Lasers & Optics **76**, 609.
- Tzortzakis, S., B. Prade, M. Franco, and A. Mysyrowicz, 2000b, Opt. Commun. **181**, 123.
- Tzortzakis, S., B. Prade, M. Franco, A. Mysyrowicz, S. Hüller, and P. Mora, 2001c, Phys. Rev. E **64**, 057401.
- Tzortzakis, S., L. Sudrie, M. Franco, B. Prade, A. Mysyrowicz, A. Couairon, and L. Bergé, 2001d, Phys. Rev. Lett. **87**, 213902.
- Vakhitov, N. G., and A. A. Kolokolov, 1975, Radiophys. Quant. Electron. **16**, 783.
- Verhoef, A. J., J. Seres, K. Schmid, Y. Nomura, G. Tempea, L. Veisz, and F. Krausz, 2006, Appl. Phys. B: Lasers & Optics **82**, 513.
- Vidal, F., and T. W. Johnston, 1996, Phys. Rev. Lett. **77**, 1282.
- Vidal, F., and T. W. Johnston, 1997, Phys. Rev. E **55**, 3571.
- Vinçotte, A., and L. Bergé, 2004, Phys. Rev. A **70**, 061802(R).
- Vinçotte, A., and L. Bergé, 2005, Phys. Rev. Lett. **95**, 193901.
- Vlasov, S. N., V. A. Petrishchev, and V. I. Talanov, 1974, Radiophys. Quant. Electron. **14**, 1062.
- Vlasov, S. N., L. V. Piskunova, and V. I. Talanov, 1989, Sov. Phys. JETP **68**, 1125.
- Vuong, L. T., T. D. Grow, A. Ishaaya, A. L. Gaeta, G. W. 't Hooft, E. R. Eliel, and G. Fibich, 2006, Phys. Rev. Lett. **96**, 133901.
- Wagner, N. L., E. A. Gibson, T. Popmintchev, I. P. Christov, M. M. Murnane, and H. C. Kapteyn, 2004, Phys. Rev. Lett. **93**, 173902.
- Ward, H., and L. Bergé, 2003, Phys. Rev. Lett. **90**, 053901.

- Weinstein, M. I., 1983, *Commun. Math. Phys.* **87**, 567.
- Wiens, R. C., R. E. Arvidson, D. A. Cremers, M. J. Ferris, J. D. Blacic, and F. P. S. IV, 2002, *J. Geophys. Res. Planets* **107**(E11), FIDO3.
- Wille, H., M. Rodriguez, J. Kasparian, D. Mondelain, J. Yu, A. Mysyrowicz, R. Sauerbrey, J. P. Wolf, , and L. Wöste, 2002, *Eur. Phys. Jour. - Appl. Phys.* **20**, 183.
- Wolf, J.-P., 2000, *Ultraviolet/visible light detection and ranging Applications in air monitoring*, in (Meyers, 2000), p. 2226.
- Wöste, L., C. Wedekind, H. Wille, P. Rairoux, B. Stein, S. Nikolov, C. Werner, S. Niedermeier, F. Ronneberger, H. Schillinger, and R. Sauerbrey, 1997, *Laser & Optoelectron.* **29**, 51.
- Wyller, J., 2001, *Physica D* **157**, 90.
- Xi, T.-T., X. Lu, and J. Zhang, 2006, *Phys. Rev. Lett.* **96**, 025003.
- Xu, H. L., J. F. Daigle, Q. Luo, and S. L. Chin, 2006a, *Appl. Phys. B: Lasers & Optics* **82**, 655.
- Xu, X. H., W. Liu, and S. L. Chin, 2006b, *Opt. Lett.* **31**, 1540.
- Yablonovitch, E., 1974, *Phys. Rev. A* **10**, 1888.
- Yablonovitch, E., and N. Bloembergen, 1972, *Phys. Rev. Lett.* **29**, 907.
- Yang, G., and Y. R. Shen, 1984, *Opt. Lett.* **9**, 510.
- Yang, H., J. Zhang, J. Zhang, L. Z. Zhao, Y. J. Li, H. Teng, Y. T. Li, Z. H. Wang, Z. L. Chen, Z. Y. Wei, J. X. Ma, W. Yu, *et al.*, 2003, *Phys. Rev. E* **67**, 015401(R).
- Yu, J., D. Mondelain, G. Ange, R. Volk, S. Niedermeier, J.-P. Wolf, J. Kasparian, and R. Sauerbrey, 2001, *Opt. Lett.* **26**, 533.
- Yu, J., D. Mondelain, J. Kasparian, E. Salmon, S. Geffroy, C. Favre, V. Boutou, and J.-P. Wolf, 2003, *Appl. Opt.* **42**, 7117.
- Zakharov, V. E., and E. A. Kuznetsov, 1986, *Sov. Phys. JETP* **64**, 773.
- Zakharov, V. E., and A. M. Rubenchik, 1974, *Sov. Phys. JETP* **38**, 494.
- Zeng, Z., R. Li, W. Yu, and Z. Xu, 2003, *Phys. Rev. A* **67**, 013815.
- Zharova, N. A., A. G. Litvak, and V. A. Mironov, 2003, *J. Exp. Theor. Phys.* **96**, 643.
- Zozulya, A. A., S. A. Diddams, A. G. Van Engen, and T. S. Clement, 1999, *Phys. Rev. Lett.* **82**, 1430.